MASTER THESIS

Aircraft measurements of tropospheric NO_2 with an imaging DOAS instrument

Geolocation correction, characterization of the instrument and first application

Patricia Altube Vázquez
Supervisor: Anja Schönhardt
23.08.2012

Postgraduate Program in Environmental Physics (PEP)
Institut für Umweltphysik (IUP)
University of Bremen

Preface

Imaging DOAS (Differential Optical Absorption Spectroscopy) constitutes a very powerful spectroscopic technique for the mapping of two-dimensional distributions of trace gases in the atmosphere. The potential of aircraft based imaging DOAS (iDOAS) lies on the possibility of retrieving these pollution maps with improved spatial resolution relative to other measurement platforms and with the flexibility that aircraft motions provide in the selection of the target location. The spatial resolution characteristics of iDOAS allow the quantification of trace gas distributions and sources even in situations of relatively large spatial gradients in the trace gas amounts.

The new iDOAS instrument was developed at the IUP Bremen and, after adequate calibration and characterization measurements, in June 2011 was installed on an aircraft for its first test flights over distinctive sources of tropospheric air pollution.

The current thesis work is focused on the analysis of spectroscopic data collected in a selected flight, performed within that first measurement campaign. The final objective is to characterize an anthropogenic point source of tropospheric nitrogen dioxide, the exhaust plume of a power plant, and to assess the quality of the instrument for such purpose. In the context of airborne imaging DOAS, characterization of the source involves the determination of the emission rate and an appropriate mapping of the horizontal dispersal of the plume. Both steps require an accurate retrieval of the nitrogen dioxide amounts from the spectral recordings and a correct computation of the area imaged on the ground by the instrument mounted on the aircraft.

The present document constitutes a compilation of the steps followed in pursue of the aforementioned objectives. It is therefore divided in three major parts which reach from the most general theoretical fundaments to the particular iDOAS application case.

Part I offers a generalized view on the atmospheric chemistry of nitrogen oxides and on atmospheric trace gas measurements, with special emphasis on spectroscopic techniques. It ends with the introduction of the DOAS method, with an overview of all its essential aspects, acting as a natural link to the more particular iDOAS measurements, which constitute the central subject of the immediately following part.

In effect, Part II deals with the basics of iDOAS technique, going into the description of the particularities of the new instrument and establishing the theoretical aspects and the methodology that have been applied in the iDOAS data analysis. It describes some well known questions related to the general DOAS analysis but it also introduces several particular and dedicated approaches adopted in the case study in question. In addition, a last chapter in this central part dedicates specific attention to point source emissions, to the classical approach through which they are modeled and to a method to measure emission strengths through DOAS measurements. Therefore, Part II is thought to put the reader in the picture about the real application case analyzed in Part III. It is in this last part when all the concepts developed in the previous chapters are applied and tested, coming to a common aim; the optimized retrieval of nitrogen dioxide column amounts from spectral iDOAS recordings over the exhaust plume of a power station. The data analysis in this respect is, in addition, oriented to the assessment of the performance of the instrument in a real case study (in comparison to the theoretical expectation), and naturally leads to the very final objective of the presented work: the estimation of the NO_2 emission rates from the power plant stack as an example of the capabilities of the airborne iDOAS instrument.

General Index

Part I: FOUNDATIONS

Part II: APPROACH

Part III: APPLICATION

Part I:

FOUNDATIONS

Contents

1. Nitrogen Oxides in the Atmosphere*

The atmosphere is the gaseous shield surrounding the Earth's surface. It is defined as a characteristic mixture of gases and suspended particles, its composition and properties being in close relationship to the processes going on at the surface, with special emphasis on the hydrosphere, lithosphere, cryosphere and biosphere.

As one of the major components of the climate system, the atmosphere is subjected to natural variability and changes in its composition may greatly affect the Earth's climate. Indeed, the atmosphere is responsible for the natural greenhouse effect that warms up the surface, for the protection of that surface from highly energetic radiation from the sun and for the redistribution of water and heat in the system. Remarkably, the trace gases present in the atmosphere (those gases that altogether make up less than 1% of the total volume) play a major role in these processes.

During the last 250 years the most abrupt changes in atmospheric trace gas composition are taking place, as a result of anthropogenic activities. Increasing amounts of these compounds are not only changing the atmospheric properties but in many cases also compromise the health of the living organisms. Some of the emitted trace gases and particles may have a direct repercussion on the radiative equilibrium of the atmosphere, on its chemistry or on the pollution level. In other cases, they may also effect an indirect impact, modifying the physical-chemical properties of the atmosphere, influencing the budget of greenhouse gases or acting as precursors for hazardous pollutants and aerosol, which might also act as cloud condensation nuclei.

The latter is the case for reactive nitrogen oxides (NO_x), encompassing nitric oxide (NO) and nitrogen dioxide (NO_2), which are in the heart of the present work. In the troposphere, nitrogen oxides greatly control the concentration of the hydroxyl radical (OH) and are responsible for the formation of ozone (O_3), a relevant greenhouse gas and toxic pollutant. In turn, the NO_x family takes part in the catalytic cycles destroying stratospheric ozone, which acts as a shield for highly energetic UV radiation.

Here, special attention is given to the role of NO_x in the troposphere, where anthropogenic emission has its most direct impact. The processes described in due course point out the importance of monitoring reactive nitrogen oxide amounts and emissions continuously in order to study their chemical pathways, transport and dispersal mechanisms and to determine trends or risky concentration levels.

1.1 Sources of NO_x

Sources of nitrogen oxides in the troposphere include a variety of natural and anthropogenic processes. Most of the emissions result from processes at high temperatures, when thermally decomposed oxygen atoms react with atomic nitrogen. Consequently, fossil fuel combustion, biomass burning and lightning constitute major sources. Emission from soils, by microbes in nitrification and denitrification processes, is also a very strong contributor.

---

[*] The present chapter is based on the notes by D.H. Ehhalt on Gas Phase Chemistry of the Troposphere (1999).

Smaller sources such as aircraft emissions and stratospheric input are also to be considered, since they have great importance for the budget in the free troposphere, where NO_x lifetimes are longer than at lower altitudes. Lightning and aircraft emissions are volume sources which might inject nitrogen oxides at various heights in the troposphere. Other major sources mentioned previously are surface sources; such emissions take place within the boundary layer and, provided the short lifetime of NO_x (of the order of hours in the lower troposphere), their effect in the upper layers is minimal. It is worth to mention that the NO_x in the stratosphere is formed mainly in the dissociation N_2O in the presence of very reactive oxygen radicals produced in the photolysis of ozone.

A summary of the source strengths and their uncertainties is shown in Table 1.1, together with a graphical display of their contributions to the global emission.

Relative contributions are linked to the spatial distribution and seasonal variation of the mentioned sources. All surface sources are limited to continental areas, as emission from oceans may, in principle, be considered negligible. Therefore, over oceans, the role of lightning, stratospheric input and aircraft emissions (at localized areas) is enhanced.

Biomass burning gains importance in the tropical regions, being particularly strong during dry seasons, and fossil fuel combustion may reach a 90% contribution to the total NO_x emissions in highly populated and industrialized continental areas, especially in the northern hemisphere with a noticeable increment in winter. The high uncertainties in the quantification of NO_x emission from soil come from the dependence of these emissions on various factors such as soil temperature, moisture content, nutrient availability or plant coverage. These dependencies also translate in spatial and temporal variability.

	Source	**Emission (Tg N /year)**	**Uncertainty (Tg N /year)**
●	Fossil Fuel Combustion	22,0	13-31
●	Biomass Burning	7,9	3-15
●	Soil Emission	7,0	4-12
●	Lightning	5,0	2-10
●	Aircraft emissions	0,9	--
●	Stratospheric	0,6	0.4-1
●	Oxidation of Ammonia	0,9	0.6

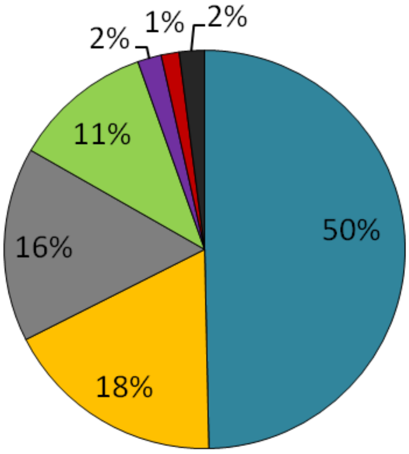

Table 1.1: Tropospheric source strengths of NO_x and their uncertainties: emission rates in tons of fixed nitrogen per year and their contribution to global emission in percentage terms. (Source: Lee et al, 1997)

On the whole, the anthropogenic influence upon the NO_x budget is overwhelming; half of the total emissions are directly attributable to fossil fuel combustion, of which 60% come from industrial activities, with combustion power plants being the major emitters. And what is more, consideration of human involvement in biomass burning and soil emissions through forest fire initiation, waste incineration and fertilisation, raises the total anthropogenic contribution up to 70% of the global NO_x emissions. Localization of these anthropogenic sources and quantification of their strengths is crucial for the development of improved emission scenarios, which are, together with an appropriate modelling of the chemistry and transport, in turn, decisive for the derivation of prognostics on the future evolution of the atmospheric system.

1.2 Tropospheric chemistry of NO_X

Reactive nitrogen oxides constitute trace gases of great relevance for atmospheric chemistry and pollution. In particular, in the troposphere, high concentrations of NO_x not only can cause damage to vegetation and are detrimental for health but also intercede in the OH radical chemistry, favouring particular oxidation pathways, and resulting in the formation of ozone, which is itself also a dangerous toxic. The chemistry of the OH radical, being the major oxidizing agent in the troposphere due to its high reactivity and recycling properties, is very complex in a detailed description. Fortunately, a basic picture of the dominant pathways is sufficient to highlight the effect of large NO_x concentrations in tropospheric chemistry and composition.

The major part of the emissions quantified in the previous section takes place in the form of NO. However, the emitted NO is rapidly oxidized to NO_2 trough reaction with O_3. During daylight, NO_2 is photolized back to NO via production of an oxygen atom that regenerates O_3 in reaction with atmospheric O_2 molecules. This set of reactions determines a null cycle in which concentrations of NO, NO_2 and O_3 are in photostationary equilibrium:

$$NO + O_3 \rightarrow NO_2 + O_2 \qquad (1.1)$$

$$NO_2 + h\nu \xrightarrow{\lambda < 400nm} NO + O(^3P) \qquad (1.2)$$

$$O(^3P) + O_2 \xrightarrow{M} O_3 \qquad (1.3)$$

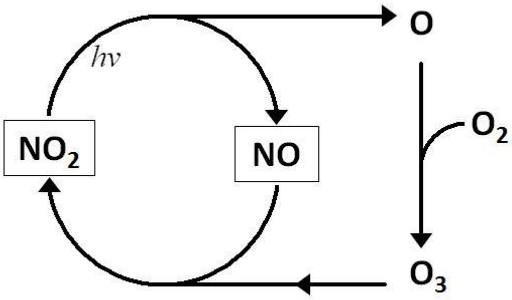

The rapid NO-NO_2 interconversion in this cycle is the reason for considering both compounds as members of a same family; the NO_x family. The resulting NO/NO_2 ratio depends on temperature and pressure conditions, on the photon flux and on the availability of O_3 molecules.

Something similar applies to the HO_x family, encompassing OH and HO_2 radicals. The best example at this respect is the oxidation of CO by OH. The HO_2 formed in this reaction interacts with O_3 to yield back OH. This illustrates the recycling property of OH in oxidizing tropospheric trace species. Still, this reaction group does not constitute a null cycle but results in a net O_3 destruction:

$$CO + OH \rightarrow CO_2 + H \qquad (1.4)$$

$$H + O_2 \xrightarrow{M} HO_2 \qquad (1.5)$$

$$HO_2 + O_3 \rightarrow OH + 2O_2 \qquad (1.6)$$

$$Net: CO + O_3 \xrightarrow{M} CO_2 + O_2 \qquad (1.7)$$

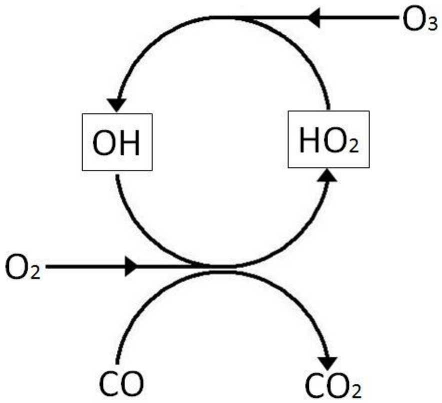

However, the NO_x and HO_x cycles do not operate independently but are interconnected by the reaction:

$$HO_2 + NO \rightarrow OH + NO_2 \qquad (1.8)$$

Being this a pathway that performs the NO_2 and OH recycling without consumption of O_3, the result of the coupling of both cycles may be a catalytic production of O_3. The importance of Reaction 1.8 is critical for it allows the possibility of ozone production with the mediation of NO and because it emphasizes the role of nitrogen oxides in the OH budget.

Reaction 1.8 is competing with Reaction 1.6 and whether a net production of O_3 takes place or not will be determined by the abundance of NO_x in the troposphere. In the unpolluted atmosphere, the NO_x mixing ratio is generally too low to act as catalyst. Conversely, in areas of large emissions, ozone production kicks off.

The effect of the coupling of the HO_x-RO_x (hydrogen radicals and peroxy radicals) and NO_x cycles is illustrated in Figure 1.1; as shown, analogous pathways are also found for oxidation of methane (CH_4) and non-methane hydrocarbons (NMHC). Since NMHC and volatile organic compounds (VOC) are also emitted in large quantities in fossil fuel combustion and biomass burning processes, the effect on ozone production is further enhanced.

In addition, the reaction of nitrogen oxides with VOC (from direct emissions or produced in the hydrocarbon oxidation chains) may result in the formation of other organic compounds such as peroxy acetyl nitrate (PAN), which is a main component of photochemical smog and can be much more harmful for health than the primary nitrogen species.

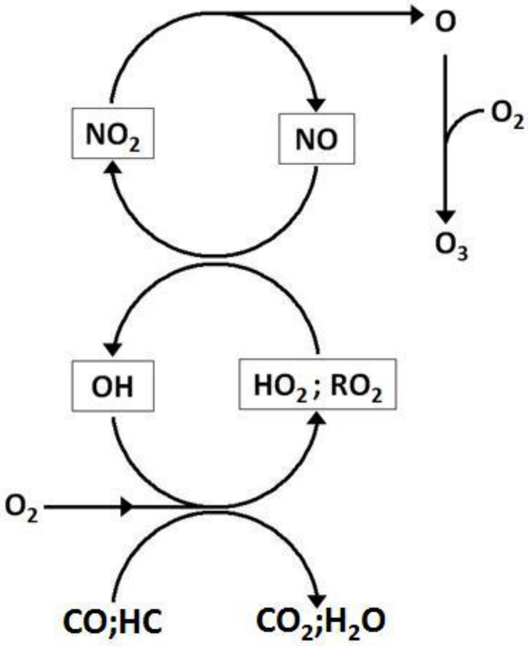

Figure 1.1: Schematic depiction of catalytic O_3 production in the coupling of HO_x-RO_x (hydrogen radicals and peroxy radicals) and NO_x (nitrogen oxides) cycles.

PAN acts as reservoir for NO_x and HO_x; it can either constitute a sink by dry deposition on the surface or a temporary reservoir before it eventually thermally decomposes releasing back the compounds to the atmosphere.

However, the main sink for NO_x and the termination step for the O_3 producing catalytic cycles is the reaction of NO_2 with OH to yield nitric acid (HNO_3):

$$OH + NO_2 \xrightarrow{M} HNO_3 \tag{1.9}$$

Reaction 1.9 implies that the NO_x in the form of NO_2 provides a loss pathway for OH. Moreover, such pathway will moderate the ozone production in polluted environments when the ratio between NO_x and hydrocarbon amounts is large, favoring instead an acidification of the atmosphere (Sillman et al, 1990). Unfortunately, HNO_3 is a main component of acid deposition; also a potential hazard for animal life and vegetation.

2. Trace Gas Measurements

Knowledge of the atmospheric composition at different temporal and spatial scales through the study of the chemical pathways and reaction rates in the atmosphere as well as its interaction mechanisms with the other components of the climate system is critical for the assessment and prevention of the impact of human-induced variations. Atmospheric measurement techniques have proven an invaluable tool for the purpose, securing the means for the monitoring and mapping of atmospheric composition and pollution, for the quantification of trace gas sources and for the study of chemical processes and transport of pollutants.

As for all field observations, portability and simplicity of design and use are ideal requirements for the instruments aimed at atmospheric measurements. In addition, atmospheric measurement methods must be specially sensitive and selective to be able to detect the small amounts of the trace gases present in the medium without interference with other species or influence from ambient conditions.

The selection of a particular technique will certainly depend on the objectives behind the measurement; e.g. the species to be measured, the accuracy and sensitivity required, the desired spatial and temporal resolution and the demands of the experimental setup.

In a first distinction, measurement techniques can be divided into in-situ and remote methods. In-situ implementations are well suited for spatially localized observations, whereas remote sensing measurements yield absolute quantities for larger air volumes and allow measurements in otherwise inaccessible regions. However, remote sensing methods rely on indirect measurements; the quantity of interest is not generally directly measurable and has to be retrieved from the information contained in another variable, physically related to the desired one. This means that several other processes and factors might as well be affecting the measurement, what poses additional complexity into the data interpretation, result validation and uncertainty estimation.

Spectroscopic techniques, based on the sensing of electromagnetic radiation in its interaction with the air sample, are a powerful tool for atmospheric monitoring due to their high sensitivity, universality (they are not specific for a single gas) and for their large potential for remote sensing.

Two main branches can be recognized among spectroscopic methods attending to the nature of the interaction, relying either on the analysis of the radiation emitted by the sample (passive) or on the study of the absorption of radiation by the sample (active). In the case of atmospheric samples, this distinction is particularly important for spectroscopic measurements in the infrared (IR) and microwave (MW) wavelength regions, where thermal emission from vibrational and rotational molecular transitions gains relevance. Since emission of ultraviolet and visible (UV-Vis) radiation by air molecules is negligible, only absorption spectroscopy measurements are possible in these wavelength ranges. The active-passive distinction in this case depends on whether the radiation source used is artificial or natural respectively.

2.1 Radiation transfer in the atmosphere

Radiation transfer in the atmosphere is determined by the interaction processes taking place between the radiation and molecules and particles present in the air. The character and effect of these interaction processes will depend on the nature of the radiation and matter involved. This is what makes possible to determine the presence and abundance of different species in the air sample; this is where the potential of spectroscopic techniques lies. The retrieval of the desired properties from spectroscopy requires detailed understanding and quantification of the main and most general processes affecting radiation transfer in the atmosphere.

Molecular Absorption

Absorption of radiation by molecules (and molecules contained in particles) results in a transition of the molecule to higher energetic states. Because the energy level distribution is different for each molecule and because the levels involved in the transition depend on the energy of the absorbed radiation, each molecular species exhibits unique spectral absorption signatures. The attenuation power of an absorbing species (i), in its interaction with radiation, is quantified through the absorption coefficient (ε_i^a), which accounts for the efficiency of the absorption process (cross section, σ_i^a) and the abundance of absorber (number density, n_i).

$$\varepsilon_i^a(\lambda) = \sigma_i^a(\lambda) \cdot n_i \tag{2.1}$$

The absorption coefficient is defined for each particular absorbing species present in the medium, due to the aforementioned unique spectral absorption characteristics, imprinted in the absorption cross section. Since the absorption coefficient is an additive quantity, the reduction (dI_a) in the intensity of the radiation ($I(\lambda)$) when traversing an infinitesimal medium containing N different absorbing species is given by:

$$dI_a(\lambda) = -I(\lambda)\left(\sum_{i=1}^{N} \varepsilon_i^a(\lambda, s)\right) ds = -I(\lambda)\left(\sum_{i=1}^{N} \sigma_i^a(\lambda, s) \cdot n_i(s)\right) ds \tag{2.2}$$

Note that absorption coefficients depend on the position along the radiation path (s); directly through the absorber number density distribution and indirectly through the absorption cross section dependence on temperature and pressure, quantities which might vary along the path.

Elastic scattering

Elastic scattering refers to the attenuation of the transmitted radiation by the deflection (without change in energy) out of the original direction of propagation of the photons in their interaction with molecules and particles in the atmosphere. Scattering by air molecules is usually referred to as Rayleigh scattering, whereas Mie scattering refers to scattering by aerosols and cloud droplets. The need of such a distinction comes from the different relative size between scatterer and wavelength in each case, which results in distinguished properties between the two scattering processes.

Rayleigh scattering is effected by molecules, whose radius is small compared to the wavelength of the incident radiation ($2\pi r << \lambda$). The probability of this type of scattering is strongly wavelength dependent ($\sim\lambda^{-4}$), being most efficient for decreasing wavelengths. The corresponding scattering phase function shows some preference for forward and backward scattering direction over sideways. On the contrary, Mie scattering, which applies in the case of aerosols with size comparable to the radiation wavelength, is weakly wavelength dependent with strong preference for forward scattering.

Anyhow, the effects of Mie and Rayleigh scattering upon the radiation transmission are both generally treated similar to absorption processes, defining scattering coefficients, in analogy to equation 2.1, with characteristic Mie (M) and Rayleigh (R) scattering cross sections in each case. Similarly, an expression for attenuation of radiation due to elastic scattering is found:

$$dI_s(\lambda) = -I(\lambda)[\varepsilon_M(\lambda,s) + \varepsilon_R(\lambda,s)]ds = -I(\lambda)[\sigma_M(\lambda)n_M(s) + \sigma_R(\lambda)n_R(s)]ds \qquad (2.3)$$

Inelastic scattering

Inelastic scattering takes place when, in the course of the deflection, the incident photon transfers part of its energy to the scattering molecule (or vice versa). Thus, unlike in the elastic case, the excitation state of the molecule is altered. When the energetic transition affects only the rotational states of the molecule, the process is termed Rotational Raman Scattering (RRS), while in Vibrational Raman Scattering (VRS) the vibrational states are also changed.

The effect of RRS is strong in the transmission of solar radiation through the atmosphere; as a consequence, the optical depth of the solar Fraunhofer lines appears decreased for increasing solar zenith angle. This effect is referred to as *Ring Effect* or *Filling-in* (Grainger and Ring; 1962).

Thermal emission

Thermal motion of all charged particles generates EM radiation. Such thermal emission by molecules also affects the radiative transfer in the atmosphere, in this case in the form of an increase of the transmitted intensity:

$$dI_{th} = \varepsilon^a(\lambda) I_{BB}(\lambda,T)ds \qquad (2.4)$$

I_{BB} in equation 2.4 stands for the Planck function of thermal emission of a black body at a temperature T. ε_a is the total absorption coefficient, sum of all the individual coefficients of the absorbers present, which equals the emission coefficient of the medium.

Finally, the combined effect of absorption, scattering and emission processes leads to the radiation transfer equation (RTE). The sum of the Equations 2.2, 2.3 and 2.4 above plus an additional term accounting for scattering processes, which deflect radiation into the considered path (scattering-in) make up for the RTE; this is the starting point for the retrieval of atmospheric parameters from spectroscopic measurements.

2.2 Spectroscopic techniques for NO_2

Spectroscopic techniques have commonly been used to perform field measurements of atmospheric NO_2 amounts. In situ spectroscopy techniques used to derive the concentration of NO_2 include, among others: Mask Correlation Spectroscopy (COSPEC), relying on the degree of correlation between the absorption spectrum of the air sample and an optical mask reproducing the spectrum of the gas under investigation (e.g. Beilke et al.,1981); Tunable Diode Laser Spectroscopy (TDLS), which uses as source a narrowband laser of variable frequency to scan an absorption line of the target gas, both for the reference gas and for the air sample, so that the resulting real air spectrum is fitted to the calibrated one (e.g. Schiff et al., 1990; Fehsenfeld et al., 1990); Photolysis/Chemiluminescence, a technique that relies on the photolytic conversion of NO_2 to NO and that measures the photon flux from the decay of excited NO_2 molecules, produced, in turn, by the oxidation of NO with O_3 (e.g. Fehsenfeld et al., 1990).

Differential Optical Absorption Spectroscopy (DOAS) (e.g. Platt and Perner, 1980) has developed as one of the most popular methods to measure trace gases in the open atmosphere, due to its wide range of applications, furthermore allowing automatic and simultaneous measurement of the amounts of various gases.

The measurable gases are those that show absorption features that rapidly vary with wavelength, preferably in the UV-Vis range, as it is the case for NO_2 in the 330-500nm wavelength region.

The differential behavior of the absorption signal (narrowband signature) is a crucial requirement to distinguish the extinction of radiation by absorption from the extinction by scattering, as the last appears as a broadband signature in the spectrum. The measurements are made at various wavelengths and with relatively high spectral resolution to identify and separate different species, since each of them exhibits a characteristic variation of absorption with wavelength.

3. Differential Optical Absorption Spectroscopy

Quantitatively, absorption spectroscopy techniques are all based on the radiation transfer equation (RTE). For the description of the attenuation of radiation when traversing an absorbing medium, the Beer-Lambert law is generally used; i.e. the integrated form of the simplified RTE for only extinction processes. This fundamental equation relates the absorbance of the medium to the sum, over all present absorbing species, of the integrated concentration of absorber along the light path weighted by the efficiency of the absorption process.

When radiation travels through the atmosphere, however, it does not only undergo extinction due to absorption of gases but also due to scattering by air molecules (Rayleigh scattering) and aerosol and cloud particles (Mie scattering) and even due to the transmissivity of the instrument used for detection at the end of the light path. An extended version of the Beer-Lambert equation includes all these factors affecting the intensity of the radiation.

The basic assumption in the Differential Optical Absorption Spectroscopy *(*DOAS) method is that all the extinction phenomena that smoothly vary with wavelength (broadband signatures) can be, within a reduced wavelength range, called fitting window, simultaneously approximated by a polynomial. The fitting window for the retrieval is selected so that the differential absorption by the trace gas of interest is largest and interference with other species is minimal. An appropriate fitting window for NO_2 retrieval may be found around 430nm, where its absorption is highly structured and most of the absorptions by other species are small.

After subtracting the approximated broadband spectrum from the measured one, a differential spectrum is left, in which only absorption features from the target species and a limited number of other trace gases are present. This absorption only spectrum is modeled by the original Beer-Lambert equation. Measuring absorbances for different wavelengths, the model is inverted to obtain the slant column densities (SCD, i.e. the integrated concentration of the absorber along the light path).

The slant column obtained from the DOAS fit depends not only on the absorber number density but also on the light path in the atmosphere through the absorber layer(s) and, hence, on the observation geometry. When performing real atmospheric measurements the parameter of interest is usually the vertical column density (VCD, i.e. the integrated concentration of the absorber vertically through the atmosphere) because it is independent of the observation geometry.

Therefore, the conversion of the slant column obtained from the DOAS equation into the vertical column constitutes a second step of the DOAS technique. The relation between both columns is given by the Air Mass Factor (AMF), defined as the ratio of the slant column to the vertical column.

As will be explained, the computation of the AMF (that is, of the actual light path through the absorber layer(s)) can be quite challenging for certain DOAS applications and often must be performed by means of complex radiative transfer models.

3.1 Observation modes and platforms

Active and passive DOAS

In a first approach, DOAS principle applications can be classified into active and passive setups, depending on whether artificial or natural light (e.g. sun or moon) is used as source.

The main advantage of active DOAS is the easy computation of the light path through the atmosphere, which allows direct application of the Beer-Lambert law and retrieval of atmospheric concentrations, needing only basic assumptions on the distribution of the absorber along the light path. However, the low mixing ratios of trace gases in the atmosphere require long light paths in order to achieve the appropriate sensitivity in the retrieval, which increases the complexity in the implementation of these active instruments. For this reason, active DOAS methods are in general, restricted to ground based applications, using horizontal light paths to analyze tropospheric composition.

On the other hand, passive DOAS measurements, using natural light sources, provide even longer light paths through the atmosphere (up to around 1000km) and thus, an increased sensitivity in the retrieval of trace gas amounts. These passive applications require relatively simple instrumental setups but the DOAS retrieval gains in complexity, as natural light sources like the sun or the moon show highly structured spectra (e.g. with both broad and narrow absorption features). For instance, the strong Fraunhofer lines in the solar spectrum must be accurately measured and removed in order to distinguish the comparably weak absorptions of atmospheric trace gases. A particular limitation of passive DOAS, that does not apply for satellite based measurements, is that it is not possible, with the actual instrument, to obtain the extraterrestrial spectrum incident at the top of the atmosphere, which would constitute the ideal reference for the retrieval. Instead, a low absorption spectrum measured under similar conditions is used as reference. This limitation implies that only differences in slant columns (differential slant column densities; dSCD[*]) between the measurements can be determined. Nevertheless, it is still possible to calculate the vertical column if the AMF for the measurements is known.

An additional division differentiates between direct sunlight and scattered sunlight passive DOAS implementations. The latter measures the light from the sun or the moon scattered in the atmosphere and/or the surface. The former requires a tracking system to keep the detector directly pointed to the sun or moon. This setup, although cumbersome and limited to a single and varying viewing direction, has several major advantages such as the increase of the signal-to-noise

---

[*] The word “differential” when applied to dSCD refers to differences of the Slant Column Densities in contrast with its meaning in the DOAS term, where it alludes to the differential behavior of the absorption signal.

ratio due to the high intensity of direct light income, the simplification of the light path calculation or the absence of the Ring effect.

Scattered light passive DOAS

The range of applicability of passive DOAS is further enlarged with scattered light measurements, as it allows measurements under cloudy conditions and plenty of viewing geometries from different platforms. Scattered light DOAS owes its name to the fact that the light collected in the detector has been scattered at points located along the viewing direction of the telescope. In this case, experimental implementations are relatively simple but special difficulties have to be addressed in the DOAS retrieval. First of all, the Fraunhofer lines may appear distorted due to the Ring Effect, which is attributed mainly to rotational Raman scattering (Vountas et al., 1998). In addition, because the paths in the atmosphere are particularly complex for scattered light, an estimation of the AMF through a radiative transfer model is needed in order to compute the vertical columns from the slant columns.

The instruments on board of satellites usually operate in nadir geometry, with the telescope looking downwards and collecting the light scattered on the surface and atmosphere below. With this arrangement, retrieval of global distributions of trace gases is possible (e.g. Richter and Burrows, 2002). Furthermore, these instruments may also be configured in limb viewing geometry for derivation of vertical profiles.

In the case of ground-based observations with the instrument pointing at zenith sky, the slant columns are usually obtained at different solar zenith angles (SZA) (e.g. Noxon et al., 1975; Richter et al., 1995). Zenith-sky geometry allows long light paths through the stratosphere, which do not vary in the presence of tropospheric clouds, and the maximum sensitivity is achieved at twilight (low sun) when the light path is longest. However, this observation geometry is not very sensitive to tropospheric absorbers as they lie below the scattering point and light paths through the troposphere are short and not very variable.

In order to retrieve information about tropospheric absorbers from the ground, observations with the telescope pointed also at various elevation angles other than the zenith are performed at similar illumination conditions (fixed SZA). For low viewing angles (close to the horizon) the light path through the troposphere is long and weakly dependent on SZA, while the path through the stratosphere remains practically constant throughout the measurement for constant SZA. Therefore, tropospheric sensitivity in horizon viewing geometry will be greatest at high sun when illumination conditions are optimal.

This method is known as multi-axis DOAS (MAX-DOAS) and it also allows the retrieval of vertical profiles, if measurements for enough different viewing elevations are carried out; the measured spectrum for each line of sight carries information on the trace gas amounts at different altitudes (e.g. Wittrock et al, 2004, and references therein).

At this stage it is important to point out that in the case of NO_2, tropospheric column amounts can also be estimated from any of the platforms mentioned by subtracting the stratospheric column from the total column, the former being inferred, e.g. from a clean air spectrum, assuming that the tropospheric NO_2 is negligible for unpolluted scenarios (e.g. Richter and Burrows; 2002).

Airborne Measurements

For aircraft-based measurements, information on absorbers in the atmosphere above and below the airplane can be obtained by installing both zenith looking and nadir looking instruments (e.g. Melamed et al., 2002).

Naturally, the upward-downward viewing double setting has also been intensively used for profile retrieval through Airborne MAX-DOAS measurements (AMAX-DOAS) (e.g. Wang et al., 2005; Bruns et al., 2006). This setup on an aircraft allows the measurement of the horizontal variability in the trace gas distribution in addition to the vertical one.

In general, the use of scattered light DOAS on airborne platforms has proved invaluable in the study of emissions from point sources such as power plants, ships and volcanoes as it provides the means to monitor otherwise inaccessible areas with improved spatial resolution (e.g. Wang et al., 2006; Berg et al., 2011).

However, the main disadvantage of the MAX-DOAS method is that the measurements at different viewing directions are not simultaneous, what might become a major problem in the retrieval if the atmospheric conditions are rapidly variable. A more recent expansion of the MAX-DOAS system measures simultaneously a large number of viewing directions. This technique is called imaging-DOAS (iDOAS).

In ground based iDOAS monitoring of point-source emissions, a measurement of the vertical distribution of trace gases is coupled to a horizontal scanning system to yield a 2-dimensional vertical map of the exhaust plume (e.g. Lohberger et al., 2004; Bobrowski et al., 2006). In analogy, iDOAS from aircraft is used to derive 2-dimensional horizontal pollution maps, the scanning system being substituted by the motion of the airplane (e.g. Heue et al., 2008).

Overall, aircraft based imaging DOAS constitutes a key tool in the study of tropospheric trace gas distribution and transport processes, plume chemistry and dispersal; allowing, due to its high spatial resolution, to distinguish closely located independent pollution sources. Moreover, airborne iDOAS measurements might give information on the trace gas variability within a satellite pixel and may be used for satellite data validation (assessment on data quality; e.g. Heue et al., 2005; Fix et al., 2005), as the flexibility in the flight tracks and times makes it possible to match satellite overpasses.

3.2 Mathematical formulation

All DOAS instruments consist basically of an optical system collecting radiation and a detection system for the spectral dispersion and recording of the collected radiation. The retrieval of the trace gas information contained in the spectroscopic measurements constitutes an inverse problem that requires a physical forward model that appropriately describes such information. Although the standard mathematical description for the DOAS method is valid for all observation modes and platforms, here special attention is given to scattered DOAS applications, where the complex radiation transfer through the atmosphere plays a significant role. The treatment includes the classical DOAS equations and a brief discussion on the air mass factor characteristics.

The measured intensity is classically modelled through the Beer-Lambert law, accounting for its extinction along the light path due to molecular absorption by a number of species (N) present in the atmosphere and due to Mie and Rayleigh scattering.

$$I(\lambda,L)=$$

$$=I_0(\lambda,L)\exp\left\{-\int_0^L\left(\sum_{i=1}^{N}\sigma_i(\lambda,s)n_i(s)+\sigma_M(\lambda,s)n_M(s)+\sigma_R(\lambda,s)n_R(s)\right)ds\right\} \tag{3.1}$$

For simplicity, in the present description the effect of the instrument upon the shape of the measured intensity, i.e. the finite resolution of the spectroscopic system is not taken into account. Such effect is mathematically described as a convolution of the intensity with the instrument slit function.

The measured intensity depends on the wavelength (λ) and on the light path (L). The wavelength dependence comes from the spectral structure of the incident radiation (I_0) and of the extinction cross sections (σ). Note that extinction cross sections and number densities of the different species (n) depend on the position along the light path (s).

The quantity L stands for an intensity weighted average light path. Actually, even for very well defined observation conditions, the measured signal consists of contributions from light scattered at different points in the atmosphere, following different light paths. Moreover, there is a further assumption implicit in equation 3.1; that the measured intensity can be separated into a factor for the radiation transmission in absence of absorber and an extinction factor accounting for the effect of the absorber. However, this assumption is only valid for weak absorbers (usually with optical densities below 0.1), because otherwise the radiation transfer is affected by the absorption process. Light paths with strong absorption contribute much less to the total measured radiation and the factor separation is not valid anymore because this path weighting is not affecting the absorber free reference spectrum in the same way.

In this classical approach, it is also assumed that cross sections do not depend on the light path, what means that their temperature and pressure dependence are not taken into account. The consequences of a strongly path dependent absorption cross section are analogous to the effect of a strong absorber as explained before.

With this additional simplification, the above equation can be written in terms of the slant columns (SC) for each kind of extinction process:

$$I(\lambda, L) = $$

$$= I_0(\lambda, L)\exp\left\{-\left(\sum_{j=1}^{J}\sigma_j(\lambda)SC_j(L) + \sigma_M(\lambda)SC_M(L) + \sigma_R(\lambda)SC_R(L)\right)\right\} \tag{3.2}$$

The slant column for a particular trace gas is defined as the integrated amount of species along the light path and it is itself also dependent on the light path:

$$SC_j(L) = \int_0^L n_j(s)ds \tag{3.3}$$

The basic assumption in the DOAS method is that all extinction phenomena that vary smoothly with wavelength (broadband signatures) can, within a reduced wavelength range called the fitting window, be all simultaneously approximated by a polynomial. This approximation includes both Mie and Rayleigh scattering processes and also low frequency absorption signatures:

$$I(\lambda, L) = I_0(\lambda, L)\exp\left\{-\left(\sum_{j=1}^{J}\sigma'_j(\lambda)SC_j(L) + \sum_p b_p\lambda^p\right)\right\} \tag{3.4}$$

The new cross sections (differential absorption cross sections, σ'_j) introduced in equation 3.4 only account for absorption features rapidly varying with wavelength and the index p spans all natural numbers from 0 to the order of the polynomial. Although not stated explicitly, the coefficients of the polynomial (b_p) also depend on the observation conditions.

Equation 3.4 represents the forward model in the standard DOAS approach for the measured spectral radiances within the fitting window. Retrieval of the slant columns of the differential absorbers, i.e. the quantities of interest, constitutes an inverse problem.

The most common approach to solve the problem is to linearize equation 3.4 by taking the logarithm, getting the optical density (*OD*), in the form:

$$OD(\lambda) = \ln\frac{I_0(\lambda)}{I(\lambda,\theta)} = \sum_{j=1}^{J}\sigma'_j(\lambda)SC_j(L) + \sum_p b_p\lambda^p \tag{3.5}$$

The importance of this DOAS equation lies on the fact that if optical densities are computed for several wavelengths, the resulting system of equations is linear with the slant columns of the absorbers considered within the fitting window and the coefficients of the polynomial as unknowns. The equation can be inverted performing a linear fit within the selected window. As the system is overdetermined, the selection of the optimal solution relies on finding the model parameters that yield optical densities in Equation 3.5 that best adjust to the measured optical densities.

The absorption cross sections for the trace absorbers are input for the model and computed in laboratory measurements; the narrowband-broadband structure separation can be done within the fitting process as explained, or prior to it, e.g. by high filtering the measured signal in advance. The slant column densities obtained this way can be interpreted as apparent columns, which are, in turn, the intensity weighted average of all slant columns along each possible light path. Note that this concept differs slightly from the definition in Equation 3.3, which interprets the slant column as the amount of absorber integrated along the most likely light path in the atmosphere.

To correct for the Ring effect a modelled cross section for rotational Raman scattering is introduced in the inversion procedure, in analogy to the absorption cross sections of trace gases in equation 3.5. Similarly, as in the case of slant columns, the scaling factor that accounts for the degree of filling-in of the Fraunhofer structures is given by the fit.

For the retrieval of slant column densities by means of equation 3.5 no additional information is needed. However, slant column densities *per se* do not give useful absolute information, due to their dependence on the light path. Instead, the desired quantity is the vertical column of the target gas, that is, the integrated concentration of absorber along a vertical line from the top of the atmosphere to the ground. The vertical column is related to the retrieved slant column through the Air Mass Factor (AMF), and it is in the calculation of this factor when assumptions on the state of the atmosphere have to be made, especially for scattered light DOAS applications, which correspond to the case at hand.

3.3 Air Mass Factor

The air mass factor establishes the relation between the slant column, as retrieved from the inversion of the DOAS equation, and the quantity of interest, the vertical column of the trace gas:

$$AMF = \frac{SC}{VC} \tag{3.6}$$

For direct light DOAS applications, the light path through the atmosphere is single and known; the AMF can be regarded as the light path enhancement factor with respect to a vertical path in the atmosphere (if the absorber is uniformly distributed), and is often calculated from pure geometrical considerations.

On the other hand, in scattered DOAS implementations the AMF calculation constitutes an additional challenge and a critical second step in the DOAS method. Since the retrieved slant column is actually an intensity weighted average of slant columns along individual light paths, the AMF as well depends on the transmission of radiation through the atmosphere until it reaches the detector. As a result, the AMF will depend on a collection of parameters describing the state of the system: solar position (solar zenith and azimuth angles), viewing geometry of the detection system (line of sight of the objective), vertical profile of the target gas, wavelength (through the effect of scattering and absorption processes), cloud cover and aerosol loading and their positions relative to the absorber, ground reflectance and even flying altitude for aircraft based measurements.

Due to the complexity of a detailed description of the radiation transfer in the atmosphere, taking into account all relevant physical phenomena (scattering, absorption, refraction, reflection processes…), computerized radiative transfer models are used for the AMF calculation. The parameters listed above are therefore necessary for the initialization of the radiative transfer models and imply crucial assumptions on the state of the atmosphere.

In general, the models operate by simulating the radiance reaching the detector under the defined atmospheric and experimental conditions. They might also calculate the weighting functions (W_{ij}), i.e. the first order change in the radiance within an atmospheric layer (i) induced by a change in any of the atmospheric parameters (j). In the case of an optically thin atmosphere (when the radiation transfer equation can be linearized), the computation of the AMF is effected through the computation of the Block Air Mass Factors (BAMF), which are, in turn, defined based on the weighting functions.

The BAMF is a very useful concept for the quantification of the sensitivity of the radiative transfer calculations on the vertical distribution of the target trace gas under the defined experimental conditions. It is defined for a particular height or layer of the atmosphere and quantifies the contribution of the concentration of absorber in the particular layer to the total slant column or to the total AMF.

In an N-layered atmosphere, the BAMF for the *i*-th layer (of geometrical thickness Δh_i and absorber number density n_i), is defined as:

$$BAMF_i = \frac{SC_i}{VC_i} = \frac{SC_i}{n_i \Delta h_i} \tag{3.7}$$

The SC in each particular atmospheric layer (SC_i) is related, through the Beer-Lambert law, to the change in intensity induced by the absorber amount present (i.e. the weighting function of the layer, defined with respect to a change in the absorber number density). Hence, Equation 3.7 can also be rewritten in terms of the weighting functions.

In turn, the total slant column can be expressed as the sum, for all layers, of the individual SC_i:

$$SC = \sum_{i=1}^{N} SC_i = \sum_{i=1}^{N} VC_i \cdot (BAMF_i) = \sum_{i=1}^{N} (BAMF_i) n_i \Delta h_i \tag{3.9}$$

And the total AMF:

$$AMF = \frac{\sum_{i=1}^{N} SC_i}{\sum_{i=1}^{N} VC_i} = \frac{\sum_{i=1}^{N} VC_i \cdot (BAMF_i)}{\sum_{i=1}^{N} VC_i} \tag{3.10}$$

From this last expression, it can be inferred that the BAMF would be identical to the total AMF if all the absorber were concentrated in the considered layer. Also, from its relation to the weighting functions, a vertical profile of BAMF will indicate where in the atmosphere most of the information contained in the measurements comes from and what parts of the atmosphere might be “invisible” given the experimental setup.

Part II:

APPROACH

Contents

4. Airborne Imaging DOAS

A new imaging DOAS (iDOAS) instrument, especially designed for its use on airborne platforms, has been recently developed at the Institute of Environmental Physics (Schönhardt et al., 2011).

The potential of the iDOAS technique lies in the possibility of measuring several Lines Of Sight (LOS) simultaneously, which together with a scanning system allows the retrieval of 2-dimensional distributions of trace gases. Moreover, the iDOAS instrument, when mounted on an aircraft, provides such horizontal trace gas column images with relatively high spatial resolution. This is particularly important for the mapping of pollutants that show large spatial gradients.

Therefore, airborne iDOAS is ideally suited for localization and quantification of closely located gas sources and sinks and for the study of pollutant transport and dispersal in emission plumes. Because iDOAS measurements from aircraft provide information on trace gas variability within a satellite pixel, they constitute a very appropriate link between ground based and satellite measurements and, additionally, may be used for satellite data validation.

The trace gas chosen for testing the new iDOAS instrument is NO_2, an anthropogenic pollutant of great importance (see Chapter 1), due to its very good behaviour in DOAS retrievals, being a well known weak absorber, with very structured absorption features and small interference with other absorbers in the blue part of the visible spectrum. These characteristics provide a framework within which possible instrumental effects affecting the retrieval are easier to recognize. Additionally, the grating iDOAS spectrometer may also be adjusted for measurements in other spectral regions and hence, optimized for future monitoring of species other than NO_2.

First test flights for assessment of the performance of the new iDOAS instrument were conducted during a measurement campaign in June 2011, on board the Polar-5 aircraft, property of the Alfred Wegener Institute for Polar and Marine Research (AWI).

During the test flights, measurements over characteristic NO_2 pollution sources (power plant, highway, oil platform) were carried out. Here, the attention will be focused on the flight over a power plant, being a large and well defined point source.

4.1 The iDOAS instrument

Roughly, passive DOAS instruments consist of a collecting telescope connected to a spectrometer/detector system, often through a quartz fibre bundle.

The use of a bundle of fibres allows the arrangement of the fibres such that the conjunct fits simultaneously the exit of the telescope at one end and the entrance slit of the spectrometer at the opposite end. This is also very useful for imaging spectroscopy as the radiation collected from different viewing directions can be fed into the spectrometer conserving the spatial arrangement, and constitutes a very special feature of the new iDOAS instrument. In addition, most quartz fibres can scramble the polarization of the light, which is a great advantage since the sensitivity of the detection system might vary depending on the polarization state of the radiation.

The principle of the spectrometer is to separate the collected light into its different wavelength components. Essentially two types of dispersive elements are used for the purpose: prisms and gratings. Often grating spectrometers are chosen, as they provide approximately linear dispersion and high resolution; their main disadvantage, though, is that different spectral orders are dispersed and overlapped in a single direction. However, in practice, a great part of the energy will be diffracted in only one order, depending on the spectral range in focus; for instance, when measuring around 400nm, the higher orders present will correspond to radiation of much smaller wavelengths, which is hardly present at tropospheric level.

In imaging spectroscopy, radiation is simultaneously collected from several LOS (or viewing directions) and therefore, the dispersion direction in the spectrometer needs to be perpendicular to the imaging direction in order to conserve all the information. The retrieval of the spectral information for each LOS may be done using different methods. “Whiskbroom” spectrometers record the spectrum for a single spatial pixel at a time, meaning that the measurement time will depend on the total number of pixels, as a scanning through all the LOS is needed. “Pushbroom” spectrometers, on the other hand, simultaneously image all spatial pixels in one direction on the focal plane and disperse their spectral information in the perpendicular direction. This arrangement substantially reduces the measurement time but involves the need of a two-dimensional detector at the focal plane of the spectrograph to record the information. For this purpose, CCD arrays are used, and the result of a single measurement is an image with n_x spectral pixels in the dispersion direction and n_y spatial pixels in the direction of the entrance slit.

The new airborne iDOAS instrument (Schönhardt et al., 2011) consists of a temperature stabilized Czerny-Turner (grating) spectrometer, with 300mm focal length, optimized for the blue part of the visible wavelength region (420-460nm).

The scattered light collected by a downward looking telescope located at the bottom of the aircraft is fed to the spectrometer through a bundle of 38 optical fibres. These fibres are conveniently arranged along the height of the entrance slit (8.5mm) of the spectrometer, but only 35 of them are imaged onto the CCD detector (which has a height of 8.2mm), each constituting a potential viewing direction (Figure 4.1 (left)).

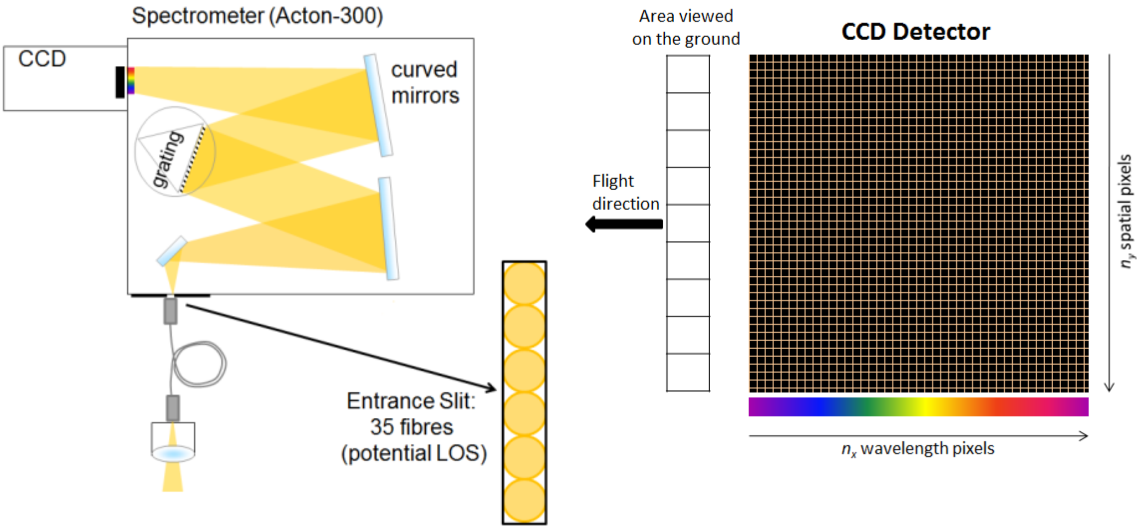

Figure 4.1: Grating spectrometer and entrance optics: telescope, quartz fibre bundle and slit (left); two-dimensional CCD detector: recording of spatial and spectral information (right). (Sketches adapted and extended from Schönhardt et al., 2011)

The entrance slit is placed such that the swath observed on the ground is perpendicular to the flight direction. The total instantaneous Field Of View (iFOV) of the system is generally determined by the focal length (8mm) and the dimensions of the entrance slit.

The scattered light that lies inside the FOV is spectrally dispersed and recorded, preserving the spatial information, by a CCD detector with 512 pixels in each direction (Figure 4.1 (right)).

Furthermore, the detector implemented is a frame transfer CCD, provided with a non-illuminated area (containing as many cells as the area exposed to light) to which the charge is rapidly transferred after the exposure time. The readout process takes place in the darkened area and meanwhile the exposed area is collecting light again, so that measurements can be continuously taken with no delay in between; also a very remarkable feature of the iDOAS instrument.

The slit functions of the spectrometer for each of the viewing directions are computed from line measurements with an HgCd spectral lamp as source (Mercury emission blue line at 435.8nm). A grating line density of 600l/mm and a slit width of 100µm result in spectral resolutions (Full Width at Half Maximum, FWHM) from 0.7 to 1.0nm, depending on the viewing direction (centre to sideward view, respectively) and for the aforementioned wavelength range.

Figure 4.2 shows an image of the CCD matrix for the Mercury line measurements (left) and the derived slit functions for the case of a total of 9 viewing directions (right). Note how the slit function varies with spatial direction as expected. The slit fuction remains unchanged along the spectral axis (Schönhardt et al., 2011).

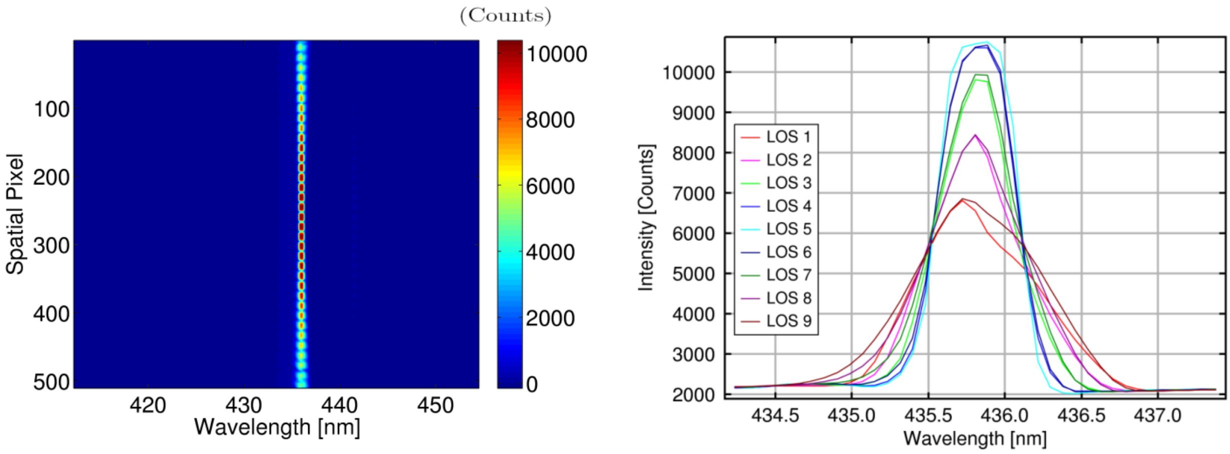

Figure 4.2: Spectrometer slit functions from line measurements with a HgCd spectral lamp; spectrometer image for Hg blue line at 435.8nm, color-coded as a function of intensity (left) and derived slit functions for 9 VD (right). (Source: Schönhardt et al., 2011)

4.2 Observation and viewing geometry

The iDOAS instrument is conveniently framed for its assembly on board of the aircraft. It includes two viewing ports in nadir arrangement: the spectrometer objective and a picture camera (Figure 4.3).

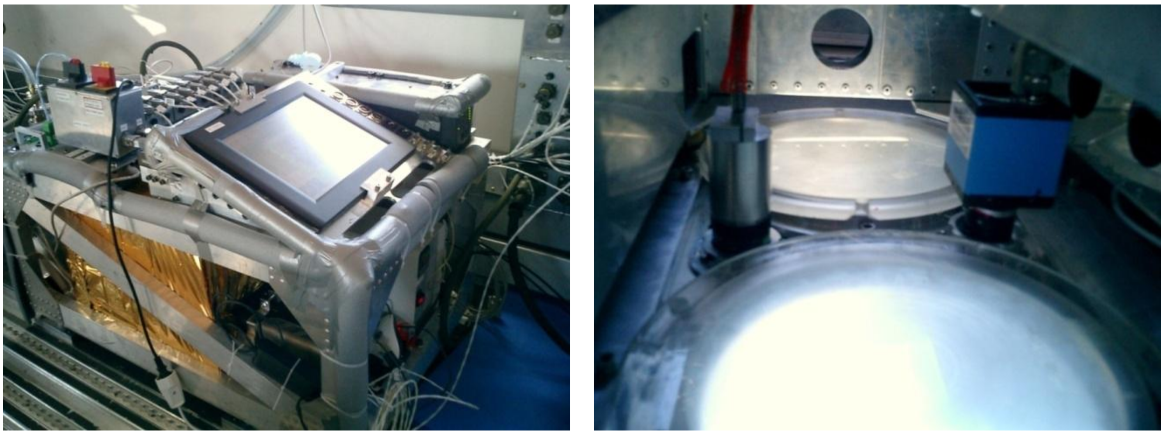

Figure 4.3: The iDOAS instrument framed and mounted on board of Polar-5 aircraft (left).Two nadir ports of the instrument; the objective and the picture camera (right). (Source: Schönhardt et al, 2011)

As explained before, the instantaneous FOV of the instrument is generally determined by the dimensions and shape of the entrance slit of the spectrometer. In the present case, however, the CCD height along the entrance slit is smaller than the slit height itself and will therefore act as the limiting dimension for the iFOV across flight direction. On the other hand, the iFOV along flight direction is effectively determined by the width of the entrance slit. Due to a slight magnification of the image in the spectrometer, the effective focal length is 9.2mm and, in accordance, custom measurements on the iFOV (Bernhardt et al, 2010) yielded values of 48º across flight track (θ) and 3º along track (γ), which are depicted in Figure 4.4.

The total FOV is given by the sum of all iFOV scanned during the measurement time. In a first approximation, the FOV is projected on the ground as a rectangular area divided in as many pixels as viewing directions are considered. As seen in Figure 4.4 the size of the pixels along flight direction is equal to the flight speed times the exposure time. The central point of each ground projected pixel determines the LOS for the corresponding viewing direction.

Given the operation of the iDOAS instrument, a set of spectral recordings is obtained per each measurement, one per pixel or LOS. The maximum number of LOS per measurement is 35; i.e. equal to the total number of optical fibres available. However, the information collected in several adjacent fibres might be averaged (e.g. down to a total of 9 LOS), decreasing the number of LOS and the spatial resolution, but increasing the Signal-to-Noise Ratio (SNR).

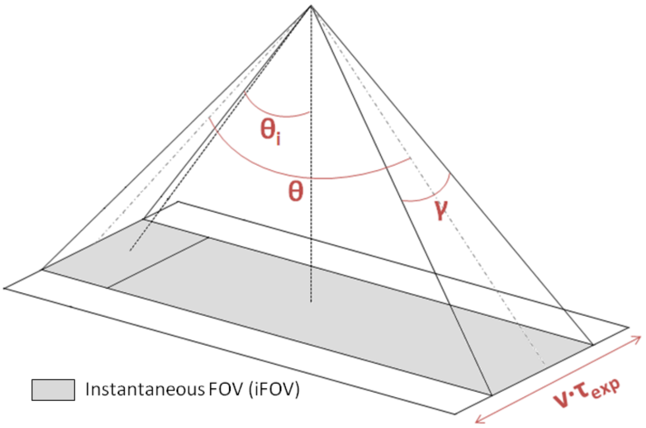

Figure 4.4: Sketch of the ground projected FOV and the iFOV of the iDOAS instrument; characteristic angles of the viewing geometry; aperture angles θ (across track) and γ (along track) and angle θ_i defining the LOS for an extreme pixel.

Now, for an appropriate geolocation of the pixels, that is, to assign the information collected to the precise area imaged on the ground, their location and shape has to be corrected taking into account movements of the aircraft other than the simple flying direction (heading). These additional movements are quantified through the pitch and roll angles, see Figure 4.5.

The aircraft can be considered as a coordinate system, with the origin located at the centre of mass, the z axis looking downward and the x axis pointing in the direction of flight. Rotations of the airplane around the z axis (yaw motions) determine the heading of the airplane with respect to the Earth, that is, the direction of flight. Movements leaving the x axis unchanged are regarded as roll motions (swinging of the aircraft) while pitch movements (nodding) correspond to rotations with invariant y axis.

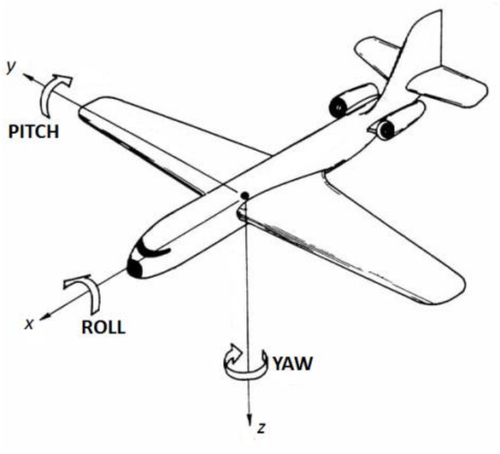

Figure 4.5: The aircraft as a coordinate system: pitch, roll and yaw angles. (Source: Pointing an instrument on an airborne platform; mtp.mjmahoney.net/www/notes/pointing/pointing.html, by MJ Mahoney)

An AIMMS-20 system, on board of the Polar-5 aircraft, provides on flight information about aircraft angles as well as flight speed and altitude, aircraft positioning and meteorological variables of interest (temperature, relative humidity, pressure, wind speed and direction). For the purpose, the AIMMS-20 system consists of four main modules: an air data probe, an inertial measurement unit (3 accelerometers and 3 gyrometers), a GPS module and a data processing unit.

4.3 Light transmissivity and expected SNR

As pointed out before, the scattered light that lies inside the FOV of the iDOAS instrument is collected by the telescope and fed into the spectrometer, where it is spectrally dispersed and imaged into the CCD array detector.

However, the number of photons per measurement collected in each pixel of the detector will depend not only on the spectral radiance of the scattered light and on the exposure time (duration of the measurement), but also on the optical characteristics of the elements that set up the objective-spectrometer system. The optical elements placed within the light path inside the instrument will affect the transmission of the radiation. Moreover, the number of photons reaching a pixel in the detector will be translated into electrons in the interaction with the semiconductor, into a voltage in the readout process and finally into counts (or Binary Units, BU) in the Analog-Digital Converter (ADC).

Finding an expression for the number of counts per pixel and per measurement expected at nominal radiation, from theoretical parameters and characteristics of the instrument, is of great importance for two main reasons. First, this theoretical signal may be compared to the level of the signal collected in actual measurements, for the identification of possible light losses in the instrument. Secondly, it might be used to compute the theoretical SNR, a quantity closely related to the possible detection limit of the instrument. Both in the design and operation of the system, it is necessary to ensure that the SNR is high enough for the targeted purpose.

Therefore, the theoretical SNR might also be compared to the SNR derived from measurements in the inversion procedure, which is to be explained in Section 5.3, to detect additional instrumental or methodological effects influencing the measurements; the SNR characterizes the quality of a measurement and determines the ultimate performance of the system.

The list of all parameters used in the following calculations is given in Table 4.1.

Starting with the nominal spectral radiance at the entrance pupil of the objective (L_λ), if A is the area of the ground swath for a single pixel of the CCD detector and H is the flight altitude, then the spectral irradiance traversing the objective lens (B_λ) is given by:

$$B_\lambda = \frac{A}{H^2} L_\lambda \tag{4.1}$$

Figure 4.6 Shows a simplified sketch of the optics of the objective and the relation between the ground projected pixel size and the actual dimensions of the pixel in the CCD detector.

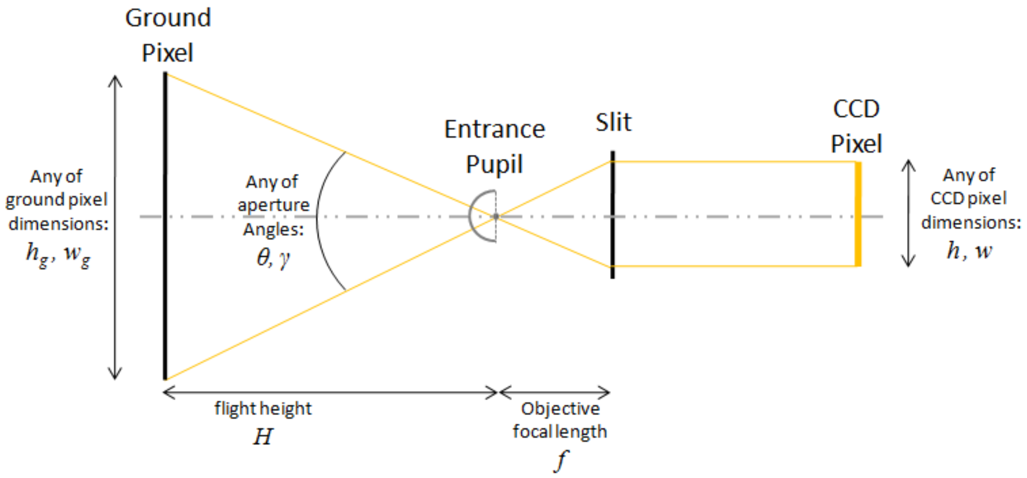

Figure 4.6: Schematic depiction of the optics of the objective; imaging of the FOV onto the corresponding pixel in the CCD detector.

As inferred from Figure 4.6, the ground projected pixel area A, with height h_g (across flight direction) and width w_g (along flight direction), can be written in terms of the CCD pixel dimensions h and w:

$$A = h_g \cdot w_g = \frac{h \cdot w}{f^2} H^2 \tag{4.2}$$

Substituting Equation 4.2 into Equation 4.1 and multiplying by the area of the entrance pupil (A_{obj}) and by the exposure time (τ_{exp}), the number of photons per CCD pixel and per unit wavelength that enter the system during a measurement is obtained:

$$C_\lambda = \tau_{\exp} A_{obj} \frac{h \cdot w}{f^2} L_\lambda = \tau_{\exp} \pi \left(\frac{D}{2} \right)^2 \frac{h \cdot w}{f^2} L_\lambda \tag{4.3}$$

Equation 4.3 can be further simplified by recalling that the diameter of the entrance pupil (D) can be expressed in terms of the f-number (F):

$$C_\lambda = \tau_{\exp} \pi \left(\frac{f}{2F} \right)^2 \frac{h \cdot w}{f^2} L_\lambda = \tau_{\exp} \frac{\pi}{4} \frac{h \cdot w}{F^2} L_\lambda \tag{4.4}$$

Now, to calculate the number of photons that actually hit a single pixel in the CCD detector during a measurement (C), the quantity expressed in Equation 4.4 has to be scaled to account for the transmissivity of light by the optical elements in the system: efficiency of the objective (ε_{obj}), efficiency of the optical fibres (ε_{fib}), efficiency of the grating (ε_{gr}), transmissivity of the CCD window (ε_{win}) and reflectivity of the mirrors (ε_{mir}) for a total of N mirrors in the spectrometer.

Also the linear dispersion ($disp$) of the grating in the spectral direction must be considered, to determine the spectral range that the CCD pixel covers ($disp \cdot w$):

$$C = \frac{\pi}{4} \cdot \tau_{\exp} \cdot disp \cdot \frac{h \cdot w^2}{F^2} \cdot \varepsilon_{fib} \cdot \varepsilon_{gr} \cdot \varepsilon_{obj} \cdot \varepsilon_{win} \cdot \varepsilon_{mir}{}^{N} \cdot L_\lambda \tag{4.5}$$

If the quantum efficiency of the CCD detector (QE_{CCD}) is introduced as a multiplying factor in Equation 4.5, the number of electrons originated in the CCD pixel by the incident radiation is found:

$$C_{e-} = \frac{\pi}{4} \cdot \tau_{\exp} \cdot disp \cdot \frac{h \cdot w^2}{F^2} \cdot \varepsilon_{fib} \cdot \varepsilon_{gr} \cdot \varepsilon_{obj} \cdot \varepsilon_{win} \cdot \varepsilon_{mir}{}^{N} \cdot QE_{CCD} \cdot L_\lambda \tag{4.6}$$

Finally, the electron-to-BU conversion factor of the ADC ($f_{e\text{-}BU}$) may be used to obtain the desired expression; the theoretical number of counts per CCD pixel and per measurement:

$$C_{BU} = \frac{\pi}{4} \cdot \tau_{\exp} \cdot disp \cdot \frac{h \cdot w^2}{F^2} \cdot \varepsilon_{fib} \cdot \varepsilon_{gr} \cdot \varepsilon_{obj} \cdot \varepsilon_{win} \cdot \varepsilon_{mir}{}^{N} \cdot QE_{CCD} \cdot f_{e-BU} \cdot L_\lambda \tag{4.7}$$

Equation 4.6 and 4.7 can be generalized for the possibility of using binned pixels, when spatial (bin_h; SNR improvement) or spectral (bin_w; e.g. spectra smoothing) information is to be averaged. For the present case, the minimum spatial binning allowed is 512/35; i.e. the total number of spatial pixels divided by the maximum number of viewing directions (number of optical fibres).

$$C_{BU}^{bin} = \frac{\pi}{4}\cdot\tau_{\exp}\cdot disp\cdot\frac{bin_h h(bin_w w)^2}{F^2}\cdot\varepsilon_{fib}\cdot\varepsilon_{gr}\cdot\varepsilon_{obj}\cdot\varepsilon_{win}\cdot\varepsilon_{mir}{}^{N}\cdot QE_{CCD}\cdot f_{e-BU}\cdot L_{\lambda} \qquad (4.8)$$

Table 4.1 gives the list of all variables and parameters involved in the theoretical calculation of the number of counts per measurement and per binned pixel expected at nominal radiation, Equation 4.8, as well as their values for the iDOAS instrument.

Symbol	Name	Value	Units
L_{λ}	Spectral nominal radiance	From radiative transfer	$Phot\ s^{-1}\ nm^{-1}\ cm^{-2}\ sr^{-1}$
τ_{exp}	Exposure time	Adjustable	*Sec*
h	Pixel height	16	*Mm*
bin_h	Spatial binning	Adjustable	--
w	Pixel width	16	μm
bin_w	Spectral binning	Adjustable	--
F	f-number	3.9	--
ε_{win}	Transmissivity of CCD window	0.96	--
ε_{obj}	Objective efficiency (440nm)	0.75	--
ε_{fib}	Fibre transmissivity	~0.50	--
ε_{gr}	Grating efficiency (430nm)	0.80	--
$disp$	Grating linear dispersion	0.005	$nm/\mu m$
N	Number of mirrors	3	--
ε_{mir}	Mirror reflectivity	~0.99	--
QE_{CCD}	CCD Quantum Efficiency (430nm)	0.75	*e-/phot*
$f_{e\text{-}BU}$	Conversion factor e- to BU	1.66	*BU/e-*
N_{shot}	Shot noise	Signal level dependent	*e-*
$N_{readout}$	Readout noise RMS (5MHz)	45	*e-*

Table 4.1: notation and names for the relevant variables and parameters used in the theoretical SNR calculation; given are parameter values for the IDOAS instrument.

Having an expression for the theoretical signal collected in the CCD, the SNR can be easily derived from an additional calculation of the level of noise. Three main sources of noise can be identified in the CCD system:

- **Shot noise** (N_{shot}) arises from the statistical nature of the process of photon detection; the number of electrons freed at the detector follows a Poisson distribution and thus appears fluctuations with a standard deviation of the square root of the intensity measured. It is commonly expressed in units of e- generated in the detector:

$$N_{shot} = \sqrt{C_{e-}} \tag{4.9}$$

· **Thermal noise** accounts for the extra electrons generated in the CCD from physical processes other than the simple absorption of photons. Hence, thermal noise is often also referred to as dark current. The dark current is related to temperature effects, since thermal motions of the particles in the detector material can set electrons free even in absence of light. Thermal noise depends on the fabrication properties and operation mode of the CCD but can also be reduced by keeping the CCD at a low temperature during the measurement. In the present calculation, the dark current is measured and accounted for in the calibration procedure of the measured spectra, prior to the DOAS inversion. Small fluctuations in the dark current are not taken into account, assumed to be very small if the detector is cooled to a rather low temperature.

· **Readout noise** is generated in the readout process of the charge generated in the detector pixels. The charge in each pixel is systematically transferred onto the output node of the CCD, where the change in voltage caused by this charge is sensed by the on-chip amplifier. The readout noise generated in the on-chip amplifier increases with increasing sampling frequency (rate at which each pixel is read). Table 4.1 gives the readout noise RMS level ($N_{readout}$) for the chosen sampling frequency in the case of the iDOAS instrument.

The theoretical SNR at nominal radiation can be computed, then, from the signal level given by Equation 4.6 and the readout and shot noise, assuming they constitute independent sources of error:

$$SNR\big|_{nom} = \frac{C_{e-}}{\sqrt{N_{shot}{}^2 + N_{readout}{}^2}} = \frac{C_{e-}}{\sqrt{C_{e-} + N_{readout}{}^2}} \tag{4.10}$$

In many cases, the readout noise in Equation 4.10 is negligible and the theoretical RMS is approximately equal to the shot noise; the square root of the measured radiation signal:

$$SNR\big|_{nom} \approx \frac{C_{e-}}{\sqrt{C_{e-}}} = \sqrt{C_{e-}} \tag{4.11}$$

5. iDOAS Data Analysis

The data from iDOAS measurements is stored in large binary files. These files are called image files, since they contain the images of the data collected in the CCD detector for several measurements. That is, they include an entry per performed measurement. Each of these entries stores the number of counts per second collected in each of the 512x512 pixels in the detector, plus an adequate header indicating relevant parameters (such as the date, the measurement time interval, exposure time, solar angles, etc).

The first step in the iDOAS data analysis consists of adequately separating the spatial and spectral information of the measurements. This is done splitting the image file into a set of smaller files, one per LOS to be considered. The splitting procedure implies averaging the information along the spatial direction down to a total of 35 or 9 LOS, depending on the user's choice. In principle, other choices are also possible but for the moment only these two have been implemented. Note that the splitting and averaging has also to be done for the image files containing dark signal and HgCd lamp line measurements.

Each of these smaller files contains again one entry per measurement but, in this case, these store only the spectral information. Naturally, these spectra are conveniently ordered according to the time of the measurement. The entries also include an appropriate header, again indicating the corresponding date, measurement time, exposure time and solar angles among others.

In parallel with the splitting and averaging, also the computation of the ground pixel geolocation is done. In the case of the atmospheric measurements, the headers additionally contain the corner and centre coordinates (as well as the derived LOS angle) of the ground pixel to which the spectral information is to be assigned. Such computation takes into account the pitch and roll motions of the aircraft affecting the shape of the ground projected FOV. The positioning data needed for the pixel geolocation is obtained from the data file provided by the AIMMS-20 system, through time synchronization between iDOAS and AIMMS-20 measurements.

In a second step of the data processing, each of the LOS files goes into a calibration procedure, in which the dark signal is subtracted and all the spectra are calibrated as a function of wavelength instead of pixel number.

The resulting post calibration files are then ready for the DOAS fitting procedure, which yields the slant column values of the absorbers considered and their uncertainties, as well as the residual spectrum for each measurement. A particular background spectrum is used for each LOS and, in turn, individual fittings are performed for all measurements in each LOS.

The following sections present descriptions of the pixel geolocation correction, of the calibration procedure and of the DOAS fitting routine in more detail. Also, the analysis of the residual spectra and the operation of the radiative model used for the calculation of AMF are described.

5.1 Correction of pixel Geolocation

For the imaging procedure, the area viewed on the ground is divided into several pixels, each corresponding to a particular LOS. The objective is to calculate the corner and centre geographic coordinates of each of those pixels, taking into account that the aircraft performs pitch and roll motions that displace and distort the ideal rectangular ground swath (that with centre of the FOV located immediately below the airplane).These calculations, which are detailed in the following lines, have been implemented through MATLAB code programming.

Pitch, roll and yaw angles at the start and at the end of each measurement are known by making use of GPS time synchronization.

Note that because there is no time lapse between consecutive measurements, the angles at the end of one measurement coincide with those at the beginning of the next one. Therefore, one possibility consists on calculating two corner coordinates of the pixel using the angle data at the start and the other two from the data at the end of the measurement, as sketched in Figure 5.1. This means that the variation of the aircraft angles within a measurement is not neglected but approximated as linear. The FOV along track is, in this case, assumed to be negligible, and the iFOV is a line perpendicular to the flight direction (i.e. the angular aperture along flight track is not considered).

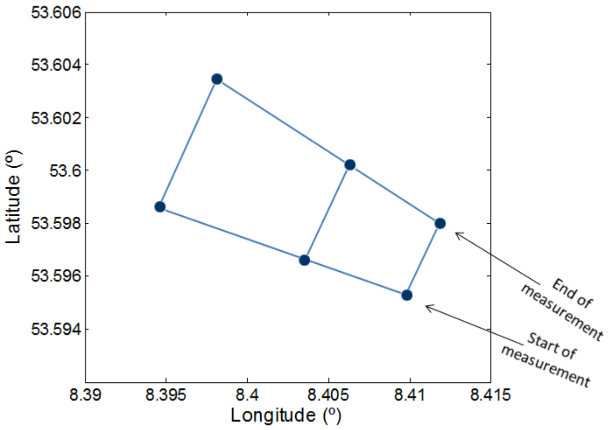

Figure 5.1: Determination of pixel geolocation from their extreme corners at the start and the end of the measurement; amplified view for only two LOS (pixels).

In order to locate the two pixel corners corresponding to the start of the measurement, first their coordinates are computed with respect to a reference system rotated by an angle given by the yaw (whose origin is located at the point directly below the aircraft). The computation is done independently for each of the two points, through trigonometric relations, using the known values of altitude (H), pitch and roll angles and relative angular distance from the point to the center of the FOV (LOS_{ind}), see Figure 5.2. The latter is derived from the total FOV (48°) and the number of pixels, and is positive for pixels located to the right of the FOV center (with the flying direction as reference).

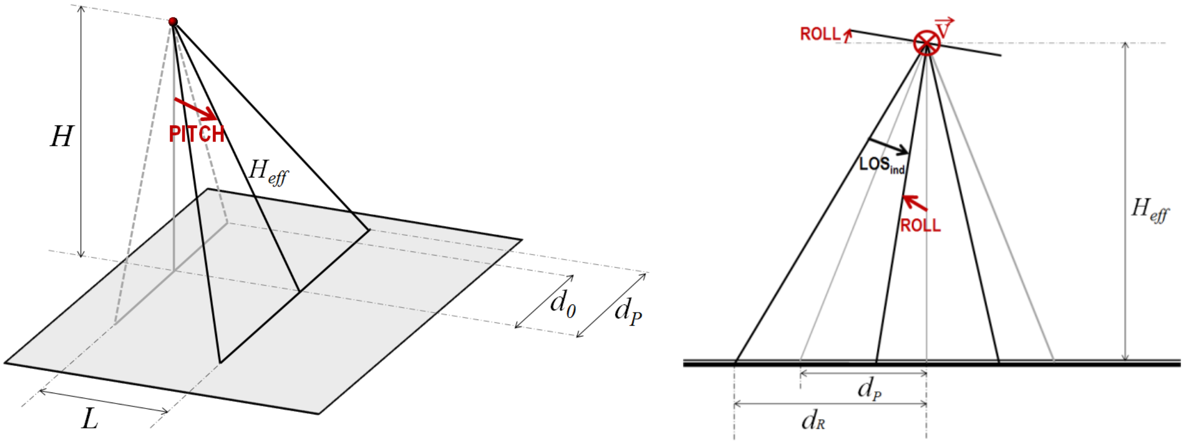

Figure 5.2: Effect of pitch (left) and roll (right) motions on the ground projection of the FOV.

Therefore, the coordinates with respect to the rotated reference system are calculated as:

$$L = H\tan(PITCH) \tag{5.1}$$

$$d_R = H_{eff}\tan(LOS_{ind} - ROLL) = \frac{H}{\cos(PITCH)}\tan(LOS_{ind} - ROLL) \tag{5.2}$$

Once L (displacement of the pixel corner along flight direction) and d_R (displacement across flight direction) coordinates are known, the point is located with respect to the Earth's system by inverting the rotation given by the yaw angle and by adding the coordinates of the aircraft ($Long_0$, Lat_0). Because the coordinates L and d_R are computed in meters, in order to express them as latitude and longitude angles the spherical shape of the Earth has to be taken into account:

$$\begin{bmatrix} Long_E \\ Lat_E \end{bmatrix} = \frac{180}{\pi}\begin{bmatrix} \frac{1}{R}\cos(YAW) & \frac{1}{R}\sin(YAW) \\ -\frac{1}{R_0}\sin(YAW) & \frac{1}{R_0}\cos(YAW) \end{bmatrix}\begin{bmatrix} d_R \\ L \end{bmatrix} + \begin{bmatrix} Long_0 \\ Lat_0 \end{bmatrix} \tag{5.3}$$

With: $R = R_0\cos(Lat_0)$; R_0: *equatorial radius of the Earth*

This procedure is applied for both extremes of the pixel (because they have different LOS_{ind}) and both at the start and end of measurement to obtain all four corner coordinates. The centre coordinate, which will actually determine the LOS for the pixel, is calculated as the "centre of mass" of the system of four coordinates.

Spatial resolution

The present calculation of the field of view on the ground implies that each of the pixels has a different area, which is, in turn, different for each measurement; the spatial resolution depends both on the pixel and on the measurement considered.

The dimensions of the swath, both along and across the flight direction, increase with increasing height and pitch and roll angles. Provided that generally the pitch angles are small and the flight altitude is approximately constant, the major contribution to the change in spatial resolution across the flight direction is from the roll motions, especially for sharp bends in the trajectory of the airplane. Because the angular aperture of the instantaneous FOV along flight track is not considered, the main factors affecting the resolution in this direction are the cruising speed and the exposure time. However, neglecting this angular aperture leads to some overestimation of the spatial resolution (see Section 7.3).

Taking now this aperture angle into account, the shape of the ground projected iFOV does not coincide with that of the entrance slit. Due to the pitch and roll motions, the iFOV acquires a more complex shape, similar to the one pictured in Figure 5.3. As a result, the total FOV during a measurement, and in particular its dimension parallel to the flight direction, is actually larger than the one that is being considered when approximating the ground iFOV as a single line. The appropriateness of taking this approximation when calculating the pixel geolocation will depend on the magnitude of the overestimation in spatial resolution that it implies. And the magnitude of the overestimation will, in turn, be mostly influenced by speed and altitude flight characteristics.

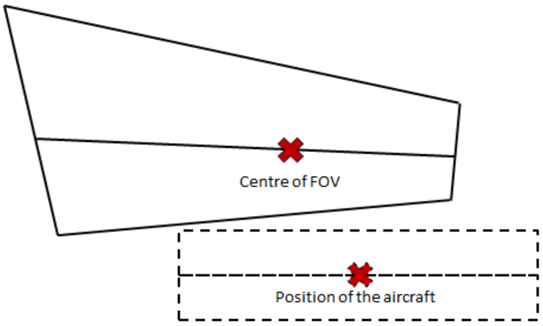

Figure 5.3: Ground projected iFOV when considering the angular aperture along flight direction: with positive (solid line) and zero (dotted line) pitch and roll angles.

5.2 Spectra calibration and DOAS fitting

After the convenient splitting of the image files and application of pixel geolocation, a set of multi-spectra files are left, one per each LOS or viewing direction. Indeed, three of these sets are needed for the subsequent data analysis: one with the atmospheric measurements, another with the dark signal measurements and a third with the line measurements.

Before entering the DOAS fitting procedure, these spectra have to undergo a calibration routine. The software package used for the data analysis has been developed and refined by Andreas

Richter at the IUP Bremen (Richter A., 1997). A flow chart of the data analysis steps is displayed in Figure 5.4.

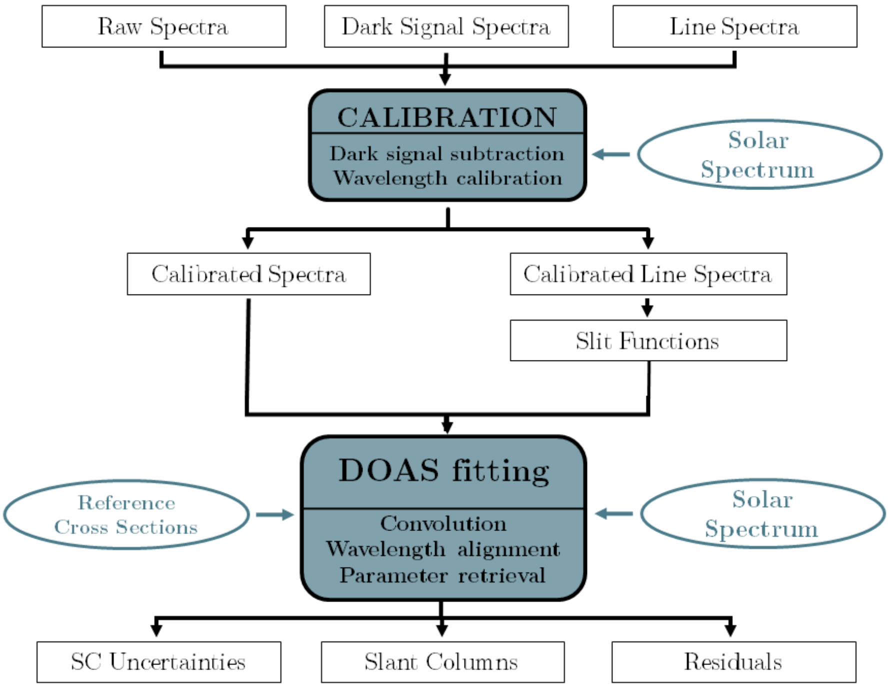

Figure 5.4: Flow chart of the DOAS data processing steps and software: spectra calibration, computation of slit functions and DOAS fitting.

Spectra calibration

The main purpose of the calibration procedure is to set a wavelength axis both for the atmospheric spectrum and for the line spectrum, which are recorded as a function of the spectral pixel number. The calibration is done by means of an appropriate software, which first subtracts the corresponding dark signal from the measured spectrum and then performs the pixel-wavelength assignment, using the Fraunhofer structures from an input solar spectrum (Kurucz solar FTS scan measured at Kitt Peak observatory).In a second step, the calibrated line spectrum is processed to derive the corresponding slit function.

DOAS fitting

The DOAS fitting is performed by means of specifically addressed software. The main purpose of the inversion algorithm is to fit the DOAS equation (Equation 3.5) to the measurements, in order to retrieve optimal values for the forward model parameters, i.e. for the SC of the differential absorbers and for the coefficients of the polynomial accounting for broadband spectral structures. The software allows the choice of a large number of fitting modes and parameters. Here only the fitting mode to be followed in the subsequent NO_2 retrieval is described.

Necessary input data for the fitting routine are the calibrated measurement spectrum (I), an adequate background spectrum (I_0), the slit function file, a Fraunhofer solar atlas (as the one used in the calibration procedure), reference spectra of the cross sections for the differential absorbers and a theoretical Raman scattering cross section (Ring spectrum).

The absorbers to be included in the fitting are those that show, within the fitting window, absorption structures strong enough to be detected by the instrument. The reference absorption spectra are convoluted with the instrument slit function prior to the inversion. This is also the case for the Ring spectrum, which is treated as a further absorber.

Besides, an additional synthetic cross section is included in the fitting to account for the effect of a possible constant offset in the measured spectrum. Such a constant offset (c) might be often attributed to the presence of stray light[*] in the instrument. The corresponding synthetic cross section is calculated from the measured spectrum as c/I, by virtue of the following approximation:

$$\ln\left(\frac{I+c}{I_0}\right)=\ln I\left(1+\frac{c}{I}\right)-\ln\left(I_0\right)=\ln\left(\frac{I}{I_0}\right)+\ln\left(1+\frac{c}{I}\right)\approx\ln\left(\frac{I}{I_0}\right)+\frac{c}{I} \qquad (5.4)$$

In the application, however, c is not the constant offset itself, which is in principle unknown, but a stray light factor multiplied by the maximum intensity found in the measured spectrum within the fitting window. The scaling factor determining the magnitude of the offset is estimated in the fitting routine.

It is of great relevance to have a precise wavelength alignment between the measured spectrum and the spectrum used as background, so that taking the ratio I/I_0 successfully eliminates the solar Fraunhofer features present.

Spectral misalignments generally arise as consequence of changes in dispersion in the spectrograph, which are, in turn, caused by the different measurement conditions of the spectra, e.g. variations in temperature and pressure.

To correct for this effect, the wavelength axis of the measurement spectrum is adapted, during the calculations, with reference to that of the background spectrum in a non-linear process. This process is generally referred to as “shift and squeeze” of the measured spectrum.

If the reference cross sections are well calibrated no further “shift and squeeze” is needed.

Since the spectral axis of the background spectrum is used as reference for the “shift and squeeze” procedure, it is also very important to have a fine calibration for this spectrum. Therefore, a

---

[*] Instrumental stray light refers to the presence of light that, without going through the dispersion procedure or proceeding from other sources than the intended one, also reaches the detector. Stray light is generally assumed to be constant (or linearly increasing) in intensity.

refinement of the wavelength calibration in the background spectrum is also performed prior to the DOAS fitting, by running a non-linear fit of this spectrum to the Fraunhofer atlas.

In a general overview, the fitting algorithm consists of two main steps: a nonlinear fit for the spectral alignment of the measured spectrum and a linear fit to invert the DOAS equation. The process starts with a performance of a first step of the nonlinear fit from fixed initialization parameters. The “shift and squeeze” parameters obtained in the nonlinear calibration step are then used for the linear fit. This procedure is repeated until a convergence criterion is met in the linear fit; usually when the relative change in Chi-square value (χ^2) between consecutive steps is smaller than a given value. The χ^2 value is the cost function in the linear inversion method; i.e. the sum of all the squared residuals (differences between measurements and model, see next section). The parameters found in the last iteration of the linear fit constitute the best estimation, under the particular measurement conditions and retrieval settings, of the slant columns of the differential absorbers present.

The fitting window, the differential absorbers present, the “shift and squeeze” fitting mode, the initial stray light factor, the number of coefficients in the polynomial in the DOAS equation and the χ^2 limit are some of the fit parameters that the user may change within the fitting routine.

5.3 Residual spectra

The DOAS inversion algorithm gives an estimate of the slant column values and their uncertainties.

A very important concept in the evaluation of the goodness of such estimation is the residual of the fitting. The residual is defined for each measurement in the spectrum and quantifies the difference between the measured intensity value and the value given by the estimated forward model. This definition leads to a spectrum of residuals for the particular fit.

For example, if the forward model is expressed as an arbitrary function of the vector of retrieved parameters, $F(\vec{\boldsymbol{x}})$, and the vector of measurements is denoted as $\vec{\boldsymbol{y}}$, the residual of the fit at the i-th wavelength of the fitting window is given by:

$$R_i = F_i(\vec{x}) - y_i \tag{5.5}$$

The value of the cost function of the fit is given by the sum of all the squared residuals within the fitting window. The cost function is commonly expressed as χ^2 because, if the residuals are normally distributed and uncorrelated, it has a chi-squared distribution with N degrees of freedom, with N as the total number of spectral measurements in the fitting window.

$$\chi^2 = \sum_{i=1}^{N} R_i^2 = \sum_{i=1}^{N} \left[F_i(\vec{x}) - y_i\right]^2 \tag{5.6}$$

The average standard deviation of the measurements with respect to the model is quantified by the Root Mean Square (RMS) of the residuals:

$$RMS = \left[\frac{1}{N}\sum_{i=1}^{N} R_i^2\right]^{1/2} = \sqrt{\frac{\chi^2}{N}} \tag{5.7}$$

Intuitively, the desire is to get the smallest RMS possible for the fit. This is supported by the fact that the RMS of the residuals is the inverse of the actual SNR and therefore determines the detection limit of the instrument plus method.

Indeed, the ideal result is to have a residual spectrum which resembles that of pure noise, with spectral structures generally not wider than a wavelength channel. In such a case, the SNR derived from the RMS is expected to be very close to the theoretical SNR calculated in Section 4.3 (Equation 4.11), since the photon noise dominates the measurements. Actually, in that case, the RMS should be a very good estimator of the σ-level of the statistical noise.

However, often structures other than pure noise are found in the residual spectrum, spanning several wavelength channels. These structures occur at random in most of the cases and their main effect is an underestimation of the error in the retrieved slant columns (Stutz and Platt, 1996).

Systematic structures, on the other hand, can seriously compromise the accuracy of the retrieved columns and the appearance of such features poses a limit to a possible further improvement of the SNR. Moreover, it is important to keep in mind that there might also be systematic contributions to the error which are not reflected in the residual spectrum.

The cause of residual structures, although generally unknown, has been often attributed to effects such as spectral misalignments, variable response of the detector to changes in illumination, stray light in the detector and inaccuracies in the slit function shape or in the reference spectra. Since the cause of the structures is many times linked to instrumental effects, it is very important in this respect to check the performance of the instrument.

5.4 AMF computation: SCIATRAN

The SCIATRAN radiative transfer model (RTM) has been developed at the Institute of Environmental Physics (IUP, University of Bremen) and constitutes a next generation of the GOMETRAN RTM (Rozanov et al, 1997), which was originally designed to fulfill the requirements of the retrieval algorithm used for GOME instrument (Global Ozone Monitoring Experiment, on board of ERS 2 satellite). In analogy, SCIATRAN RTM (Rozanov et al, 2002) was initially developed for the retrieval of atmospheric constituents from radiance measurements of the SCIAMACHY instrument (Scanning Imaging Absorption spectrometer for Atmospheric CHartographY, on board of ENVISAT satellite).

The SCIATRAN model numerically solves the monochromatic radiative transfer equation (RTE, see Section 2.1). It covers the wavelength range from 175 to 2400 nm, and it allows the selection of several spectral windows. It may include absorption by O_2, H_2O, CO_2, CH_4, CO, N_2O, O_3, NO_2, ClO, OClO, BrO, HCHO, SO_2, NO_3 and O_4 species, as well as all relevant emission features and atmospheric scatterers (molecular scatterers, aerosols and clouds). It accounts for line broadening effects, for multiple and inelastic (Raman) scattering phenomena and for surface reflective properties (wavelength dependent lambertian or bidirectional reflecting surfaces).

Additionally, the RTE numerical solution might be executed for two different atmospheric geometries. The plane-parallel atmosphere approximation, which neglects all effects due to the spherical shape of the Earth, is valid for SZA less than 90° and small LOS angles (Rozanov et al, 2005). The pseudo-spherical mode, on the other hand, takes into account the sphericity of the Earth (and refraction) but only for the computation of the solar source term in the RTE (solar photon flux reaching the first scattering altitude). This last approach yields accurate results for solar zenith angles up to 92°.

SCIATRAN enables the modeling of the radiation field, weighting functions (changes in radiance due to variations in atmospheric parameters at certain altitude locations) and AMFs for a large variety of atmospheric conditions, experimental setups and viewing geometries, through an adequate choice of its numerous internal parameters.

SCIATRAN constitutes a suitable tool for the computation of the AMFs, and, hence, for the derivation of vertical columns, for airborne based measurements that include several off-axis LOS, as is the case for iDOAS measurements from aircraft.

6. Point Source Emissions

Pollutants emitted into the atmosphere are advected over long distances by the mean flow and dispersed by small-scale air-flows or turbulence, which effect the mixing with clean air. Atmospheric dispersion models are mathematical simulations of the physics and chemistry governing the transport, dispersion and transformation of pollutants in the atmosphere. However, a detailed description of turbulent dispersion processes is a complex challenge, due to the presence of differently sized eddies in the atmospheric flow.

Dispersion models are most commonly used to estimate downwind concentrations of contaminants over varying time scales, in order to assess the potential environmental and health hazards of emissions from industrial processes. However they might also be used in a number of relevant applications: assessing compliance of emissions with air quality guidelines and the effectiveness of these, planning new facilities with appropriate stack heights or forecasting pollution episodes among many others.

Even though the choice of an appropriate dispersion model is heavily dependent on the intended application, the most well known and commonly used dispersion models are steady-state Gaussian-plume models. These incorporate a simplistic description of the dispersion process, and some fundamental assumptions. However, even with these limitations, this type of model can provide reasonable results in medium-complex meteorological and topographical conditions.

As pointed out before, aircraft based iDOAS measurements are a very powerful tool for quantification of emission rates and for the study of pollutant transport and dispersal in point source exhaust plumes. This last property is of great utility for the development of advanced pollutant dispersion models.

In turn, the estimation of emission rates might be used for improvement, updating and verification of the available emission inventories. Moreover, the emission rate of the point source constitutes a critical initialization parameter and an important error source for the mentioned models. At this regard, iDOAS measurements can be very helpful and the theoretical considerations that follow are to be used later, specifically to estimate the NO_2 emissions from a power plant stack.

6.1 Gaussian plume model

The basic Gaussian plume model arises as the fundamental solution to the classical Fickian diffusion equation:

$$\frac{dc}{dt} = \vec{K} \cdot \nabla^2 c \tag{6.1}$$

With c the concentration of pollutant and K being the eddy diffusivity vector (non-isotropic medium). The solution of Equation 6.1 for an instantaneous point source that emits a total pollutant amount C is given by the Gaussian formula:

$$c(x,y,z,t)=\frac{C}{(4\pi t)^{3/2}(K_x K_y K_z)^{1/2}}\exp\left(-\frac{(x-ut)^2}{4K_x t}\right)\exp\left(-\frac{y^2}{4K_y t}\right)\exp\left(-\frac{z^2}{4K_z t}\right) \tag{6.2}$$

To consider advection in the direction of the mean flow (x) with constant speed u, it is possible to change to a fixed reference system, so that the variable x is substituted by $x\text{-}ut$.

In order to obtain a steady-state solution for a continuously emitting source, Equation 6.2 has to be integrated for all times. This means that the plume at a particular spatial position is regarded as the time average of an infinite ensemble of instantaneous puffs. For simplicity, diffusion along the advection axis is neglected for the integration, and the final solution yields:

$$c(x,y,z)=\frac{Q}{2\pi\sigma_y\sigma_z u}\exp\left(-\frac{y^2}{2\sigma_y{}^2}\right)\exp\left(-\frac{z^2}{2\sigma_z{}^2}\right) \tag{6.3}$$

Q is the pollutant emission rate and $2K_yt$ and $2K_zt$ have been replaced by the ensemble average displacements of the pollutant particles due to diffusion, σ_y and σ_z respectively.

For continuous emitters within the boundary layer, Equation 6.3 is expanded to account for the effect of reflection of the plume on the ground, assuming an imaginary image source:

$$c(x,y,z)=\frac{Q}{2\pi\sigma_y\sigma_z u}\exp\left(-\frac{y^2}{2\sigma_y{}^2}\right)\left[\exp\left(-\frac{(z-h)^2}{2\sigma_z{}^2}\right)+\exp\left(-\frac{(z+h)^2}{2\sigma_z{}^2}\right)\right] \tag{6.4}$$

Apart from the emission rate Q, the critical input parameters in Equation 6.4 are the statistical variances σ_y and σ_z and the effective stack height h, which is the sum of the physical stack height and the plume rise.

The statistical variances will have different values depending on the position x along the advection axis. Moreover, they are characterized by quantities such as terrain roughness and friction velocity, wind speed and wind direction fluctuations and atmospheric stability (mechanical and thermal turbulence). These variances have been historically derived both from theoretical and empirical approaches. In particular, Briggs derived a series of formulas based on previous empirical schemes (Briggs, 1973) that have proven to work well in medium roughness terrain conditions and for moderate atmospheric stability cases. These formulas, for σ_y and σ_z as a function of distance to the source, are compiled in Table 6.1, for open country conditions and classified according to Pasquill stability classes.

The plume rise is the altitude above the stack at which the plume becomes level. It depends on parameters like atmospheric stability, stack gas exit velocity, atmospheric and gas exit temperatures, stack diameter and wind speed. The most widely used equations for plume rise computation are again due to Briggs, who derived them from fluid dynamics considerations (Briggs, 1975). According to this formulation, the plume rise (Δh) is given by:

$$\Delta h = 2.6 \cdot \left(\frac{F_0}{uS} \right)^{1/3} \tag{6.5}$$

Here, F_0 is the initial buoyancy flux and S is the ambient stability parameter:

$$F_0 = w_0 R_0^{\ 2} \frac{g}{T_{p0}} \left(T_{p0} - T_{e0} \right) \tag{6.6}$$

$$S = \frac{g}{T} \left(\frac{\partial T}{\partial z} + \Gamma_d \right) \tag{6.7}$$

Where w_0 is the exit velocity of the stack gases, R_0 is the stack radius, g is the gravity acceleration, T_{p0} is the gas exit temperature, T_{e0} is the ambient temperature at stack height and Γ_d is the dry adiabatic lapse rate (0.0098 K/m). The ambient temperature gradient in Equation 6.7 and the wind speed (u) in Equation 6.5 correspond to average values over the expected height of the plume.

Class	**Description**	$\boldsymbol{\sigma_y}$ **[m]**	$\boldsymbol{\sigma_z}$ **[m]**
A	Extremely unstable	$0.22x(1+0.0001x)^{-1/2}$	$0.20x$
B	Moderately unstable	$0.16x(1+0.0001x)^{-1/2}$	$0.12x$
C	Slightly unstable	$0.11x(1+0.0001x)^{-1/2}$	$0.08x(1+0.0002x)^{-1/2}$
D	Neutral	$0.08x(1+0.0001x)^{-1/2}$	$0.06x(1+0.00015x)^{-1/2}$
E	Slightly stable	$0.06x(1+0.0001x)^{-1/2}$	$0.03x(1+0.0003x)^{-1}$
F	Moderately Stable	$0.04x(1+0.0001x)^{-1/2}$	$0.016x(1+0.0003x)^{-1}$

Table 6.1: Recommended formulas for horizontal and vertical variances as a function of distance to the source (x) for the Gaussian plume model, in open country conditions and classified according to Pasquill atmospheric stability classes. (Briggs, 1973)

Finally, it is important to keep in mind the main assumptions and approximations behind the Gaussian plume model:

(i) Emission duration must be greater than plume travel time in order for the diffusion in the advection direction to be negligible.

(ii) A constant wind speed is assumed although it actually changes in speed and direction within the boundary layer, as predicted by the Ekman spiral. Besides, the model breaks down for very stable conditions with small wind speeds.

(iii) Equation of continuity holds; the modelled pollutant is assumed to be chemically inert and no removal or deposition mechanisms are present.

(iv) Steady state conditions are assumed for the time interval for which the model is applied. These circumstances might not hold in the case of rapidly changing meteorological conditions.

(v) The boundary layer flow within the first hundred meters above the ground may not be simulated, since the statistical dispersions are assumed constant with height.

(vi) The model is not applicable for short distances from the source (of the order of hundred meters) since the plume has not reached the stability height and because the assumption of Fickian diffusion only holds for large diffusion times (when the average diffusive displacements of the pollutant particles are independent of the previous motion).

6.2 Estimation of emission rates

Good estimates of emission rates from aircraft based measurements of trace gas amounts and distributions are possible with adequate flight patterns and accurate knowledge of wind conditions. The most widely used approach for the purpose, and the one undertaken in the present work, is based on the well known divergence theorem. However, a more complex method based on the inversion of the Gaussian plume model (Equation 6.4), in its vertically integrated form, has also been used for the retrieval of emission rates for the case of several closely located sources (Krings et al, 2011).

Integral of a divergence field

The continuity equation in its integral form states that, under steady-state flow conditions, any net divergence of a vector field over a closed volume is associated with the existence of sources or sinks inside the volume. Indeed, the volume integral of the divergence of the vector field quantifies the strength of the sources (or sinks if the net divergence is negative) inside the volume. This concept can be effectively applied to the estimation of source emission rates (Q) from measured concentrations of pollutants (c) that are being advected by a constant wind (u). If an appropriate volume V enclosing the source is chosen:

$$Q = \iiint_V div(\vec{u} \cdot c) dV \tag{6.8}$$

A more intuitive and applicable form of the continuity equation is found by making use of the Gaussian divergence theorem:

$$Q = \iiint_V div(c\vec{u})dV = \iint_S (c\vec{u}) \cdot d\vec{S} \tag{6.9}$$

That is, the net pollutant flux through the surface equals the source emission rate. And those boundaries parallel to wind direction can be omitted from the calculation.

In aircraft based measurements, the flight transects over the exhaust plume are ideally performed perpendicular to the wind direction axis. Because from iDOAS measurements gas vertical column amounts are retrieved instead of concentrations, Equation 6.9 has to be modified using a height independent wind vector and the 2D-integral can be reduced to a line integral along a perimeter *L*. In addition, the formula has to be approximated in its discrete form, due to the discrete nature of the measurements:

$$Q \cong \int_L VC \cdot \vec{u} \cdot d\vec{l} \approx \sum_i VC_i \cdot \vec{u} \cdot d\vec{l}_i \tag{6.10}$$

As pointed out before, the assumption of a height independent wind field might be reasonably questionable due to surface friction (Ekman spiral). Despite the limitation imposed by the retrieval of vertically integrated gas amounts, if wind data for several altitudes is available, a reasonable approach is to use a weighted average of the wind field over the height of the plume, the weighting factors being the relative fractions of pollutant present at each layer. The estimation of the weighting factors may be done assuming a Gaussian plume model (Equation 6.4). In analogy with the horizontally integrated form of Equation 6.4, the shape of the vertical profile of the pollutant at a distance x from the source can be modeled through:

$$C(x,z) = \frac{1}{\sqrt{2\pi}\sigma_z(x)}\left[\exp\left(-\frac{(z-h)^2}{2\sigma_z(x)^2}\right) + \exp\left(-\frac{(z+h)^2}{2\sigma_z(x)^2}\right)\right] \tag{6.11}$$

Equation 6.11 allows the calculation of an adequate effective wind speed for its use in the estimation of emission rates. It must be kept in mind, though, that the application of such an effective wind speed is limited by the same assumptions as the Gaussian plume model described in the previous section.

Part III:

APPLICATION

Contents

7. Flight over a power plant

The information compiled in previous chapters, especially in Part II, is now to be applied to the main purpose of the present work: the assessment of the performance of the new airborne iDOAS instrument in the characterization of an anthropogenic point source of NO_2.

As mentioned before, the application case chosen in this respect is a flight, performed in June 2011, over the exhaust plume of a power plant, being a large and well defined tropospheric point source of NO_2.

A preliminary analysis of the data for the selected flight yielded satisfactory results with respect to the monitoring of the NO_2 emission plume (Schönhardt et al, 2011). Here, an extended study of the data is presented, more specifically addressed to the investigation of the instrument performance, possible error sources and comparison with theoretical expectations. Such analysis is completed in the last chapter with an estimation of the NO_2 emission rates from the power plant, the quantification of source strengths being one of the main final objectives of iDOAS applications.

7.1 Flight and Target description

The Ibbenbüren power station is a black coal (anthracite) burning plant, property of RWE Power AG. The facility is located in the city of Ibbenbüren, in the Münster region, Germany (52°17′9″ N, 7°44′45″ E), see Figure 7.1. The system is equipped with a chimney of 275m height and generates a power of 848MW.

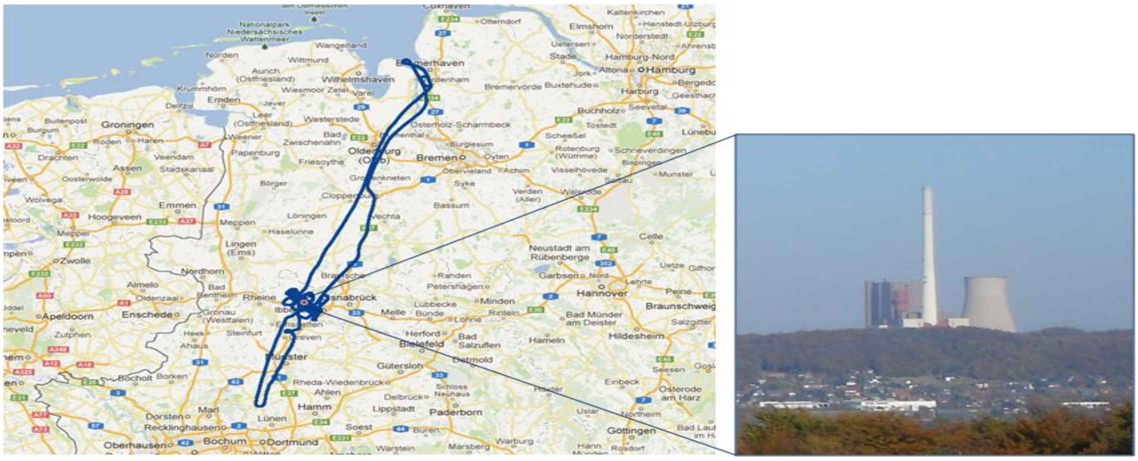

Figure 7.1: Flight track on the 04.06.2011, overlaid in Google Maps (left), and picture of the power plant in Ibbenbüren, Germany (right). (Source: City-panorama of Ibbenbüren, 2005, by Stefan Brueggemann)

Figure 7.2 shows a bar plot of the reported NO_x annual emissions from Ibbenbüren combustion station (from the European Pollutant Release and Transport Register, E-PRTR). Although the record only spans the last 4 years, the annual amount of NO_x released to the atmosphere by the

Ibbenbüren power plant operation ranges from 2000 to more than 3000 tons. These emissions make up close to a 0.9% of the total reported industrial atmospheric discharge of NO_x in Germany, which is, in turn, about 330 thousand tons.

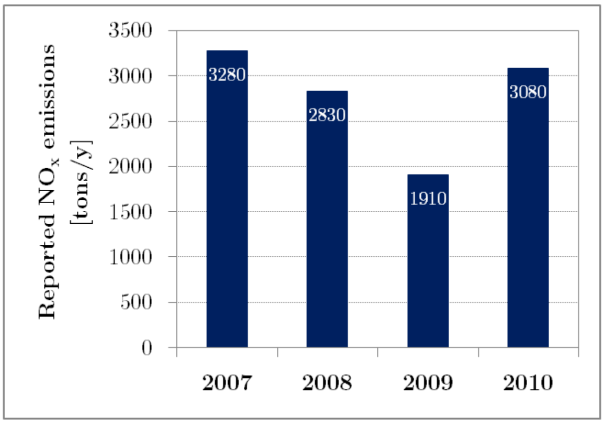

Figure 7.2: Bar plot of reported annual NO_x emissions (in terms of NO_2 molecular mass) from Ibbenbüren power station (Data source: European Pollutant Release and Transport Register, E-PRTR; http://prtr.ec.europa.eu/).

The flight on the 4th of June (2011) departed from Bremerhaven, following a southeast trajectory towards Ibbenbüren and covering in great part the course traced by the A29 and A1 highways. It was a dry and cloud free morning. The flight track over the Ibbenbüren power plant consisted of several overpasses above the exhaust plume, performed, as far as possible, perpendicular to the wind direction. The flight duration was close to 3 hours; the time period from 9 UT to 10.35 UT roughly corresponding to the plume overpasses. As depicted in Figure 7.3 (left), the typical flight altitude varied only slightly around 1100 m.a.s.l, being practically constant in the overpasses. Analogously, flight speed was kept approximately constant between 60 m/s and 80 m/s.

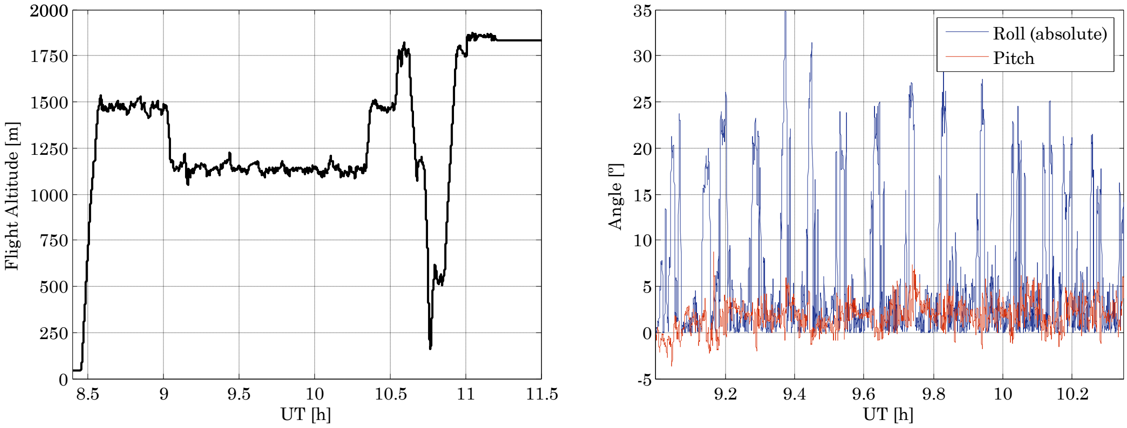

Figure 7.3: Time records for flight altitude a.s.l. (whole flight, left) and pitch and absolute roll angles (for time interval corresponding to plume overpasses, right) as measured for the flight on the 04.06.2011 over Ibbenbüren Power Station.

iDOAS measurements were taken continuously throughout the flight duration with no gaps between subsequent exposures, the constant exposure time being 0.5s. Geolocation information, positioning angles and meteorological data were also recorded by means of the GPS sensor and the AIMMS-20 system routinely installed on the Polar-5 aircraft. Figure 7.3 shows the time record for the flight altitude (left), pitch and absolute roll angle values (right), with a temporal resolution equal to the exposure time.

7.2 Geolocation correction

The computation of the geolocation of ground imaged pixels, taking pitch and roll aircraft motions into account, as described in Section 5.1, has been applied in each of the measurements taken during the flight over the power station in Ibbenbüren. The calculation has been done both for the cases of 35 and 9 viewing directions. The accuracy of the ground pixel geolocation and the good imaging quality of the iDOAS instrument have been verified by overlying the corrected ground swath on a Google Earth map (Figure 7.4).

In the pictures displayed, each ground pixel appears color-coded as a function of the intensity reaching the equivalent pixel in the detector (in counts per second). The ground swath corresponding to a single measurement is divided into 35 pixels (one per LOS). This is most appropriate in this case since, having a better spatial resolution than in the case of 9 VD, it is possible to identify ground features of smaller scale. The use of intensity as reference is very useful at this respect, because ground features appear outlined depending on their reflective characteristics.

The heterogeneity of ground reflectivity in the blue part of the visible spectrum is noticeable in Figure 7.4(a), where the ground projected swath of the instrument is displayed for the overpasses above Ibbenbüren power plant.

It is especially interesting to have a more specific look at the imaging of the roads and highways, which exhibit large reflectance and appear dark colored in the pictures.

Figure 7.4(b) shows a transect of the flight track when following the A29 highway coming from the North, and demonstrates the accurate mapping of the ground projected pixels, which correctly follow and reproduce the road path and fork, when highway A29 merges into highway A1. In addition, the shape of several croplands is agreeably reproduced, especially for those with large surface reflectivity. This is the case, e.g. for the large triangular arable land marked with an arrow in the top part of the picture.

Figure 7.4(c) displays again the good mapping of a second southern transect of highway A1, this time for the case of a sharp bend in the trajectory of the aircraft. This last situation is particularly challenging due to the large pitch and roll movements of the airplane (this map corresponds to a zooming in of the southernmost loop in Figure 7.4(a)).

Indeed, Figure 7.4(c) shows an additional very remarkable ground feature: the Sonnenhügelsee Lake (indicated in blue characters and circled in the right hand map). Water surfaces exhibit a low value of ground spectral reflectance, as demonstrated by the small intensity received from the lake surface (bluish color coding). The Sonnenhügelsee is located in the bulk of the curve, where pitch and roll angles are expected to be largest, and still it appears very well imaged in shape and correctly geolocated due to the fine spatial resolution of the imaging instrument and to the accuracy of the applied geolocation correction.

Therefore, the pixel geolocation correction is working very accurately and the apparent good spatial resolution foresees the appropriateness of the iDOAS instrument for the study of point sources of air pollution. However, it is also important to quantify more exactly the spatial resolution, the importance of taking into account aircraft motions for the geolocation of ground pixels and the effect of the approximations used in the computation of the last.

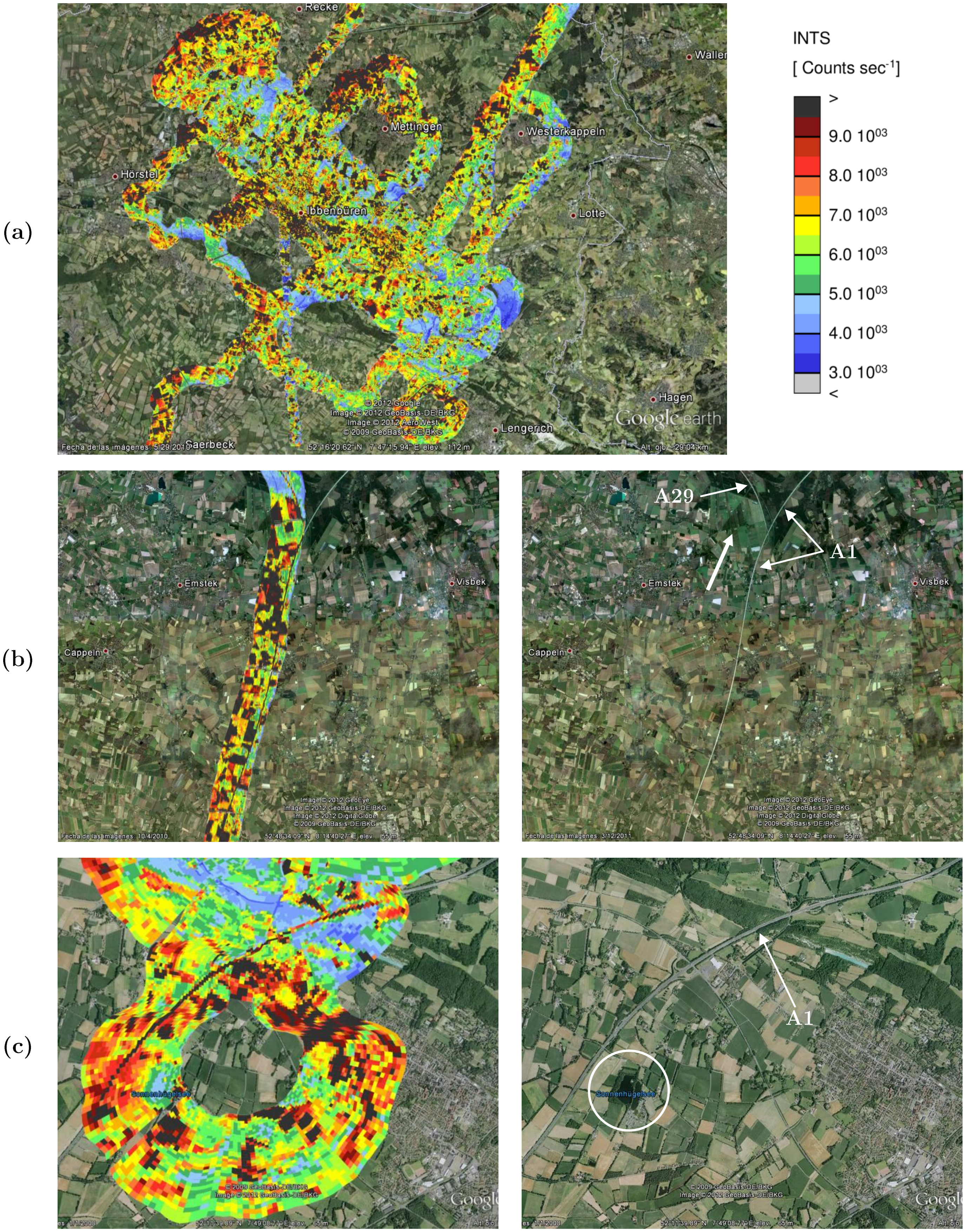

Figure 7.4: Verification of geolocation accuracy and instrumental imaging quality; Google Earth landscapes with and without intensity images of the instrument ground swath: (a) along the overpasses above Ibbenbüren power plant; (b) while overflying highway A1; (c) along a sharp curve.

Effect of pitch and roll motions

The quantity used to estimate the effect of pitch and roll movements of the airplane upon the geolocation of the ground imaged pixels is the displacement of the centre of such a pixel with respect to its position if the motions were not considered. This quantity also gives an idea of the magnitude of the relative change in the respective LOS angle.

In Figure 7.5, the flight track in comparison to the ground viewed area is plotted; on behalf of clarity, only the three central pixels (out of a total of 9 viewing directions) are displayed and appear color-coded as a function of the roll angle. Negative roll angles (bluish) are indicative of curves to the left, whereas for positive roll angles (reddish) the aircraft is turning to the right.

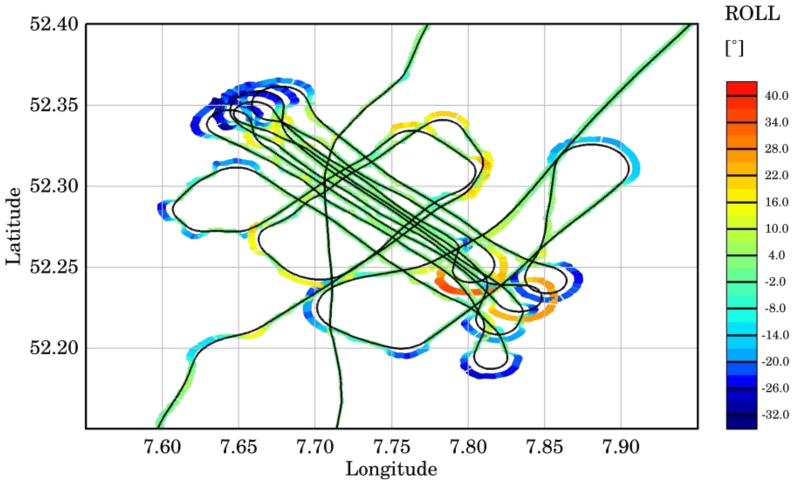

Figure 7.5: Flight track (black line) and ground imaged area (only the 3 central pixels) with color-coded roll angle values for the flight on 04.06.2011 over Ibbenbüren power station.

It can be observed how the center of the imaged swath diverges from the point immediately below the aircraft (the flight track, in black) for large absolute values of the roll angle, as well as how both coincide for null roll motions; a clear example is the red curve located among the overpasses and the straight overpasses themselves. The behavior of the swath at the turnings appears reasonable, describing shaky paths at the beginning and especially at the end of pronounced curves, characteristic of the variability of the roll angle in these situations when the pilot is trying to stabilize the airplane. As an additional point, it is also possible to infer the flight direction from the picture by considering the track and the mathematical sign of the roll.

The magnitude of the pixel centre displacement depends on the magnitude of pitch and roll motions as well as on the flight height.

Table 7.1 displays characteristic values of pixel centre displacements calculated for three different LOS: the central pixel and the two extreme pixels (rightmost and leftmost with respect to flight direction).

As seen, average displacements lie around 150m, reaching several hundreds of meters in the curves. These pixel displacements within the turns can go beyond 1000m in the case of the extreme LOS, which are more strongly affected by pitch and roll motions than the central pixel. However, even along the approximately straight overpasses, the representative pixel centre displacement hovers around 60m, due to small aircraft instabilities that translate in absolute roll angles typically smaller than 5º.

Consequently, consideration of pitch and roll angles for the location of the imaged ground projected pixels may be of great relevance, meaning that neglecting their effect may result in geolocation inaccuracies at least of the order of half the transversal size of a pixel and considerably more in curves.

LOS Number	**Displacements of the center of the pixel [m]**				
	Avg. Absolute	Avg. Straight $\lvert\text{Roll}\rvert < 5^{\text{o}}$	Avg. Turns $\lvert\text{Roll}\rvert > 5^{\text{o}}$	Max. Turns ($\lvert\text{Roll}\rvert > 5^{\text{o}}$)	Min. Turns ($\lvert\text{Roll}\rvert > 5^{\text{o}}$)
1 (Rightmost)	177	63	401	1161	95
5 (Center)	150	60	330	773	83
9 (Leftmost)	169	65	376	1234	92

Table 7.1: Displacements of the center of the pixel due to the effect of pitch and roll angles (relative to the position of the individual centre without considering these aircraft motions), for the flight on 04.06.2011, over Ibbenbüren power plant. Shown are the characteristic values for central, rightmost and leftmost LOS, throughout the overpasses above the exhaust plume.

7.3 Spatial resolution

As explained in Section 5.1, the shape and dimensions of ground imaged pixels varies depending on the LOS considered and also on the measurement considered, even for a fixed LOS. This is because values of pitch and roll angles vary along the trajectory of the aircraft. Indeed, since these angles are considered to vary (linearly) within a measurement, the shape of the pixels is not necessarily rectangular.

Hence, estimations of the spatial resolution have been quantified through the pixel dimension approximately along the flight direction (spatial resolution along track) and the perpendicular pixel size dimension (spatial resolution across track). Both distances are being computed along the intersection through the centre of the pixel.

The quantification of the spatial resolutions has been restricted to the flight transect corresponding to the continuous overpasses above the plume (9 UT to 10.35 UT), because the fact that altitude and speed were kept practically constant at 1100m and 60m/s approximately, allows to effectively appreciate the effect of pitch and roll angles in the pixel size. The results for the pixels corresponding to the extreme LOS (rightmost and leftmost of the field of view), in the case of a total of 9 viewing directions, are illustrated in Figure 7.6. Average and maximum values of the spatial resolution for these two extreme pixels and for the central LOS are summarized in Table 7.2 and Table 7.3, for a splitting into 9 and 35 viewing directions, respectively. In the case of 35 viewing directions, the number 34 is taken as the leftmost one, since number 35 is actually made up of less CCD pixels, due to the fact that the corresponding optical fiber is not completely fitted within the slit.

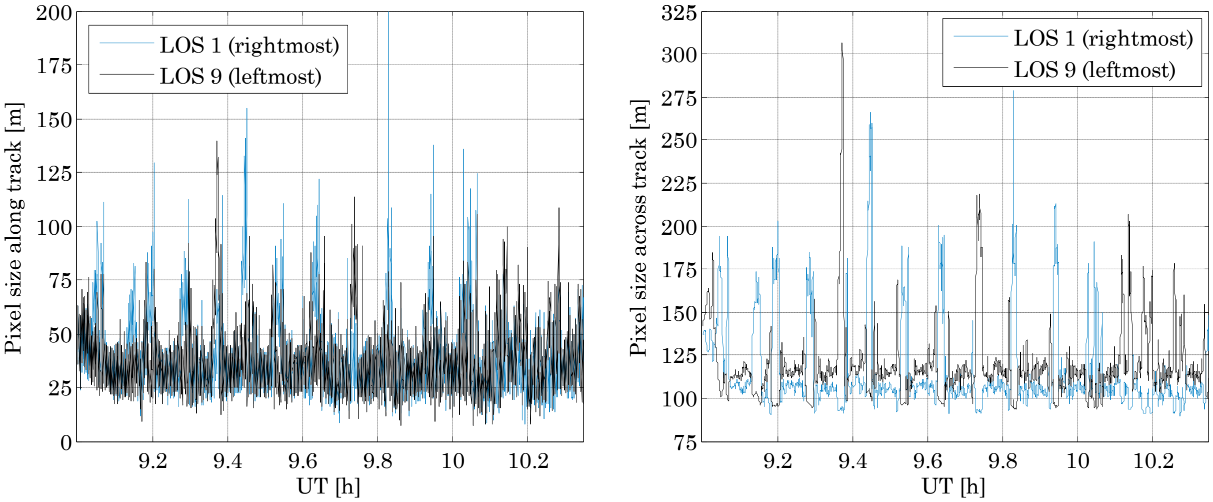

Figure 7.6: Time record of estimated spatial resolution for rightmost and leftmost LOS during plume overpasses: spatial resolution along flight direction (left) and spatial resolution across flight direction (right), as calculated for the flight on the 04.06.2011 over Ibbenbüren Power Station.

The reference to quantify a change in spatial resolution is taken to be the pixel size during the straight transects of the airplane track, when the altitude is stable and small pitch and roll motions are to be expected.

Focusing on the straight flight transects, which are of particular relevance for the characterization of the point source of air pollution, typical pixel sizes (across track x along track) round 30 x 110m for the case of 9 viewing directions, and 30 x 30 m for the case of 35.

In most of the cases, increasing absolute values of pitch and roll angles (e.g. turnings of the aircraft) tend to increase the pixel size; i.e. to decrease the across track spatial resolution. This is strictly true in the case of the central LOS, see Tables 7.2 and 7.3. However, pitch and roll motions will affect oppositely the across track resolution of pixels located at each side of the central one. Such effect is clearly seen in Figure 7.6 (right); e.g. when the aircraft turns to the right, the leftmost pixel size across track increases, whereas the size of the rightmost pixel decreases below its standard dimension (increase in across track spatial resolution).

The main parameters influencing the spatial resolution along track are the flight altitude and speed, given that the angular aperture of the FOV along flight direction has been neglected. However, given the approach undertaken to calculate the pixel geolocation, considering pitch and roll angles both at the start and at the end of a measurement, the effect of these motions upon the size of the pixel along flight track becomes relevant, see Figure 7.6 (left). The resulting change in spatial resolution in this case is not determined by the absolute values of pitch and roll angles but by their relative change during one exposure, as shown by the large variability in along track pixel size. In fact, in this case, the changes in pitch angle values are the main contributors to the variability.

LOS Number	**Pixel size along track [m]**			**Pixel size across track [m]**		
	Avg. Straight |Roll| < 5º	Max. Turns |Roll| > 5º	Avg. Turns |Roll| > 5º	Avg. Straight |Roll| < 5º	Max. Turns |Roll| > 5º	Avg. Turns |Roll| > 5º
1 (Rightmost)	34	201	51	107	279	131
5 (Center)	33	111	45	109	155	120
9 (Leftmost)	34	140	45	115	306	135

Table 7.2: Estimated spatial resolution (9VD) for the flight on 04.06.2011, over Ibbenbüren power plant. Shown are the characteristic values for central, rightmost and leftmost LOS (of a total of 9 viewing directions), throughout the overpasses above the exhaust plume.

LOS number	**Pixel size along track [m]**			**Pixel size across track [m]**		
	Avg. Straight |Roll| < 5º	Max. Turns |Roll| > 5º	Avg. Turns |Roll| > 5º	Avg. Straight |Roll| < 5º	Max. Turns |Roll| > 5º	Avg. Turns |Roll| > 5º
1 (Rightmost)	34	210	51	35	95	43
18 (Center)	33	109	45	28	41	31
34 (Leftmost)	34	143	45	34	93	37

Table 7.3: Estimated spatial resolution (35VD) for the flight on 04.06.2011, over Ibbenbüren power plant. Shown are the characteristic values for central, rightmost and leftmost LOS (of a total of 35 viewing directions), throughout the overpasses above the exhaust plume.

The ground projected pixels display a quadratic shape in the case of 35 viewing directions and a rectangular size in the case of 9 viewing directions, the latter becoming approximately quadratic when applying averaging over 2 second measurements. The sizes of the pixels as estimated make iDOAS very suitable for the mapping of anthropogenic sources.

Overestimation of spatial resolution along track

In the computation of the area viewed on the ground by the iDOAS instrument, the angular aperture of the entrance optics in the direction parallel to the flight direction (~3º) has been neglected so far. With the aim of getting an idea of the magnitude of the overestimation in the spatial resolution that this approximation implies, the total area (A_{total}) that is actually imaged in each measurement, at least during some part of the exposure time, has been approximated. The estimated A_{total}, then, has been compared to the area scanned (A_{scan}) by the central line of the FOV due to the motion of the airplane during the time the measurement lasts.

This last area is very close in value to the one that was computed in the previous section, and A_{total} is approximately (A_{scan}+iFOV). A flight speed (v) of 60m/s and an exposure time (Δt) of 0.5s have been used for the calculations. The values of the ratio [iFOV/(A_{scan}+iFOV)] are given by percentage in Figure 7.8 (left); the higher the percentage, the bigger A_{total} is compared to A_{scan}. The flight altitude has also been plotted in order to show its main influence in the enlargement of the area neglected (note that this area is the same as the iFOV). The spikes in the overestimation curve that do not have analogues in the height plot are due to the effect of roll motions and indicators of the turnings of the aircraft. Focusing on the stretch corresponding to the overpasses above the plume, the central part of the graph, it has been found that the area neglected in the calculation of the pixel geolocation may actually be 60 to 80% of the total one, which implies not only comparably large overestimation in the spatial resolution along flight, but also that the areas viewed on the ground (A_{total}) are overlapped between measurements. The overlapping takes place every time the area excluded (iFOV) is bigger than the area considered (A_{scan}), which is throughout all the flight, takeoff and landing excluded.

There is another important point to take into account: because the iFOV is moving with the aircraft, not all parts of A_{total} are imaged during the same duration within a single measurement. The beginning and end of A_{total} are only seen for a tiny instant and are therefore much less important for the measurement. This concept is illustrated in Figure 7.7, simplified for rectangular ground pixels. It shows a sketch of the areas on top of a diagram of the distances along track versus the time that each of them is viewed, for two cases of different relative size between the iFOV and the distance overflown. The use of rectangular pixels makes it possible to refer to distances along flight direction instead of areas. As displayed, there will be an area that lies inside the FOV for the whole duration of the measurement only if the iFOV along track (defined here as $2l_T$) is at least the same size as the distance $v\Delta t$ overflown during the exposure (i.e. $2l_T > A_{scan}$). In any case, there is always some part of the total area that is observed for longer time than others. This most viewed area (A_{mv}) is given by the absolute value of the difference between the iFOV and A_{scan} (i.e. $|2l_T - v\Delta t|$ along track for rectangular areas in Figure 7.7). Naturally, this difference is positive itself if there is overlapping between subsequent measurements and negative otherwise.

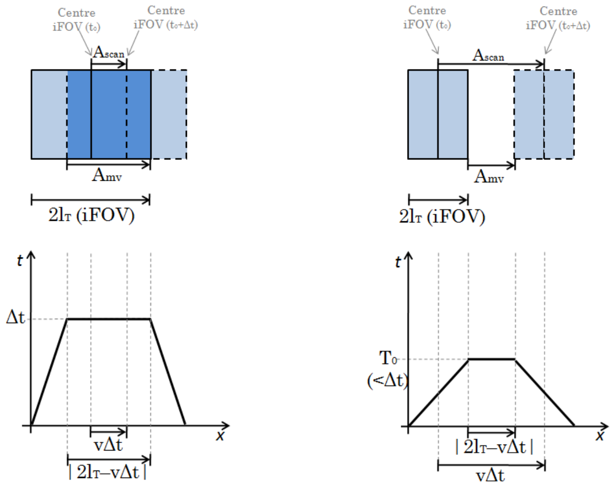

Figure 7.7: Graphs of the time during which the different parts of A_{total} lie inside the FOV (Δt, the exposure time) with respect to flight direction: case $v\Delta t<2l_T$, i.e. for large iFOV and comparably short exposure time or low flight speeds (left); and case $v\Delta t>2l_T$ (right). The overlapped area is shaded in dark.

Therefore, it can be considered that the area that contributes most to the measurement is that which is viewed for the longest time; the overestimation in the spatial resolution along flight direction is to be estimated again, now as a comparison between the most viewed area and the scanned area ($1-A_{scan}/A_{mv}$) (Figure 7.8 (right)). In this case, for the stretch corresponding to the overpasses above the plume, A_{scan} is 80-90% of A_{mv}, i.e. the overestimation lies around 10-20% (for the central flight pattern). Large increases in the overestimation are found only for pronounced curves, as the roll angle greatly influences the magnitude of the most viewed area.

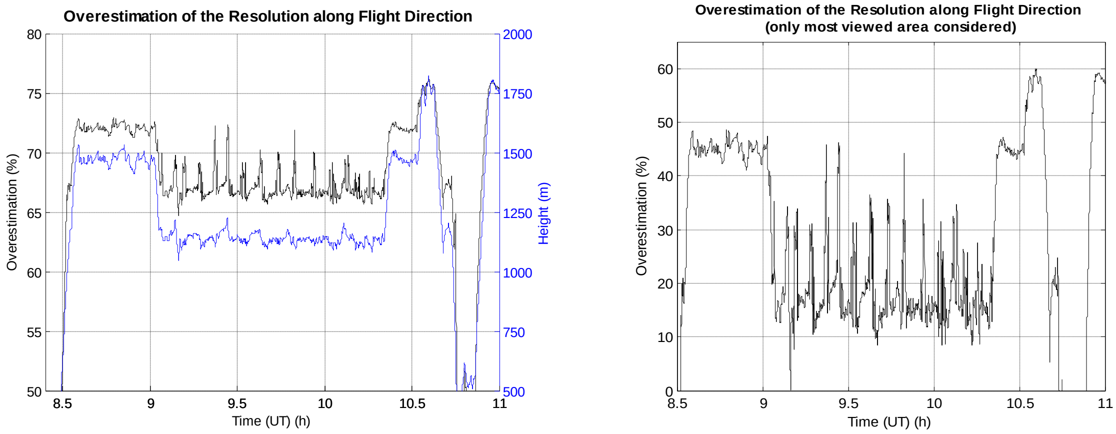

Figure 7.8: Overestimation of the spatial resolution for the flight on 04.06.2011; comparison between the calculated ground viewed area (with length vΔt along track) and the area when taking into account the influence of the iFOV if: the total area is considered (left) and only considering the most viewed area (right).

A_{scan}, as calculated in the previous section, can differ greatly from A_{total}, although it is relatively close to A_{mv}. If the results of the NO_2 retrieval were applied to A_{total}, overlapping between measurements would take place. If the values of the inferred NO_2 slant columns were averaged for these overlapping areas, as is the usual practice, point sources would be easier to localize and the values of the slant columns would appear smoothed, resulting in a virtual improvement in the spatial resolution. However, this procedure is counterproductive if NO_2 emission rates are to be determined from the retrieval, as the values of the differential slant columns would be diluted through the averaging. This would decrease the accuracy of the results due to taking into account regions which are only viewed for a comparably short part of the exposure time. Effectively, this might lead to an underestimation of NO_2 amounts directly above the source. However, the usage of A_{scan} makes a good compromise and is actually closer to A_{mv} that A_{total} actually is.

As a conclusion, the pixel geolocation correction has proved successful under the assumptions undertaken, as shown by the accurate imaging of ground features (Section 7.1) and supported by the relatively small error estimated in the overestimation of spatial resolution. However, it must be considered that the approximation undertaken might not hold in the case of different flight characteristics, for example for different flight altitude and speed combinations.

8. Retrieval of NO_2 Columns

The central step in DOAS applications is the retrieval of the column amounts of the target trace gas. As described in Section 5.2, an adequate DOAS slant column retrieval requires the appropriate selection of a series of parameters in the initialization of the inversion algorithm. For the real application of the flight over the exhaust plume of Ibbenbüren power plant, the choice of optimal inversion conditions were performed by the analysis of the retrieval quality when changing several of these parameters.

Once the optimal retrieval parameters were determined, vertical column amounts were derived from the output slant columns. This was effected through suitable calculation of the corresponding AMF by means of SCIATRAN radiative transfer model, as explained in Section 5.4. Again, several assumptions had to be made, this time regarding the atmospheric state and ground spectral reflectance conditions.

In the ensuing sections, the steps followed in the optimization of retrieval parameters and calculation of AMF are described, and the subsequent results for the NO_2 amounts along the flight transect over Ibbenbüren power station are presented and discussed.

8.1 Optimization of retrieval parameters

In order to find the optimal parameters for the slant column retrieval, repeated DOAS inversions were applied to the data, varying in each situation the parameter of interest. In all cases, though, a quadratic polynomial for modelling broadband spectral features and a constant stray light offset were selected. To reduce computational time, the following tests were only applied to the dataset for the central viewing direction, out of a total of 9, and only for measurements within the overpasses above the power station.

The magnitude of the RMS of the residual spectrum was used as primary indicator of the quality of the fit, since it is desirable to have the smallest possible mismatch between measurements and fitted model. As a second indicator, the RMS of each measurement (RMS^i) was normalized (RMS_n) with respect to shot noise as expected from the measured number of electrons per binned pixel and per measurement (I^i_{meas}):

$$RMS_n^i = \frac{RMS^i}{\sqrt{I^i_{meas}}} \tag{8.1}$$

Since the RMS is approximately the inverse of the actual SNR, the ideal situation would be if the residuals arose only as a result of shot noise (Section 5.3). In that case a normal distribution of the normalized RMS values with mean 1 would be expected. Hence, the expected value of the normalized RMS, calculated from a frequency histogram computed with the results for all measurements and the skewness of the estimated probability distribution were also used as indicators.

In addition, because there might be systematic phenomena affecting the accuracy of the retrieved slant columns that are not reflected in the residual spectra nor in the RMS value, additional tests were needed to discriminate between retrievals showing similar RMS records.

The starting point for the optimization routine was a standard DOAS retrieval for NO_2 (see Table 8.1), within the fitting window spanning the 425-450nm spectral range, and including O_3, O_4 and H_2O absorbers in addition to NO_2. The reference absorption cross section spectra are those measured approximately at the temperature of the atmospheric layer where the bulk of the corresponding absorber is expected to be found; close to the surface (~293K) for NO_2 and O_4 and mid stratosphere (~241K) for O_3.

The background spectrum used as reference for the DOAS model fitting (I_0), see Section 3.2 (Equation 3.5), is, in this case, a time average of consecutive spectra measured, during the same flight, over a rural scene with low atmospheric NO_2. Hence, the retrieved slant columns are actually slant column differences between the background scene and the particular measured scene. An individual background spectrum is used for the retrieval in each LOS.

Standard NO_2 Retrieval Parameters	
Fitting Window	425 – 450 nm
Differential Absorbers	NO_2 (293K) O_3 (241K) O_4 (296K) H_2O (HITRAN)
Additional effects	Ring (SCIATRAN) Constant Stray Light
Polynomial	Quadratic
Background spectrum	Low NO_2 rural scene 1 min average Individual for each LOS

Table 8.1: Parameters for the standard NO_2 retrieval; after testing several other parameter combinations, this standard was selected as the optimal one.

The standard retrieval was repeated with 2 different background spectra, both of them constructed from 1 minute averages of consecutive spectra, these being selected from different rural scenes with low atmospheric NO_2 amounts. The results were satisfactory, since no significant changes in the RMS values or in the retrieved slant columns were detectable between fittings with different backgrounds. Therefore, the background spectrum chosen was that corresponding to the smallest NO_2 pollution, which yielded slightly higher slant column differences.

A second test for the optimization of the retrieval was performed by varying the length and position of the fitting window in steps of 5nm and in as many combinations as allowed by the spectral range covered by the instrument. Table 8.2 summarizes the results obtained, regarding the principal indicators, RMS and RMS_n. Fitting windows less than 10nm wide were excluded from the test, since the information contained was expected to be too limited (the system to be inverted would be highly under-determined; an ill-posed problem). Indeed, the inversion procedure implies the retrieval of at least 9 parameters (3 coefficients of the polynomial, 4 absorber columns, the filling in factor and the stray light offset) plus the shift and squeeze coefficients for the fine tuning of the calibration. The spectral resolution (width of slit function) is approximately 0.7nm for the best case (see Section 4.1, Figure 4.2) so, overall, the independent pieces of information would be hardly more than 10.

Fitting Window [nm]	**NO_2 ref. T [K]**	**Additional variations**	**Avg. RMS**	**Std. RMS**	**Avg. RMS_n**	**Skewness RMS_n**
425-450	293	--	0.00190	0.00028	1.069	2.205
	293	H_2O excluded	0.00192	0.00029	1.075	2.055
	221	--	0.00191	0.00028	1.069	2.175
430-450	293	--	0.00186	0.00029	1.055	2.942
	293	H_2O excluded	0.00187	0.00029	1.061	3.220
	221	--	0.00186	0.00029	1.055	2.914
435-450	293	--	0.00173	0.00026	1.001	1.722
	293	H_2O excluded	0.00174	0.00025	1.008	1.682
	221	--	0.00174	0.00026	1.010	1.727
425-445	293	--	0.00193	0.00030	1.062	2.199
425-440	293	--	0.00207	0.00038	1.115	2.918
430-445	293	--	0.00190	0.00031	1.052	2.928

Table 8.2: Values of the primary fit quality indicators, RMS of the residuals and normalized RMS, for different combinations of retrieval parameters (for the set of measurements corresponding to the overpasses above Ibbenbüren power plant).

Three fitting windows stood out with the best performing RMS: 425-450nm, 430-450nm and 435-450nm (highlighted in Table 8.1). Fitting windows with similar RMS values, 425-445nm and 430-445nm, were discarded since they revealed some correlation connecting the retrieved columns of O_4 and O_3, a behavior that might be indicative of ill-posedness of the inverse problem.

Two additional tests were carried out for the three selected fitting windows (Table 8.1). First, the NO_2 absorption cross section reference spectrum was changed for one measured at rather low temperature (221K), typical for stratospheric NO_2. The NO_2 slant column values retrieved with the low temperature reference were smaller (through an approximately constant scaling factor).

This was to be expected, since due to the lesser occupation of excited energy levels in molecules at low temperatures, the probability of transition due to absorption is higher (larger absorption cross sections). However, this also means that, at low temperatures, additional absorption structures might appear. The fact that the RMS values found in the retrievals with a low temperature reference are practically the same as with a high temperature one implies that the instrument is not sensitive enough to distinguish such structures.

Secondly, the retrievals were repeated without including H_2O as absorber. A look at the water vapor column amounts retrieved previously showed that these varied quite randomly around zero. In effect, excluding H_2O from the inversion did not affect the RMS values much, indicating that water vapor amounts were below the detection limit of the instrument and verifying the dry atmospheric conditions on the day of the measurements.

The fitting window yielding the best results regarding the RMS and its noise-like behavior was the 435-450nm one. However, the use of such a narrow wavelength range proved to compromise the accuracy in the slant column retrieval for those viewing directions characterized by broader slit functions (the outer side LOS). The effect was particularly strong in the case of LOS number 35, for which the lack of information adds to the low signal to noise ratio (the corresponding optical fiber illuminates less CCD pixels; see Section 7.2). In that case, the fit yielded negative values of NO_2 slant columns for the spectra corresponding to the background scene, pointing to a systematic source of error.

The 430-450nm fitting window was also discarded, being the narrower of the remaining two and given that the skewness of the normalized RMS was larger, revealing the presence of strong outliers.

Finally, the chosen retrieval parameters were those of the standard NO_2 fit given in Table 8.1. Note that the retrieval is performed independently for each viewing direction, considering the corresponding slit function and background spectrum in each case. Figure 8.1 shows an example of a retrieval result, displaying the comparisons between reference absorption cross section spectra (solid lines), scaled with the retrieved slant column value, and the fitted differential optical density for each of the absorbers considered (dashed lines). The plots correspond to a measurement in the central viewing direction and were taken while flying just above the NO_2 plume. The NO_2 absorption features are accurately fitted and the resulting residual spectrum resembles pretty much that of pure noise.

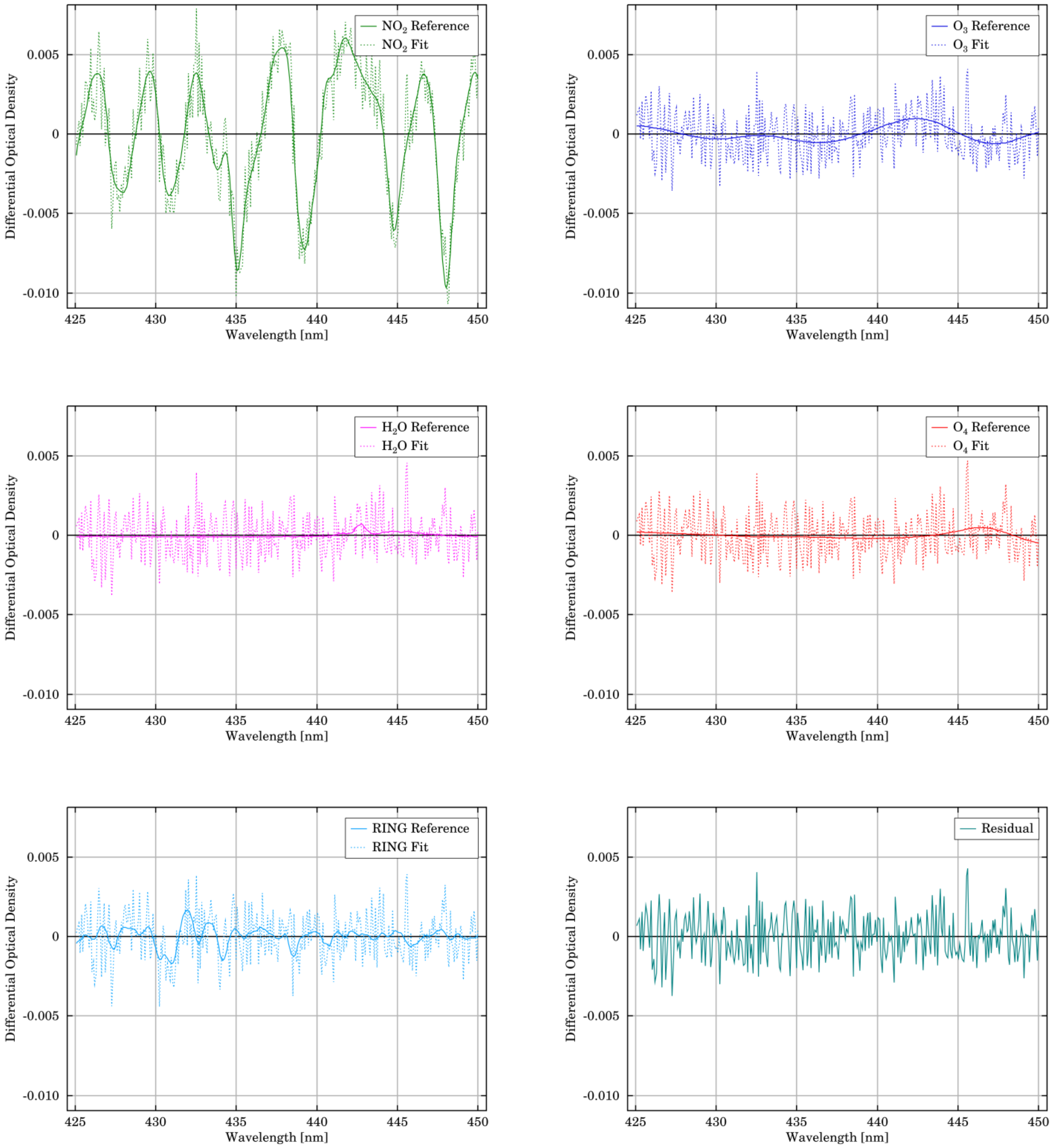

Figure 8.1: Comparisons between reference absorption cross section spectra, scaled with th3e retrieved slant column value, and the fitted differential optical density (Central LOS out of 9, measurement time: 10:11:43, SZA: 39.74º): NO$_2$ (top left), O$_3$ (top right), H$_2$O (center left), O$_4$ (center right), Ring effect (bottom left) and residual spectrum (bottom right). The NO$_2$ column retrieved was: SC(NO$_2$)=3.95x10^{16} molec/cm^2, with an error: ΔSC(NO$_2$)=2.63%.

Figure 8.2 shows the retrieved NO$_2$ slant column differences for the overpasses above the emission plume of Ibbenbüren power plant, both for a total of 9 and 35 viewing directions. As seen, the advection of the NO$_2$ plume in the direction of the wind (around 72º, as to be estimated in Section 10.2) and its evolution within distances c.a. 10km from the source have been successfully mapped. Although the SC values appear noisier for the case of 35 viewing directions (due to lower SNR), especially in the background regions, they are in concordance with those found for 9 LOS, which seem very reasonable (around 38 - 58 x10^{15} molec/cm^2 (35 LOS) and 34 - 42x10^{15} molec/cm^2 (9 LOS) in the bulk of the exhaust plume) for the upcoming vertical column computation.

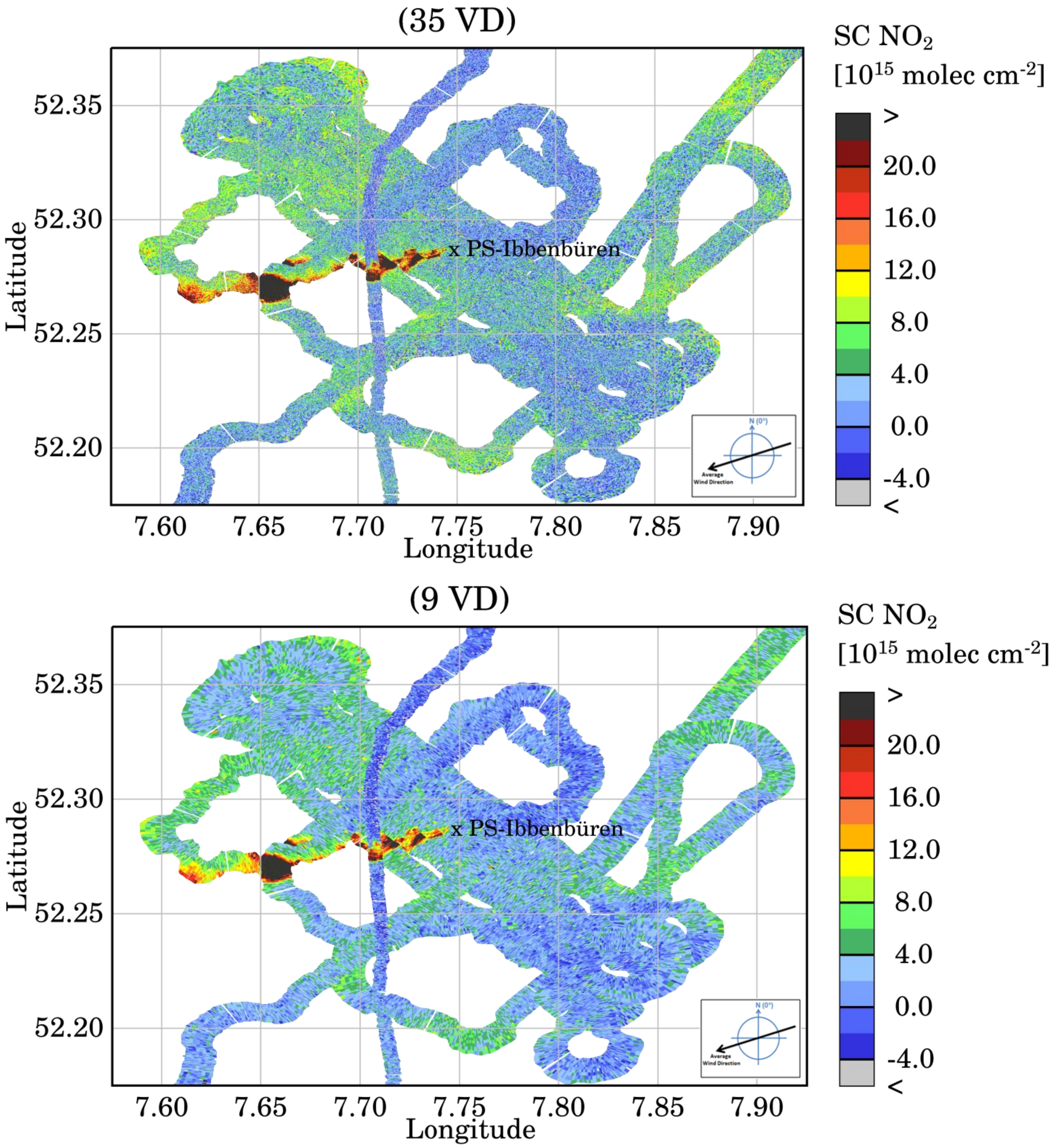

Figure 8.2: Plots of retrieved NO$_2$ slant column differences for the flight on 04.06.2011 over Ibbenbüren power station; 35 viewing directions (top) and 9 viewing directions (average between adjacent optical fibres, bottom).

8.2 AMF and tropospheric Vertical Columns

The NO_2 amounts retrieved in the DOAS fit are Differential Slant Columns (DSC_i). That is, they are not only the concentration of NO_2 integrated along the light path, but also the difference between the SC in the background scene (SC_0) and the SC in the monitored scene (SC_i). Moreover, both of these slant columns can be separated into a stratospheric and a tropospheric contribution:

$$\begin{aligned} DSC_i &= SC_i - SC_0 = (SC_i^{strat} + SC_i^{trop}) - (SC_0^{strat} + SC_0^{trop}) = \\ &= (SC_i^{strat} - SC_0^{strat}) + (SC_i^{trop} - SC_0^{trop}) = DSC_i^{strat} + DSC_i^{trop} \end{aligned} \tag{8.2}$$

Therefore, prior to the tropospheric AMF calculation, a correction of the stratospheric signal was applied to the retrieved DSC. To do so, a constant stratospheric vertical column was considered and the stratospheric AMF was assumed to vary only due to geometrical reasons related to the change in SZA between the background and the actual measurement:

$$\begin{aligned} DSC_i^{trop} &= DSC_i - DSC_i^{strat} = DSC_i - VC^{strat}\left(AMF_i^{strat} - AMF_0^{strat}\right) = \\ &= DSC_i - VC^{strat}\left[\frac{1}{\cos(SZA_i)} - \frac{1}{\cos(SZA_0)}\right] \end{aligned} \tag{8.3}$$

The value taken for the constant NO_2 stratospheric VC was 4.3x10^{15} molec/cm^2 (Andreas Richter, personal communication); the stratospheric column as retrieved at 53°N and 8°E from SCIAMACHY measurements on the same day, 4th of June 2011, at the overpass time of the satellite, 10 UT. The assumption of a constant VC is quite reasonable, regarding that diurnal NO_2 stratospheric VC increasing rates have been estimated to be close to 1.0x10^{14} molec/cm^2/h (Sussmann et al, 2005). This implies an error of 5% in the stratospheric VC. However, because the stratospheric AMF also depends on the corresponding VC, the maximum error in the stratospheric correction factor is close to 13% (for a two hour difference between the current measurement and the background measurement). However, for the overpasses just above the plume this time difference is smaller (~40 min maximum) and the error introduced is below 2%.

Once the stratospheric signal was subtracted, the tropospheric Vertical Column Differences (DVC_i) were computed through the corresponding DSC and tropospheric AMF (see Section 3.3):

$$DVC_i^{trop} = \frac{SC_i^{trop}}{AMF_i^{trop}} - \frac{SC_0^{trop}}{AMF_0^{trop}} \approx \frac{DSC_i}{AMF_i^{trop}} \tag{8.4}$$

The approximation undertaken in the last step of Equation 8.4 implies that the AMF for the background is equal to the AMF for the current measurement. The requirement of such an approximation arises from the need of assuming a NO_2 profile in the background scene for the corresponding AMF calculation. Such profile is largely unknown since several profile shapes are possible and reasonable, but actually the changes in AMF between the background and current measurement are no overly important, provided that the NO_2 amount in the background is small.

The tropospheric AMF needed in Equation 8.4 for the calculation of NO_2 VCD was performed by means of the SCIATRAN radiative transfer model (Section 5.4). The conditions assumed for initialization of the model, some of which have been varied to investigate their impact, are listed below:

- **Radiation wavelength:** constant at 440nm. The wavelength dependence of the AMF within the fitting window is small and not considered.
- **Flight altitude:** the instrument is located at a constant height of 1km. This is similar to a 1.1km flight altitude above 100m high terrain.
- **NO_2 profile:** constant NO_2 mixing ratio (1ppb) in the lowest kilometer of the atmosphere, linearly decreasing mixing ratios up to 2km and zero thereon.
- **Surface:** Lambertian reflector (diffuse). This implies that the azimuthal dependence is neglected.
- **Ground reflectance:** constant with a value of 0.05.
- **Aerosols and clouds:** not considered.

The tropospheric AMF for NO_2 under the conditions described above were computed for a large range of SZAs and for a constant LOS of the instrument of 0º (AMF_i^0). The appropriate AMF, then, was applied to each measured SCD depending on the corresponding SZA. The correction to account for the change in LOS (due to the different viewing directions available in iDOAS measurements and to the pitch and roll effects) was applied considering only geometrical effects:

$$AMF_i^j = AMF_i^0 \cdot \frac{\sec(SZA_i) + \sec(LOS_i^j)}{\sec(SZA_i) + 1} \tag{8.5}$$

The term LOS_i^j appearing in Equation 8.5 refers to the viewing angle of the viewing direction j in the measurement i at SZA_i.

Figure 8.3 shows the retrieved NO_2 VCD for the overpasses above the emission plume of Ibbenbüren power plant, both for a total of 9 and 35 viewing directions. The NO_2 column amounts found in the bulk of the exhaust plume range from 19 - 25x10^{15} molec/cm^2 in the case of 35 LOS, and from 14 - 18x10^{15} molec/cm^2 for a total of 9 LOS. Similar values are found in the literature for analogous iDOAS applications but for other power plants (Heue et al, 2008). The dilution of the column amounts by averaging is clearly seen for the case of a total of 9 viewing directions. However and as pointed out before this last approach has the advantage of a higher SNR.

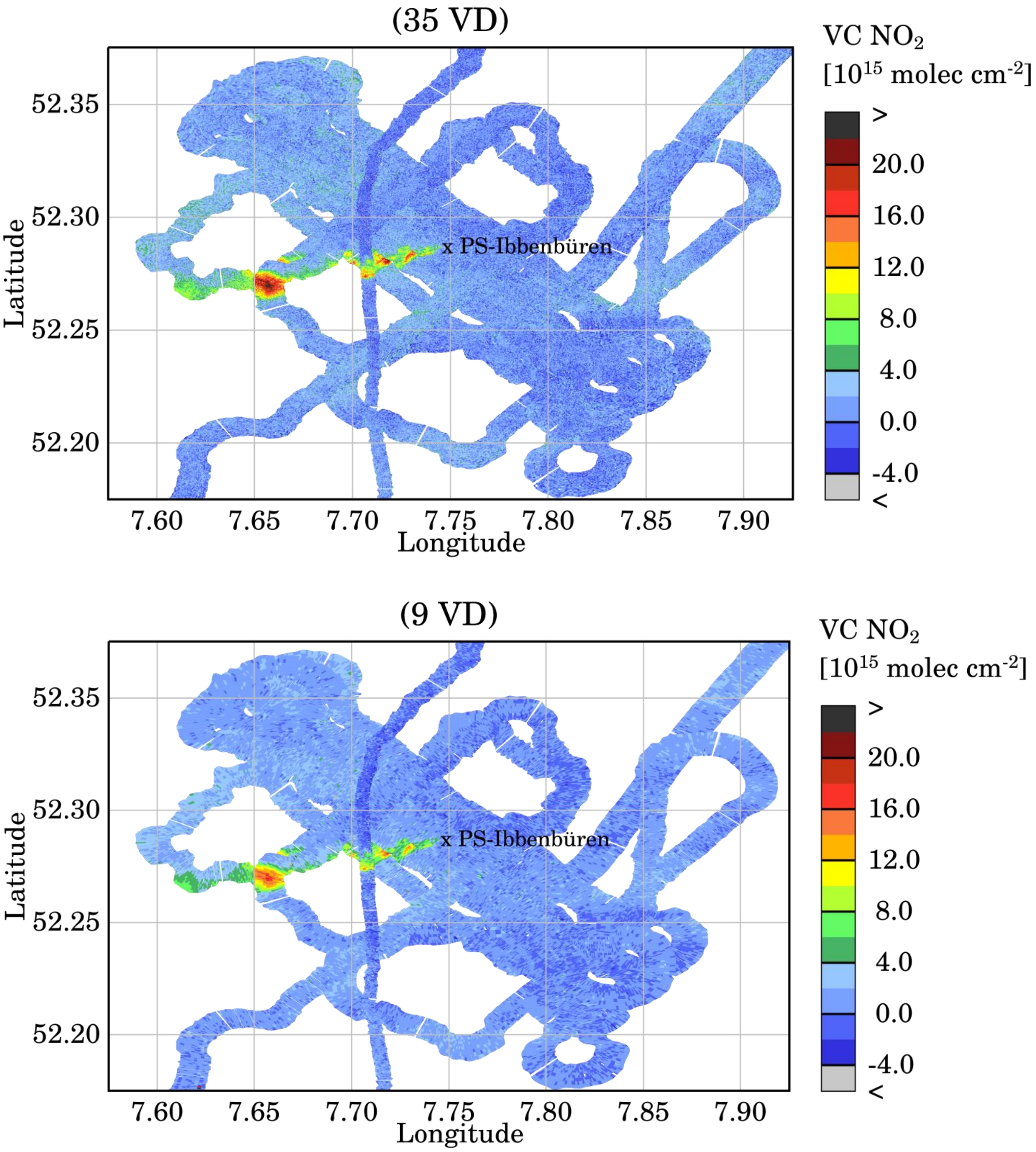

Figure 8.3: Plots of retrieved NO_2 vertical column differences for the flight on 04.06.2011 over Ibbenbüren power station; 35 viewing directions (top) and 9 viewing directions (average between adjacent optical fibres, bottom).

Sensitivity study

In order to test the validity range and the error introduced by the parameter choice in the AMF calculation, a standard sensitivity assessment was performed by running SCIATRAN radiative transfer model for different combinations of several critical parameters such as NO_2 vertical profile, surface reflectance and LOS.

Vertical profiles of BAMF (see Section 3.3 for reference) are helpful to study the sensitivity of the experimental setup, given certain environmental conditions, to the absorber amount present at different altitudes.

Figure 8.4 displays such profiles for a fixed SZA of 40° and varying ground albedo conditions. As a general characteristic, the sensitivity is maximal with respect to the NO_2 column located directly below the flight altitude, and decreases almost linearly for absorber amounts at lower atmospheric heights. The signal reaching the detection system from the NO_2 located at heights above the aircraft altitude is weaker, which is to be expected given the experimental setup choice. Altitude layers below the aircraft are traversed twice, on slant paths both times, in comparison to layers above where they only travel through once. The existence of a sensitivity maximum below the instrument height might be roughly explained by the fact that although fewer photons from direct sunlight input make it to the lower layers in the atmosphere, also the scattering efficiency increases for lower altitudes due to the increasing air density. The effect of changing ground albedo is most noticed for absorber amounts at decreasing heights, especially in the first hundred meters above the surface, which become increasingly relevant for higher surface reflectivity values. Indeed, for very high albedo values, the sensitivity of the observation method towards the lowermost atmospheric layer drastically increases close to the surface.

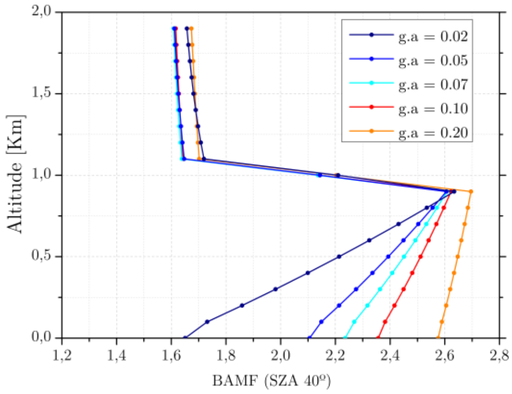

Figure 8.4: Vertical profiles of the BAMF for different ground albedo conditions.

The BAMF profiles also contain information on the influence of the initial NO_2 profile choice upon the calculation of the AMF. The AMF can be regarded as an average of the BAMF weighted by the NO_2 vertical profile. Because the NO_2 amount, being a weak absorber, does not affect the light path much (and hence neither the BAMF), the resultant AMF for any possible profile will be a value between the minimum and maximum BAMF. This gives an estimation of the maximum possible error introduced by a particular NO_2 profile assumption. In this respect and for the case of this study, the upper limit uncertainty in the computed AMF can be estimated to be around 30%.

In the AMF computation a constant surface reflectance of 0.05 was considered. Figure 8.5 (right) displays the dependence of the AMF on the SZA for different albedo conditions (2% to 20%). Intuitively, AMF values increase with the SZA due to the light path enhancement. The iDOAS observations over Ibbenbüren power plant lie within the SZA range from 33º to 58º approximately. Hence, the uncertainty introduced by the assumption of a constant 0.05 albedo ranges from 8 to 10% approximately, depending on the SZA and as long as the surface reflectivity lies within the range considered.

To test the reasonability of calculating the AMF for the different LOS angles through pure geometrical considerations, the radiative transfer model was repeatedly executed (assuming a constant 0.05 albedo) for LOS angles ranging from 5º to 40º. This interval comprises the LOS angles inherent to the instrument FOV plus a maximum angular contribution of ~15º from pitch and roll motions. The comparison between the AMF computed this way and the AMF estimated applying the geometrical correction for the LOS angle (Equation 8.5) is shown in Figure 8.5 (left). The error committed not considering the radiative transfer explicitly is negligible. It increases for increasing LOS angles, resulting in a maximum overestimation in the AMF of ~1% for a LOS of 40º. The geometrical approximation in the LOS correction is reasonable for the current study.

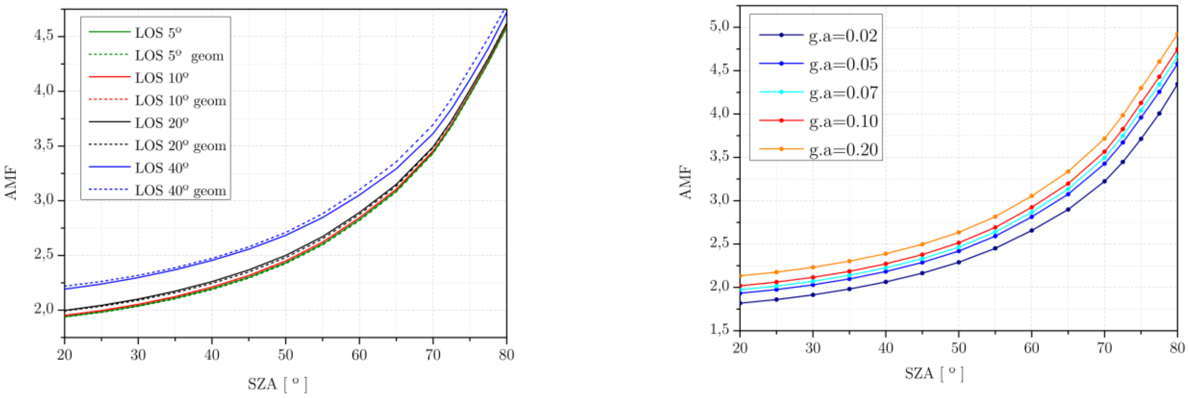

Figure 8.5: AMF dependency on SZA for different ground albedo conditions and fixed 0º LOS (right). AMF values considering a non-zero LOS angle (left); from SCIATRAN (continuous lines) and from the application of a geometrical correction for the LOS (dashed line).

9. iDOAS data quality evaluation

One of the main purposes of the present work is to investigate the performance of the iDOAS instrument in a real application situation, when actually mounted on an aircraft and subject to very variable environmental conditions. Through the example of the test flight over Ibbenbüren power plant, the especially good imaging quality of the instrument has been demonstrated (Chapter 7). Also, the selection of optimal DOAS retrieval parameters has yielded very reasonable NO_2 vertical column values in the monitoring of the power plant exhaust plume with promising fitting results regarding the RMS of the residuals and the related SNR (Chapter 8).

In the following sections a more detailed study on the nature of the resulting residual spectra is presented, which may serve to identify any systematic structure, if present, that instrumental effects might have introduced in the measured spectra (see Section 5.3). Also the light transmissivity of the instrument in real case operation is evaluated with reference to the theoretically expected radiation intensity, (see Section 4.3). Both the appearance of residual structures and the efficiency of light transmissivity have a big impact on the actual SNR which, in turn, determines the sensitivity limit for the detection of NO_2. Hence, these concepts serve to assess the quality of the data provided by the iDOAS instrument, which is crucial for an accurate and sensitive retrieval of trace gas amounts in the atmosphere.

9.1 Behavior of the RMS of residuals

A common method to identify the existence of constant systematic effects, at least those that are reflected in the residual spectrum after the retrieval, is to test the behavior of the resulting RMS of residuals when averaging several measured spectra.

As explained in Section 5.3, the RMS is a measure of the average standard deviation of the measurements with respect to the fitted model. If these deviations arise as a consequence of random phenomena such as noise effects or even quasi statistical non constant systematic contributions, the reduction of RMS in averaging should be accurately predicted by the statistical theory. Indeed, if an average between N uncorrelated spectra, each with standard deviation RMS_i, is performed, the standard deviation of the residuals in the average spectrum, $RMS <>_N$, is ideally given by:

$$RMS <>_N = \frac{1}{N}\sqrt{\sum_{i=1}^{N}(RMS_i)^2} \tag{9.1}$$

This last expression is further simplified if the individual residual spectra have all the same standard deviation (i.e. $RMS_i = RMS$):

$$RMS <>_N = \sqrt{\frac{(RMS)^2}{N}} = \frac{1}{\sqrt{N}} RMS \tag{9.2}$$

Since constant systematic sources of error are not reduced by averaging, their presence would deviate the behavior of the RMS in averaging from the ideal one given in Equation 9.2.

Therefore, to test the behavior of the RMS in the NO_2 retrievals performed for iDOAS measurements over Ibbenbüren power station, sets of 4 consecutively measured spectra were averaged and the resulting average spectrum was fitted. This is equivalent to a time average of 2 seconds, provided that the exposure time is constant at 0.5 seconds.

The assumption that the 4 measurements used for the average are independent is justified. However, it might be argued that not necessarily all the 4 RMS are the same, for the intensity reaching the detector in each case might vary. Nevertheless, the variation is expected to be small, and the use of Equation 9.2 did not show significant changes with respect to the application of the generalized Equation 9.1 in a test computation.

The mean RMS of the 4 single spectra ($<RMS>$) and the RMS of the averaged spectrum ($RMS<>$) were computed and compared in several scatter plots, to facilitate the recognition of deviations from the ideal behavior, which in this case is given by:

$$RMS <> = \frac{1}{\sqrt{4}} < RMS > = \frac{1}{2} < RMS > \tag{9.3}$$

That is, it is expected that the RMS of residuals after averaging is reduced by a factor of 2 with respect to the mean RMS of the single spectra.

Selected scatter plots are displayed in Figure 9.1: two for the case of a total of 35 viewing directions, one for the central LOS and the second for the rightmost LOS; and one plot for the central LOS in the 9 viewing direction situation.

Measurements corresponding to the takeoff and landing of the aircraft and clear RMS outliers have been excluded from the analysis. The resulting data series appears color-coded as a function of the intensity of the backscattered radiation in each case. The expected ideal behavior is represented by the black line with a slope of ½ and the linear fit of the datasets is shown by the red line. The results of the linear fitting, which are given in the plots, may serve as quantitative indicators for the deviation from the ideal behavior. For example, the R-squared coefficient measures the fraction of variance of the data that is explained by the linear fit and its square root is the correlation coefficient accounting for the linearity of the relation. The departure of the slope of the linear fit with respect to the ideal ½ gives also an intuition of how many data points and how strongly they deviate from the ideal behavior.

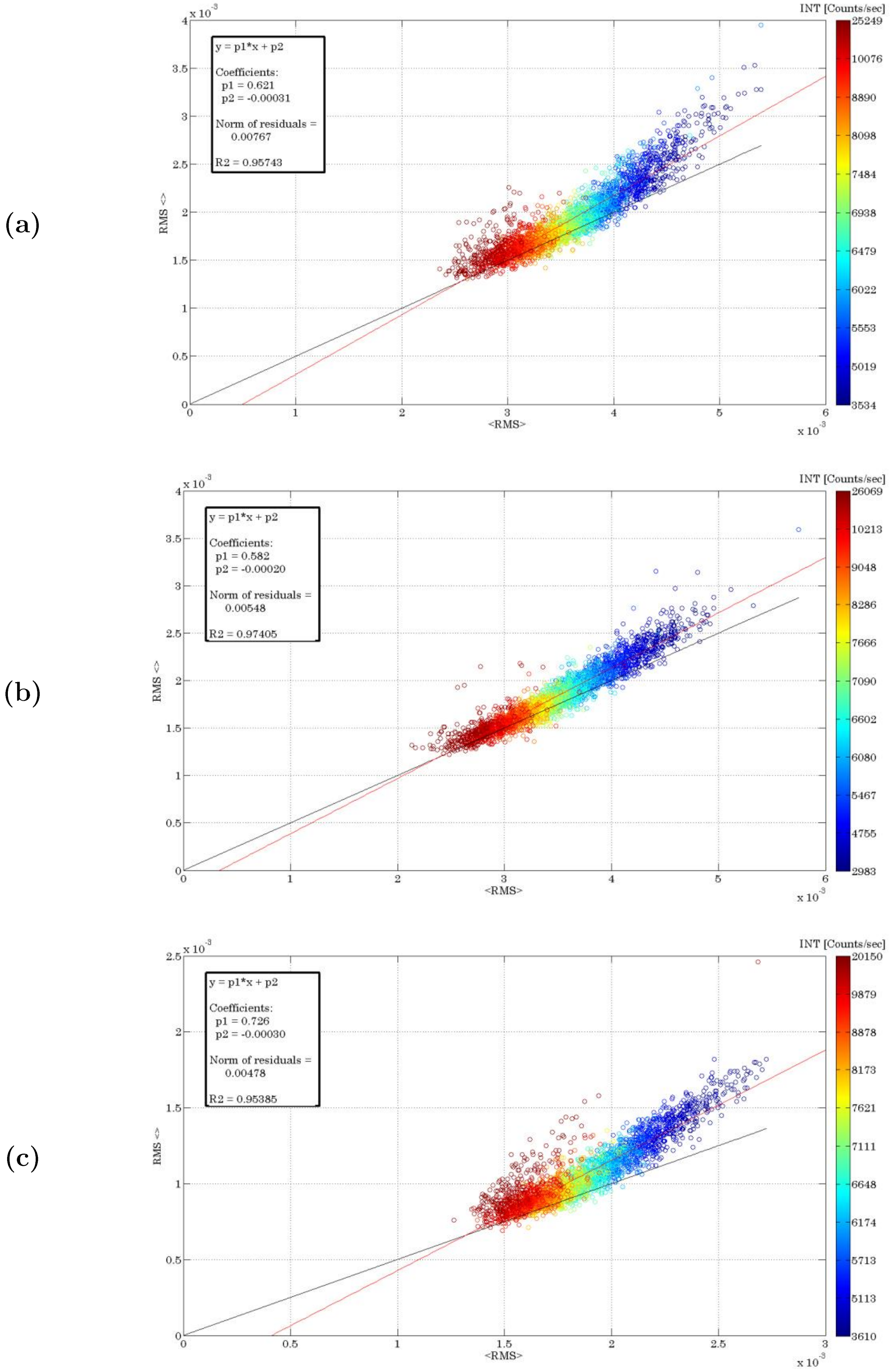

Figure 9.1: Investigation of the RMS behavior in averaging; scatter plots of the RMS of residuals for the averaged spectrum (RMS<>) vs. the mean RMS of the four spectra used in the averaging (<RMS>). Datasets correspond to the series of iDOAS measurements, performed on 04.06.2011 over Ibbenbüren power plant, for: (a) central LOS of a total of 35 viewing directions, (b) rightmost LOS of a total of 35 and (c) central LOS of a total of 9.

For the situation of a total of 35 viewing directions, for the central LOS (Figure 9.1(a)), it can be seen how for measurements with mid to high intensity of backscattered radiation, the behavior of the RMS fits reasonably well the ideal black line. The linear fit shows a behavior with a slope of 0.62 and a R^2 of 0.96. Hence, we can infer that there is not any large constant systematic effect affecting the data.

Still, there is a small but clear deviation from the statistical behavior towards those measurements for with low intensity. Lower intensities correspond to higher RMS, as can be suspected from the rainbow-like color structure of the datasets and as will be shown below. Therefore, the deviation from the ideal performance is enhanced with decreasing intensities. The hypothesis to explain such a behavior points to the combined effect on the DOAS retrieval of an increase in shot noise and of a comparably small DOD in the monitored atmosphere. That is, even when the noise is large, if relative absorptions are also large, the DOAS fitting is still able to separate both contributions in the differential spectrum. On the other hand, if the noise is large but the relative absorber amounts are small, the contributions are not easily discernible and the fit might be misled by any additional systematic or near random structure in the spectrum. The fit residual, would exhibit features other that the large shot noise itself, and these would only be eliminated if in the averaging process the noise was reduced enough for the absorption signal to be conveniently larger.

As seen in Figure 9.1(b), for the rightmost LOS the deviation for decreasing intensities from the ideal line is not so pronounced. The linear fit shows a behavior with a slope of 0.58 and a R^2 of 0.97. This might be explained by an enhanced smoothing of all spectral features by the wider slit function of the outer LOS. This would reduce the residuals and minimize the effect of additional structures.

Considering now the RMS behavior for the situation of 9 viewing directions, Figure 9.1(c), the phenomenon at low intensities appears accentuated with respect to the 35 viewing directions case. This might be associated to the introduction of slight additional errors by the averaging, e.g. when the calibration or the slit functions associated to the optical fibres averaged are different (Heue et al, 2008). In addition, in this third case, a deviation for high intensity measurements from the statistical RMS behavior is visible. It points to the existence of a rather small systematic effect that gains importance for increasing intensities as for example non constant stray light which might enter the spectrometer. In any case the behavior of the RMS is still very close to the case of pure statistical behavior, with a linear fit of 0.73 slope and a R^2 of 0.95.

As anticipated before, the value of the RMS anti-correlates with the intensity reaching the CCD. Furthermore, it coincides quite well with the inverse of the SNR expected from the shot noise: $1/\sqrt{I_{meas}}$, see Figure 9.2.

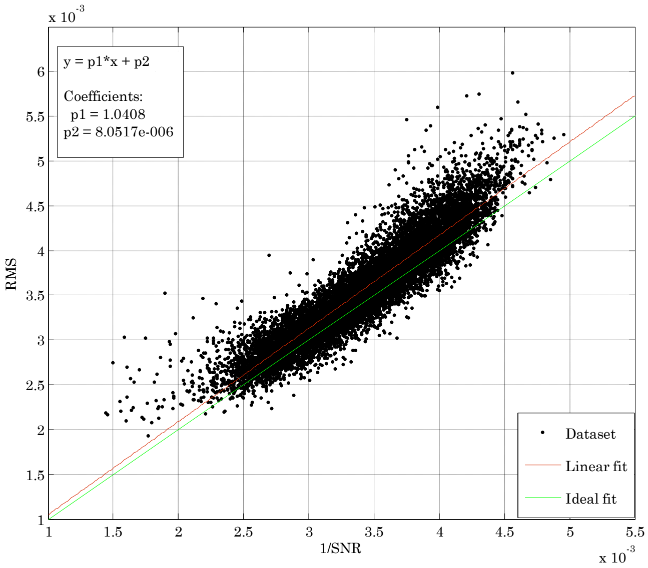

Figure 9.2: Scatter plot of the RMS vs. the inverse of the SNR, if the latter is calculated from the intensity of the collected radiation, assuming that the only contribution to the SNR comes from shot noise.

Consequently, it can be concluded that the measurements are mainly noise limited and the systematic structures have only minor impact.

9.2 Instrument performance assessment

Since the intensity of the radiation collected in the detector is the main factor affecting the RMS of the residuals in the NO_2 retrievals, an assessment of the intensity throughput of the instrument gains relevance (refer to Section 4.3).

The spectral nominal radiance reaching the entrance of the instrument is a critical input variable for the calculation of the number of counts per measurement and per binned pixel of the CCD that are theoretically expected, C_{BU} (Equation 4.8). Therefore, SCIATRAN radiative transfer model runs were performed again, under the same assumptions listed in Section 8.2, to estimate the spectral radiance for several albedo conditions, see Figure 9.3.

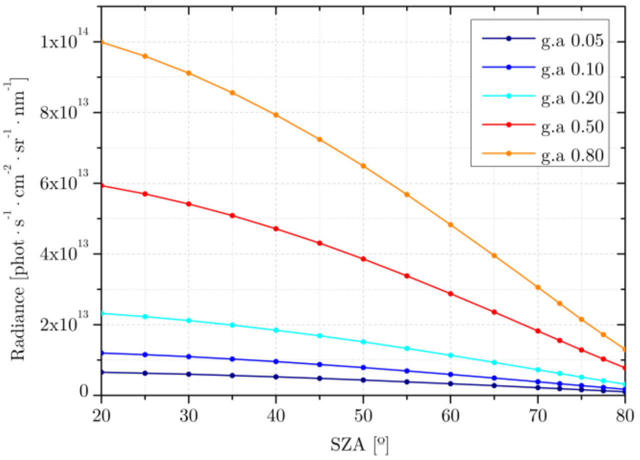

Figure 9.3: Spectral nominal radiance reaching the entrance of a nadir viewing airborne instrument at 1Km altitude, for different ground albedo scenarios. (provided by SCIATRAN RTM)

In order to compare the intensity of backscattered radiation collected in actual measurements with the expected one as estimated from instrumental characteristics, a ground scene of reasonably known reflectance has been selected among the measurements from the flight under consideration. The scene corresponds to the Aasee lake (Ibbenbüren), whose intensity plot is displayed in Figure 9.4. Over Aasee the intensity ranges from 5 to 6x10^5 counts/sec, and it is shown surrounded by fields with intensity recordings of 7 to 10x10^{15} counts/sec. A diffuse reflectance close to 0.05 is expected for water surfaces at 440nm, and overpass of the aircraft above Aasee took place at 41.3° SZA.

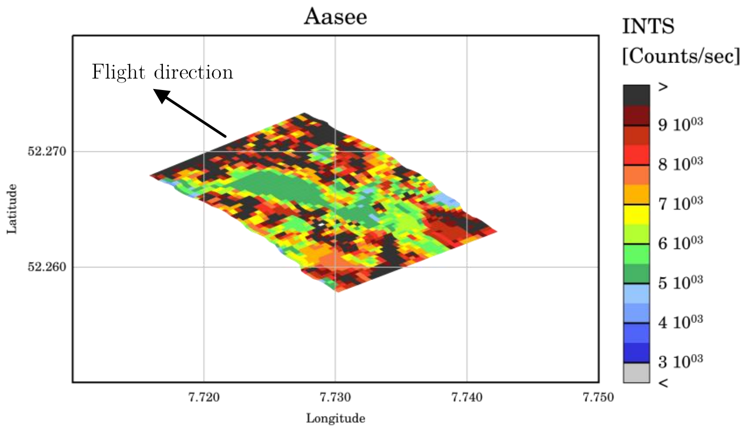

Figure 9.4: Intensity of backscattered radiation for iDOAS measurements over Aasee lake (Ibbenbüren); the aircraft is flying in north-west direction and the across track FOV is divided in a total of 35 pixels.

The intensity of backscattered radiation collected for measurements over Aasee and the intensity expected from theoretical calculations (using the nominal spectral radiance given by SCIATRAN for 0.05 ground albedo and 40° SZA) are compared in Table 9.1. The theoretical values have been computed using the instrumental parameters given in Table 4.1 and by means of Equation 4.8 and Equation 4.3. The theoretical RMS is the inverse of the modeled SNR. The observations given for the Aasee lake are averages over the measured quantities using the pixels that image the lake area (dark green area in Figure 9.4). The measured SNR is the inverse of the mean RMS of residuals resulting from the data fittings.

Case	**LOS num.**	**L_λ Spec. radiance**	**C_{BU}^{bin} [BU/meas/binPix]**	**C_{BU} [BU/sec]**	**RMS**	**SNR**
Theoretical	35	5.242x10^{12}	52491	6999	0.00343	292
	9		199467		0.00174	574
Aasee (measured)	35	--	39461	5261	0.00404	248
	9		157760	5440	0,00203	494

Table 9.1: Comparison of the intensity of radiation reaching the detector (in counts per binned pixel and per measurement, as well as in counts per pixel and per second), RMS and SNR at 40º SZA and for 0.05 ground albedo: from a theoretical model of the instrument characteristics and from actual iDOAS measurements over Aasee lake.

Although the light loss for the studied case is close to 25%, it might be considered that several parameters indicated in Table 4.1 are estimations. The main uncertainty is given by the value for the transmissivity of the optical fibres, which has not been explicitly measured and which depends on factors such as fabrication material, length and wavelength of the transmitted radiation. For typical optical fibres the transmission loss is often relatively larger for wavelengths in the visible range and might go beyond the 50% considered. In addition, the reflectivity value assumed for the Aasee surface might as well have been overestimated, since values around 0.02 for lake surface albedo in the visible region of the spectrum are also reported in the literature, especially when large concentrations of Coloured Dissolved Organic Matter (CDOM) are present in the water (Ficek et al, 2011; Menken et al, 2006).

Therefore, it might be concluded that the 25% loss in radiation intensity points towards an upper limit. Anyhow, a more detailed study on light losses in the instrument might be of great help to reduce the mentioned uncertainties; a measurement of optical fibre transmissivity, a selection of ground surfaces of more precisely know reflectance characteristics and the comparison of different spectral radiance situations, since the intensity loss might depend on the intensity itself.

The comparison given in Table 9.1 reveals rather promising results. Calculated and measured RMS values only deviate by 17%, which means that the theoretical detection limit is only ~17% better than the achieved one.

Indeed, taking the average RMS value given in Table 8.2 for the 425-450nm fitting window, (19.0x10^{-4}) scaled by the maximum absorbed cross section within the fitting window (7.00x10^{-19} cm^2) and by the AMF computed at 40º SZA and 0.05 ground spectral reflectance (2.813) an approximate detection limit for NO_2 vertical columns of 1.24x10^{15} molec/cm^2 is estimated. Moreover, this limit can be reduced by averaging or even by changes in the optical setup.

10. Estimation of emission rates

As a final part of the data analysis, the NO_2 vertical column amounts computed from iDOAS measurements over the Ibbenbüren power plant (Section 8.2) were applied in the estimation of NO_2 emission rates from the stack. The method used for this estimation is the integral of a divergence field, described in Section 6.2.

The most appropriate flight transects over the exhaustion plume were selected for the purpose. Since the wind speed and direction are decisive input values for the successful application of the method, two complementary wind data sources were applied.

The emission estimation presented in the following is a preliminary analysis oriented more to demonstrate the suitability of the data retrieved from measurements with the new iDOAS instrument to quantify source strengths than to report very accurate emission rates. Indeed, such a precise estimation would require a more dedicated flight pattern and, if NO_x instead of NO_2 emission rates are to be reported, additional measurements would be needed.

10.1 Transects over the exhaust plume

As seen in Figure 8.2, the aircraft with the iDOAS instrument on board flew a total of 7 times over the NO_2 exhaustion plume of Ibbenbüren power plant. Since the flight track had not been specifically designed for the iDOAS measurements, some of these tracks are not suitable for the computation of the emission strength.

The choice of a segment (i.e. line of measurements of one constant LOS crossing the NO_2 plume, in this case) perpendicular to the wind direction is particularly desirable because it defines the surface across which the integral NO_2 flux is to be calculated. Those overpasses lying on a curve in the trajectory of the airplane may not be as appropriate as straight paths because the definition of a segment approximately perpendicular to the wind direction might be impossible due to the lack of spatial coverage with NO_2 measurements. If the segment is chosen so that it follows the trajectory of the turn, which is in principle also possible, care has to be taken in choosing the length of the segment, particularly if the curve is sharp.

Because most of the NO_x emissions take place in the form of NO (see Section 1.2), overpasses too close to the stack do not give much information on the emission rates. Furthermore the Gaussian plume model (Section 6.1), which is to be applied for the calculation of an effective wind speed, is not valid for the first few hundred meters from the source.

Additionally, the flight transect at especially low altitude (crossing in north-west direction and observed on top of all other transects in Figure 8.2) was also excluded, since under such circumstances part of the plume is expected to remain above the aircraft.

The application of these criteria led to the selection of a total of 4 transects over the NO_2 column, which are sequentially displayed in Figure 10.1.

Despite the previous reasoning, the last panel in Figure 10.1 shows a transect corresponding to a curve in the trajectory. This transect is still investigated due to the fact that it is the best overpass at large enough distance from the source for which steady state in the NO-NO_2 interconversion can be assumed.

The shape of the plume at distances closer to the source appears irregular and patchy. There might be several reasons for such behaviour in the mapped NO_2 column amounts: variations in the NO-NO_2 conversion rate due to inhomogeneous mixing of the plume with the surrounding air, variable wind and even topographic effects whose influence is enlarged in the first stages of the plume development when its bulk is located closer to the ground. Moreover, if these topographic features induce wavelike structures in the plume (rough terrain or strong winds), the patchy appearance might partly be associated with the change in sensitivity of the iDOAS measurements at different heights.

The apparent rotation of the plume transect imaged in the far overpass at 6km downwind might be attributed to topographic effects (the existence of a close and sharp hill that deviates the column) or to wind variations.

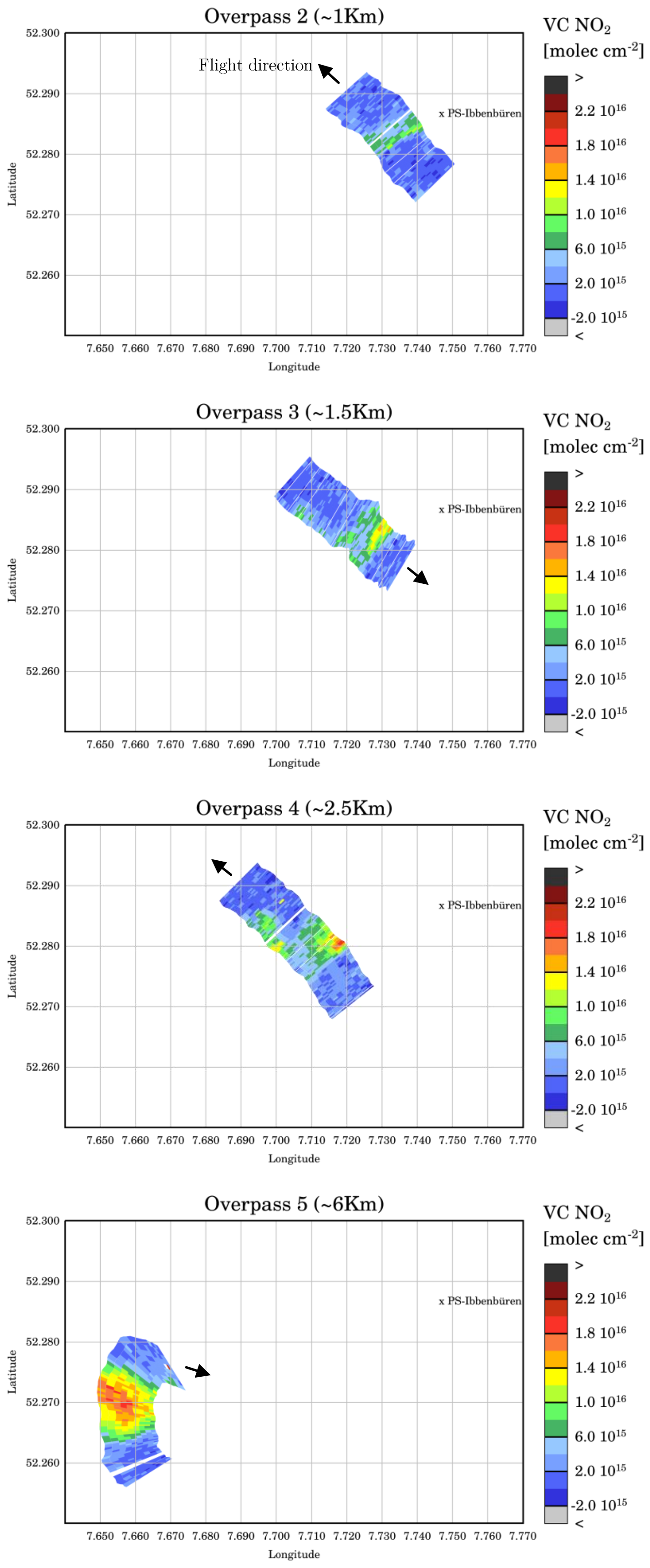

(a) 9.8 UT

(b) 9.9 UT

(c) 10.0 UT

(d) 10.2 UT

Figure 10.1: Selected overpasses over the NO$_2$ exhaust plume, labeled as a function of the approximate distance to the source: (a) c.a. 1km, (b) c.a. 1.5km, (c) c.a. 2.5km and (d) c.a. 6km.

10.2 Wind data

The field whose divergence integral yields an estimate of the source emission rates is the wind field scaled by the corresponding NO_2 concentration at each point. Wind field data from two different sources has been used: in situ data from the AIMMS-20 inertial measurement system mounted on board the aircraft and model data from the COSMO-DE from the German Weather Service (Deutscher Wetter Dienst, DWD). Since vertical column amounts rather than concentrations are available, effective wind speed and direction along the vertical plume extent have to be computed. This is performed for the model wind data field, which gives information on the vertical wind profile. The AIMMS-20 system, on the other hand, only provides wind data at flight altitude.

AIMMS-20 system data

As pointed out above, wind data only at flight altitude is available from the AIMMS-20 measurement system. Although as a general rule the wind changes in direction and speed throughout the atmospheric boundary layer (Ekman spiral), the assumption of a constant speed from the plume to the flight altitude (~1100 m.a.s.l) is reasonable during summer daylight if the mixed layer is well developed (as will be seen later in Figure 10.3 and after).

Wind data from AIMMS-20 is represented as a time series in Figure 10.2. Corresponding values of yaw angle (heading of the aircraft) have been plotted simultaneously to point out an issue in the processing module of the measurement system, which seems to experience problems to subtract the contribution of the movement of the aircraft relative to wind direction.

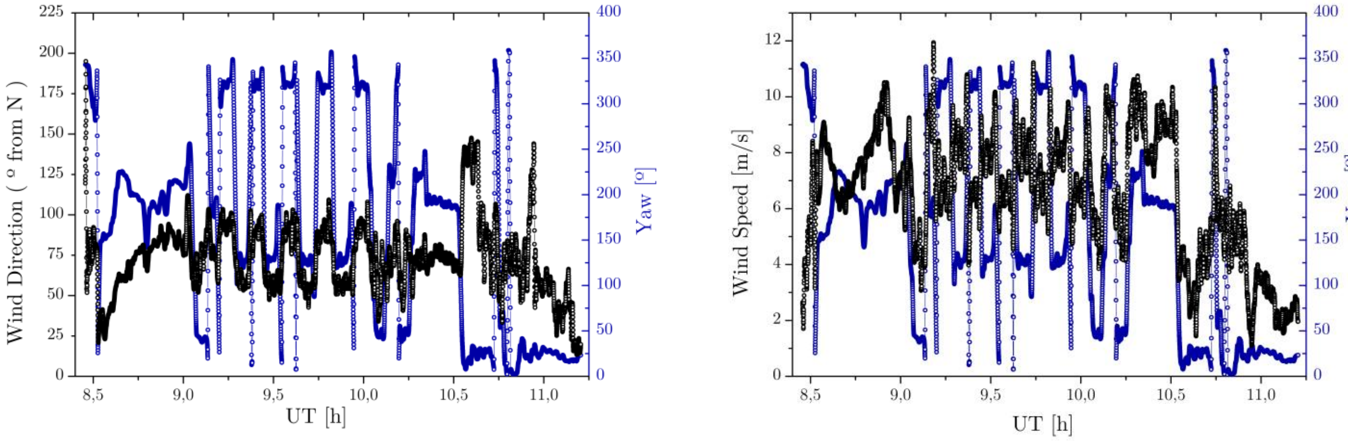

Figure 10.2: Wind direction (left) and speed (right) data time series from AIMMS-20 inertial measurement system on board of the Polar-5 aircraft. Shown are also yaw angle values of the aircraft in each case (in blue), indicating a systematic error in the measured wind data.

The error introduced by the heading of the aircraft for the time interval corresponding to the overpasses above the plume shows a quasi periodic structure but it is too large to be smoothed by a running mean that would reveal the underlying trends. Instead, regular averages over appropriate periods (around ~12 minutes) were applied only to the time interval between 9 and 10.25 UT, when the flight altitude was approximately constant. The resulting wind data is summarized in Table 10.1, and although the uncertainties are large, the average values appear reasonable.

UT interval [h]	**Avg. Height** [m]	**Wind Speed** [m/s]	**Std. Wind Speed** [m/s]	**Wind direction** [º from N]	**Std. Wind direction** [º from N]
9.08-9.23	1138	6.7	2.4	80.8	13.9
9.23-9.42	1142	7.4	1.4	77.8	16.6
9.42-9.61	1148	7.3	1.1	73.1	17.5
9.61-9.80	1136	7.5	1.4	72.7	17.7
9.80-10.00	1131	7.5	1.4	71.8	17.3
10.00-10.25	1132	6.8	1.9	70.0	17.5

Table 10.1: Wind field values and their uncertainties (standard deviations) for the overpasses above Ibbenbüren power station, after processing AIMMS-20 wind data by averaging over consecutive intervals.

In view of the uncertainty in the estimated wind data from the AIMMS-20 system, a complementary data source has been considered in addition.

COSMO-DE model data

The COSMO-DE model[*] is a high resolution numerical weather prediction model run by the DWD. The horizontal grid point size is 2.8km x 2.8km and the vertical resolution ranges from 20 to 200m, improving for low altitudes in the atmosphere. The COSMO-DE wind and temperature data for the particular measurement site and time interval was processed and provided by Thomas Krings, at the IUP Bremen, and was previously received from the DWD.

The processed data grid spans the latitudes from 52.41ºN to 56.15ºN and the longitudes from 7.48ºE to 7.87ºE. It includes 50 vertical layers of which only the lowermost (corresponding to heights from 10m to 2014.3m, see Table 10.3) were used for the effective wind calculation. The vertical coordinate is terrain following.

---

[*] http://www.cosmo-model.org/

Each model grid point provides a vertical wind profile. Therefore, for each of the overpasses, the data from the 4 nearest neighbors of the grid was selected and averaged. For the first three selected overpasses in close vicinity to the source, at 1km 1.5km and 2.5 km respectively (Figure 10.1) these 4 points are the same. The time evolution of the averaged vertical profiles for these cases is shown in Figure 10.1. For the last overpass the nearest grid points are different, but the resulting average profiles are rather similar.

Going back to the wind values from the AIMMS-20 system, in Table 10.1, they can be compared now with the values given by the model for the times 9UT and 10UT. The AIMMS-20 wind data is in accordance with the model outcome at an altitude of 1000m (approx. flight altitude assuming a constant terrain height of 100m).

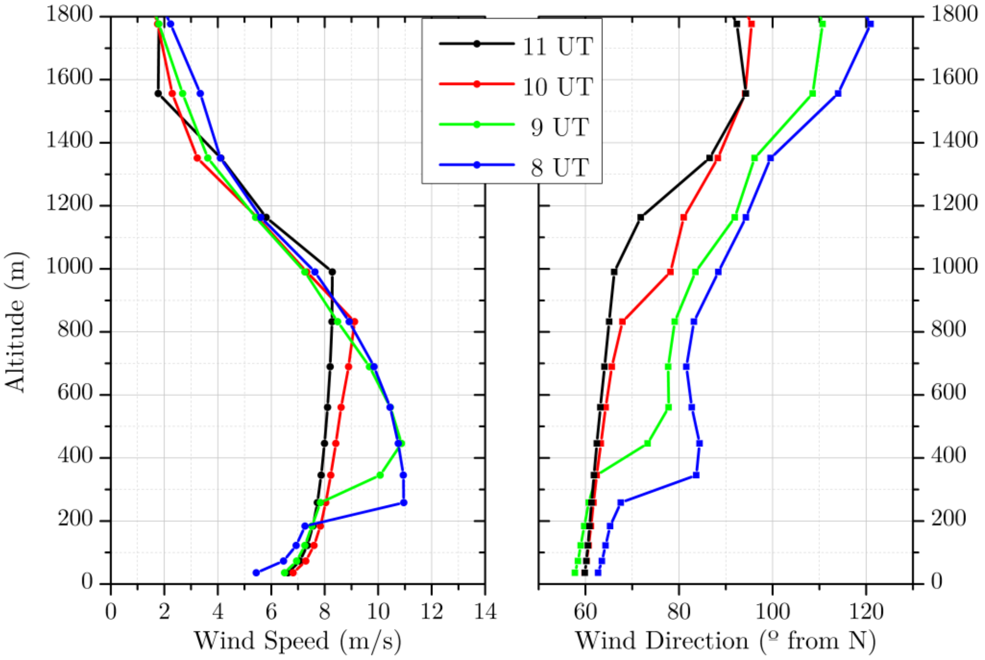

Figure 10.3: Time evolution (at COSMO-DE model temporal resolution) of wind speed (left) and direction (right) profiles, averaged from model data at the 4 nearest grid points from the three selected overpasses above the plume that are closets to the source.

Since the time resolution of the model is 1h and the selected plume overpasses (Section 10.1) are comprised between 9.7 and 10.2 UT, only the model data at 10UT were considered for the calculation of the effective wind speed.

This effective wind speed is calculated from a weighted average of the wind profiles. As explained in Section 6.2, the weighting factors may be calculated from the relative fractions of NO_2 present at each vertical layer of the model.

To estimate these relative fractions the Gaussian plume model was applied, Equation 6.11. The wind speed values derived are large enough for the application of such model. The use of the Gaussian model requires the specification of the average vertical plume dispersion ($\sigma_z(x)$) and of the effective plume height (h), sum of the stack height and plume rise.

The average dispersion depends on the distance to the source and was calculated from the Briggs formulas in Table 6.1, assuming an atmospheric stability class C. The determination of the stability class is not trivial and has been derived through independent methods by Thomas Krings in a not yet published work on MAMAP measurements during the same flight (Krings et al, 2011; for information on MAMAP measurements).

The plume rise was computed using Briggs equations (Equations 6.5, 6.6 and 6.7) assuming typical values of the exit temperature (T_{p0}) and speed (w_0) of the gases from the stack and a characteristic tower radius (R_0) for power stations with features similar to Ibbenbüren. The ambient temperature at stack height (T_{e0}), the ambient temperature gradient (Γ_a) and the wind speed (u) were calculated from COSMO-DE model data, again using a nearest neighbor average. The values used for the calculation are listed in Table 10.2. The plume rise estimated this way is 422m, which added to a stack height of 275m results in an effective plume height of 697m.

Param.	**Description**	**Estimated value**
w_0	Exit velocity of flue gases	30 m/s
T_{p0}	Exit temperature of flue gases	413 K
R_0	Inside stack radius	6 m
T_{e0}	Ambient temperature at stack height (COSMO-DE; z=275m and UT=10h)	293 K
Γ_a	Ambient temperature gradient (COSMO-DE; z=275-2000m and UT=10h)	-0.0072 K/m
u	Mean wind speed at stack height (COSMO-DE; z=275m and UT=10h)	8.3 m/s

Table 10.2: List of the parameters and their estimated values used for the calculation of the plume rise.

The weighting factors for each vertical layer in the model at the different distances from the source, which were used for the calculation of the effective wind speeds and directions, are displayed in Table 10.3. The estimated average dispersion values in each case can also be found in Table 10.3.

Layers COSMO-DE		**Percentage of pollutant per layer (%)**			
Number	**Height [m]**	**x = 1000m** $\sigma_z = 73$**m**	**x = 1500m** $\sigma_z = 105$**m**	**x = 2500m** $\sigma_z = 163$**m**	**x = 6000m** $\sigma_z = 324$**m**
34	2014.3	0	0.	0	0
35	1777	0	0	0	0
36	1556.2	0	0	0	0.4
37	1351.8	0	0	0	1.9
38	1163.2	0	0	0.55	5.1
39	990.2	0	1.04	6.46	9.6
40	832.3	13.3	22.41	23.09	13.3
41	689.3	73.6	51.26	32.55	14.5
42	560.7	12.9	22.13	22.97	13.3
43	446.2	0.2	2.97	9.98	10.8
44	345.5	0	0.19	3.19	8.1
45	258.2	0	0.01	0.87	6.0
46	183.9	0	0	0.23	4.5
47	122.3	0	0	0.07	3.6
48	73	0	0	0.02	3.1
49	35.7	0	0	0.01	2.9
50	10	0	0	0.01	2.9

Table 10.3: Weighting factors for each vertical layer in COSMO-DE at distances corresponding to the selected overpasses. These factors were calculated from the relative NO_2 amounts at each layer, as derived from the Gaussian plume model.

Table 10.4 compares the resulting effective wind speeds and directions, as calculated from the COSMO-DE model, with the wind speed and direction estimated from AIMMS-20 system data, for each considered overpass above the plume. Recalling that AIMMS-20 wind data was measured at flight altitude (~1100m) and assuming that the terrain height is round to 100m in average for the area, these data appear realistic by comparison with COSMO-DE model profiles at 1000m altitude (Figure 10.3). Indeed, wind values from AIMMS-20 at the further part of the plume (6km downwind) seem to fit better the effective wind results from the model at the same distance from the source. This seems reasonable because this overpass takes place later in the morning, when the mixed layer is more developed and spans a larger height range, and further from the source, when the bulk of the plume is expected to be located at higher altitudes.

Data source and distance from stack	**AIMMS-20**				**COSMO model**			
	1000m	**1500m**	**2500m**	**6000m**	**1000m**	**1500m**	**2500m**	**6000m**
Wind Speed [m/s]	7.5	7.5	7.5	7.5	8.9	8.8	8.7	8.1
Wind Direction [º from N]	72.7	71.8	71.8	71.8	69.0	69.7	70.1	71.2

Table 10.4: Compilation of AIMMS-20 wind measurements as well as effective wind speeds and directions estimated from COSMO-DE model data for each of the considered overpasses above the NO_2 exhaust plume.

10.3 Emission rate estimates

The wind speeds and directions derived from in-situ and model data were used in the estimation of NO_2 emission rates for the selected overpasses above the exhaust plume at different distances from the source. These emission rates were calculated by sequential application of the integral of a divergence field method (Section 6.2; Equation 6.10). The integral method requires the selection of an appropriate surface, or in this case a perimeter, enclosing the source for which emissions are to be computed.

The shape of the perimeter can, in principle, be chosen arbitrarily, and those sides of the perimeter parallel to the wind direction will not contribute to the emission calculation. Assuming a constant NO_2 background vertical column of $1x10^{15}$ molec/cm^2 and that no other sources than the power plant stack are enclosed by the perimeter, the integration was applied only to an appropriate downwind segment of the perimeter.

To select the integration segment, the trajectory of the aircraft in each overpass, approximately perpendicular to the wind direction, was used (Figure 10.1). The ground swath of the instrument consists of a sequence of iDOAS measurements, each divided into the corresponding 9 total pixels (LOS). Each of these LOS is associated with a section of the plume situated at slightly different distances downwind.

Hence, the segment determining the surface through which the flux was to be integrated was chosen to follow the ground path of a single LOS. This means that each LOS trajectory within an overpass provided an emission estimate. For a particular LOS, the individual segments, constituent of the overall integration segment, corresponded to a straight line through the centre of the pixel in each measurement. The wind field projected on the normal vector of the segment and scaled with the corresponding NO_2 vertical column (background subtracted) was summed for all the individual segments to yield an emission estimate (as described by Equation 6.10). This was applied for each LOS in each selected overpass and using both in-situ and modeled wind data (Table 10.4).

For each overpass, the number of pixels or individual segments along the perimeter is different, due to the varying plume width. These lengths are not adapted in order to minimize the contribution of the background which is not completely removed. Within a single overpass, the number of pixels in the overall segment was chosen to be the same for all LOS. However, its length varies slightly due to the changing pixel sizes. This is especially relevant in the curved transect at 6km downwind and may lead to inaccuracies if the background is not appropriately corrected. Figure 10.4 displays selected cross sections of the plume at the different distances downwind of the source. The cross sections are drawn as a function of along track pixel number and, therefore, the curve widths do not represent the actual plume width. Still, the plume shape can be appreciated.

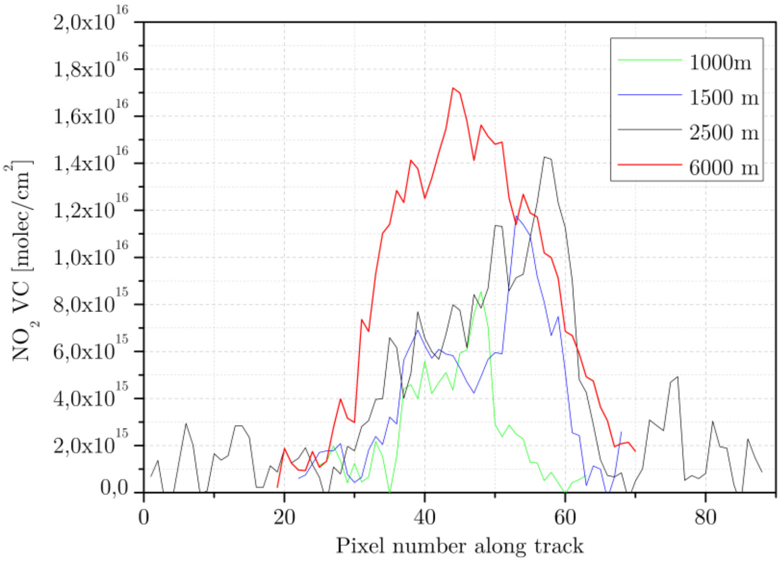

Figure 10.4: Plume cross sections as a function of the pixel position along track and for the selected overpasses at different distances from the source, each for one individual LOS.

The results for the estimated NO_2 emissions are plotted in Figure 10.5, as a function of the approximate distance downwind of the power plant stack. Table 10.5, at the end of the chapter, lists the quantitative results. Emission estimates for the furthest overpass range from 4 to c.a. $9x10^{23}$ molec/sec. These are converted to g/s and Tg/y in order to compare to emission data bases (assuming constant emission rates).

Emissions take place mainly in the form of NO, which is oxidized to NO_2 in the atmosphere and transitory stages are expected until a stationary state in the NO/NO_2 ratio is achieved. Therefore an overall trend is observed in the emission estimates, increasing with distance from the stack. Indeed the trend in Figure 10.5 decreases in strength with increasing distance to the source, pointing to the achievement of such a steady situation. The duration of the transitory state will depend on the particular environmental conditions determined by the ambient availability of O_3, solar UV flux, wind speeds and atmospheric stability (Devis et al, 1972). However, the distance from the source at which stationary state is achieved is expected to be within the first tens of kilometers.

For the three closest overpasses irregular values of emission rates are observed (smaller values for mid-way segments in comparison to segments slightly closer), most likely due to the aforementioned inhomogeneous and patchy structure of the plume in its first stages. The large increasing trend in emission rates appreciated for the furthest plume transect reflect the trend that is also observed in the NO_2 vertical column mapping (see Figure 10.1 (d)), but seems to have been accentuated by the different curvature of the segments considered.

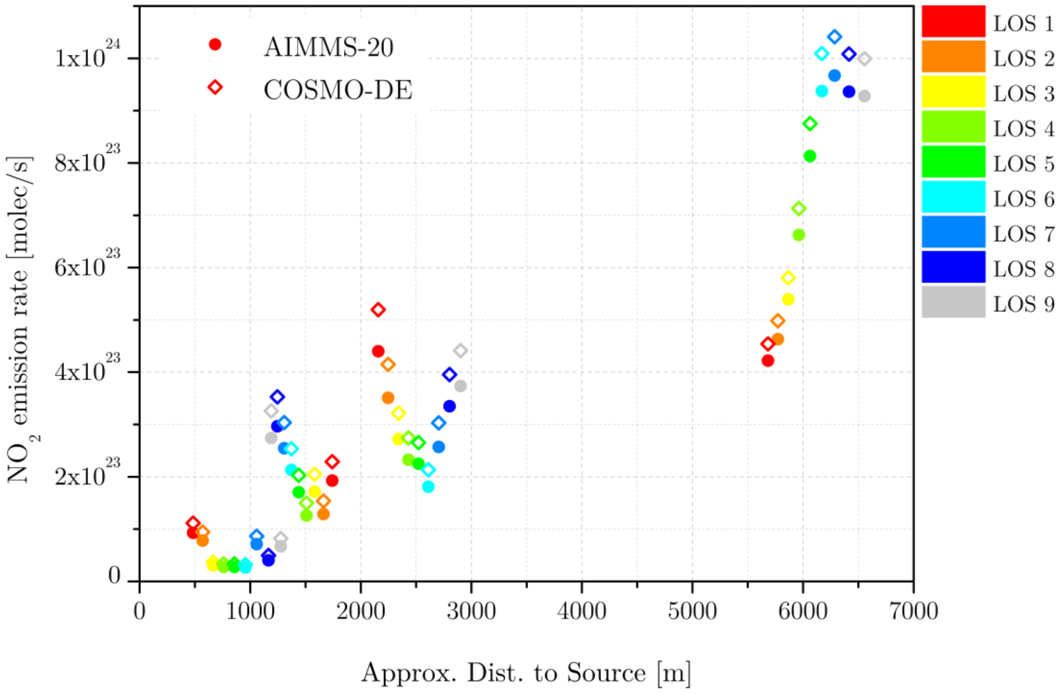

Figure 10.5: Resulting estimates of NO_2 emission rates as a function of the approximate downwind distance from Ibbenbüren power plant. The emissions have been estimated using two complementary wind data sources: AIMMS-20 inertial measurement system on board of the aircraft and COSMO-DE numerical weather prediction model.

According to the wind data time series given by COSMO-DE, the assumption of steady state advection conditions within 1h monitoring of the plume may be quite reasonable, especially for the far transects of the plume, since its average altitude increases with distance to the source (see Figure 10.3). The dispersion conditions, however, depend on the variability of atmospheric conditions and cannot be appropriately assessed. This can introduce a considerable uncertainty, through the estimated value of the average dispersion factor $\sigma_z(x)$, in the application of the effective speed derived from COSMO-DE. A maybe more critical point implicit in the application of the Gaussian model is the assumption of a chemically inert gas. This does not hold for NO_2. However, it is applicable to NO_x compounds as a whole, since their dry deposition may be considered negligible (Ryerson T.B. et al, 1998, and references therein) and their loss through reaction with ambient OH is not expected to be significant for such short distances from the source (Davis D.D. et al, 1972). Therefore, if the NO/NO_2 ratio is assumed to be locally constant along the plume cross section (where the integral method is applied), the Gaussian model still holds. If the assumptions addressed here apply and the NO/NO_2 ratios were known in each case, the NO_x emissions could be calculated from the NO_2 calculations.

As a final consideration, it is interesting to compare the estimated emission values with those emission rates officially reported for Ibbenbüren power station (see Figure 7.2). To do so, the estimated rates in molecules per second were converted to emissions in tons of NO_2 per year (Table 10.5). This conversion introduces some uncertainties in the comparison, because the reported emissions are given in annual tons of NO_x. First, emissions would be underestimated, since the NO amounts were not detected and the ratio NO/NO_2 in equilibrium conditions is, in principle, uncertain (for the same reasons that apply to the uncertainty in the determination of a characteristic transition time). Additionally, the conversion assumes that the power plant operates continuously with the same power throughout the year. It can be argued that the power plant operates mostly continuously; coal fired stations do usually never completely stop the energy supply due to the cost implications of initiating the production again afterwards. However, the production can be adapted according to the variable energetic demands throughout the year. Therefore, the present emission estimates, being derived from measurements in the summer time when the energy production is expected to be decreased, are likely to be lower than the annual mean.

From the reports from Ibbenbüren station in the period spanning from 2007 to 2010 (Figure 7.2), an average emission of 2775 tons of NO_x per year is derived. This value is to be compared with the mean value of the estimated NO_2 emissions for the far transect of the Ibbenbüren exhaust plume, monitored by the airborne iDOAS instrument on the 4th of June 2011. This mean value was computed only taking into account the 4 farthest segments in the most distant overpass, which show approximately constant values and are likely to be closest to the steady state in NO to NO_2 conversion. Hence, the annual average emission estimate is around 2400 tons of NO_2

Despite the approximations undertaken in the emission calculation and the many sources of uncertainty involved (wind data, derived plume rise and average dispersion from atmospheric conditions, as well as uncertainties in the NO_2 SC and AMF), the emission rate estimates yield very promising results. They stay below the reported emission values, in accordance with the above discussion, but they are within the correct order of magnitude.

In addition, it is also possible to do a direct comparison with the reported emission values if a reasonable NO/NO_2 ratio is assumed. From data in June at 45ºN (Ehhalt et al, 1992), a realistic value for this ratio may be 1/4. Since the reported annual emissions in tons are given with respect to the molecular weight of NO_2, the conversion from estimated NO_2 emission rates (E_{est}^{NO2}) to NO_x/NO_2 estimated rates (E_{est}^{NOx}) can be done via the NO/NO_2 ratio (r) as:

$$E_{est}^{NOx} = (1 + r)E_{est}^{NO_2} \tag{10.1}$$

For a ratio (r) of 1/4 and an estimated NO_2 annual emission rate of 2400 tons, the resulting estimated NO_x annual emission rate is of 3000 tons. And this value is very close to that reported for Ibbenbüren power station in 2010 (3080 tons/y, see Figure 7.2).

Despite the lack of detailed error estimation for the calculations, it can be concluded that iDOAS measurements constitute a very powerful tool for the quantification of source strengths and the present results point to the possibility of reasonable estimation of these emission rates. The performance of the derivation can be further improved if more specifically addressed flight patterns and measurement campaigns are performed.

LOS num	Meas. time interval [UT]	Approx. dist. to source [m]	Approx. Travel time [min]	Emission AIMMS-20			Emission COSMO		
				[molec/s]	[g/s]	[T/y]	[molec/s]	[g/s]	[T/Y]
LOS 1	9.7833-9.7889	484	1.13	9.29E+22	7.1	224	1.11E+23	8.5	268
LOS 2		570	1.33	7.82E+22	6.0	188	9.45E+22	7.2	228
LOS 3		665	1.56	3.10E+22	2.4	75	3.72E+22	2.8	90
LOS 4		761	1.78	2.78E+22	2.1	67	3.36E+22	2.6	81
LOS 5		857	2.01	2.77E+22	2.1	67	3.37E+22	2.6	81
LOS 6		957	2.24	2.69E+22	2.1	65	3.25E+22	2.5	78
LOS 7		1058	2.48	7.13E+22	5.4	172	8.66E+22	6.6	209
LOS 8		1166	2.73	4.04E+22	3.1	97	4.97E+22	3.8	120
LOS 9		1276	2.99	6.69E+22	5.1	161	8.23E+22	6.3	198
LOS 1	9.8764-9.8840	1741	4.08	1.93E+23	14.7	465	2.29E+23	17.5	551
LOS 2		1662	3.89	1.29E+23	9.8	311	1.54E+23	11.7	370
LOS 3		1582	3.70	1.72E+23	13.1	414	2.05E+23	15.7	494
LOS 4		1509	3.53	1.26E+23	9.6	303	1.50E+23	11.5	361
LOS 5		1439	3.37	1.71E+23	13.0	411	2.03E+23	15.5	489
LOS 6		1371	3.21	2.13E+23	16.3	513	2.54E+23	19.4	611
LOS 7		1308	3.06	2.55E+23	19.4	613	3.04E+23	23.2	731
LOS 8		1246	2.92	2.97E+23	22.7	715	3.53E+23	27.0	850
LOS 9		1191	2.79	2.74E+23	20.9	660	3.26E+23	24.9	785
LOS 1	9.9972-10.0069	2158	5.05	4.40E+23	33.6	1060	5.20E+23	39.7	1252
LOS 2		2248	5.26	3.51E+23	26.8	846	4.15E+23	31.7	999
LOS 3		2342	5.48	2.72E+23	20.8	656	3.22E+23	24.6	775
LOS 4		2432	5.69	2.33E+23	17.8	560	2.75E+23	21.0	661
LOS 5		2522	5.90	2.25E+23	17.2	542	2.65E+23	20.3	639
LOS 6		2612	6.12	1.81E+23	13.8	436	2.14E+23	16.3	514
LOS 7		2705	6.33	2.57E+23	19.6	620	3.03E+23	23.2	731
LOS 8		2803	6.56	3.35E+23	25.6	807	3.96E+23	30.2	953
LOS 9		2903	6.80	3.74E+23	28.5	900	4.41E+23	33.7	1063
LOS 1	10.1916-10.1987	5683	13.30	4.22E+23	32.2	1017	4.54E+23	34.7	1094
LOS 2		5771	13.51	4.63E+23	35.4	1116	4.98E+23	38.1	1201
LOS 3		5866	13.73	5.39E+23	41.2	1300	5.81E+23	44.4	1399
LOS 4		5962	13.96	6.63E+23	50.6	1596	7.13E+23	54.5	1718
LOS 5		6062	14.19	8.13E+23	62.1	1959	8.75E+23	66.9	2109
LOS 6		6169	14.44	9.37E+23	71.6	2258	1.01E+24	77.1	2431
LOS 7		6285	14.71	9.67E+23	73.9	2330	1.04E+24	79.5	2509
LOS 8		6415	15.02	9.36E+23	71.5	2255	1.01E+24	77.0	2429
LOS 9		6555	15.34	9.28E+23	70.9	2235	9.99E+23	76.3	2407

Table 10.5: Compilation of emission rate estimates as a function of approximate distance to the source and corresponding approximate time of travel. Results are given for estimations computed with in-situ wind data from AIMMS-20 system and model wind data from COSMO-DE.

Summary and Conclusions

Throughout the pages of the present document, the fundamentals of the tropospheric chemistry of nitrogen oxides, of the DOAS formulation and method and on the iDOAS technique in particular have been settled.

The new iDOAS instrument developed at the IUP Bremen and implemented for its setting on board of an aircraft has been introduced. In addition, the instrumental characteristics and parameters have been defined and the related throughput of the instrument has been theoretically modeled.

The iDOAS analysis has been explained in detail and, in the final part, applied to the spectral recordings collected with the airborne instrument during a test flight over the exhaust plume of Ibbenbüren power station, with the objective of monitoring the NO_2 emissions.

For the studied flight, the geolocation correction, used for the determination of the ground viewed swath of the instrument on board of the airplane, has proven very accurate. The spatial resolution of the instrument, with square ground pixels of 30m x 30m (or c.a. 100m x 100m if spatial and temporal averaging is applied), is adequate for the good mapping of anthropogenic sources of air pollution.

Sequential DOAS retrievals with variable combinations of fit parameters were performed for the spectroscopic data observed during the test flight and their results were evaluated. These trials have served to find an optimal combination of fit parameters for the retrieval of tropospheric NO_2 slant columns. The optimal retrieval was found for the fitting window ranging from 425 to 450 nm, and included O_3, O_4 and H_2O absorbers in addition to the target NO_2.

The AMFs adjusted to the experimental conditions were computed by means of SCIATRAN RTM and applied to the retrieved slant column to obtain the corresponding NO_2 vertical column. The influence of the assumptions on the atmospheric state (which are needed for the initialization of the RTM) upon the calculation of the AMF were assessed through a basic sensitivity study.

The vertical columns derived, (of the order of $2x10^{16}$ molec/cm^2) are in concordance with the typical values found in the literature. The monitoring of the advection of the NO_2 exhaust plume in the direction of the mean wind as well as its continuous dispersion has been successful.

Studies of the behavior of the RMS of residuals when averaging consecutive spectra have shown very good performance, indicating that systematic effects have very small impact in the measurements and that the quality of the retrieval is mostly noise limited. The obtained RMS of residuals indicated an average sensitivity limit in NO_2 vertical columns of c.a $1.3x10^{15}$ molec/cm^2, which might be further improved if the light input is increased.

Indeed, the comparison of the actual throughput of the instrument with the one expected from the theoretical modeling of the instrumental characteristics has revealed that no large losses of light take place (below 25%) and that the obtained detection limit does not differ in more than 17% from the theoretical one.

As a final task, the NO_2 emission rates from Ibbenbüren power plant have been estimated by means of the divergence field integral method. For the estimation, the measured NO_2 vertical columns and two complementary wind data sources have been used (in situ and model data). Wind data sources both have yielded consistent NO_2 emission rate estimates on the order of $9x10^{23}$ molec/sec (~2400 T/y). A basic comparison of these estimates with the annual emission rates reported for Ibbenbüren power plant (of around 3000T/y of NO_x/NO_2), assuming a typical NO/NO_2 ratio in photostationary conditions, indicates that the estimates are reliable. With this, the adequacy of the method and instrument for the quantification of source strengths has been demonstrated. Furthermore, it is expected that dedicated flight patterns and measurements would greatly decrease the uncertainty for these estimates.

Overall, it can be concluded that the results are very satisfactory, that the instrument is suitable and performs adequately in the characterization of anthropogenic sources of air pollution and that it might be ready for a wide range of applications. Indeed it might be interesting and is considered as a possible activity for the future, to conduct analogous analysis and assessment for the rest of the test flights performed in 2011, since these pose an additional challenge for the instrument, being not so large and strong sources of NO_2.

References

A. Rozanov, V. Rozanov, M. Buchwitz, A. Kokhanovsky, J. P. Burrows: SCIATRAN 2.0 – A new radiative transfer model for geophysical applications in the 175–2400 nm spectral region; *Adv. Space Res., vol. 36*, pp. 1015-1019; 2005

Beilke, S., Markusch, H., Jost, D.: Measurements of NO-oxidation in power plant plumes by correlation spectroscopy; Proceedings of 2nd Europion Symposium on the Physico-Chemical Behavior of Atmospheric Pollutants (1981), D. Reidel Publishing Company, Dordrecht, Holland, pp. 448–459; 1981

Berg N., Mellqvist J., Jalkanen J.-P., Balzani J.: Ship emissions of SO_2 and NO_2: DOAS measurements from airborne platforms; *Atmos. Meas. Tech. Discuss., vol. 4*, pp. 6273-6313; 2011

Bernhardt, F.: Optimierung und Anwendung eines abbildenden Spektrometers zur räumlich aufgelösten Messung atmosphärischer Spurengase vom Flugzeug, Diploma Thesis, IUP, University of Bremen, 2010.

Bluett J., N. Gimson, G. Fisher, C. Heydenrych, T. Freeman, J. Godfrey: Good Practice Guide for Atmospheric Dispersion Modelling; Ministry for the Environment Manatū Mō Te Taiao, Wellington, New Zealand; 2004

Bobrowski N.,Hönninger G., Lohberger F., Platt U.: IDOAS: A new monitoring technique to study the 2D distribution of volcanic gas emissions; *J. Volcanol. Geotherm. Res., vol. 150 (4)*, pp. 329–338; 2006

Bovensmann, H., Burrows J. P., Buchwitz M., Frerick J., Noël S., Rozanov V. V., Chance K. V., Goede A. P. H.: SCIAMACHY: Mission Objectives and Measurement Modes. *J. Atmos. Sci., vol. 56*, pp. 127–150; 1999

Briggs, G.A.: Diffusion estimation for small emissions; Air Resources Atmospheric Turbulence and Diffusion Laboratory, Annual report ATDL-106, pp. 83-145; 1973

Briggs, G.A.: Plume Rise Predictions; Air Resources Atmospheric Turbulence and Diffusion Laboratory, Annual report ATDL-76/14, pp. 425-478; 1975

Bruns M., Buehler S. A., Burrows J. P., Richter A., Rozanov A., Wang P., Heue K. P., Platt U., Pundt I., Wagner T.: NO_2 Profile retrieval using airborne multi axis UV-visible skylight absorption measurements over central Europe; *Atmos. Chem. Phys., vol. 6*, pp. 3049–3058; 2006

Davis D.D., G. Smith, G. Klauber: Trace gas analysis of power plant plumes via aircraft measurement: O_3, NO_x, and SO_2 chemistry; *Science, Vol. 186*, pp. 733-736; 1974

Ehhalt D.H., Rohrer F., Wahner A.: Sources and Distribution of NO_x in the Upper Troposphere at Northern Mid-Latitudes; *J. Geophys. Res., Vol. 97*, pp. 3725-3738; 1992

Ehhalt, D.H.: Gas phase chemistry of the troposphere In: Zellner, R. (ed.) *Global Aspects of Atmospheric Chemistry*; Deutsch Bunsen-Gesellschaft für Physikalische Chemie; Steinkopf, Darmstadt; Springer, New York; 1999

Fehsenfeld F. C., Drummond J. W., Roychowdhury U. K., Galvin P. J., Williams E. J., Buhr M. P., Parrish D. D., Hübler G., Langford A. O., Calvert J. G., Ridley B. A., Grahek F., Heikes B. G., Kok G. L., Shetter J. D., Walega J. G., Elsworth C. M., Norton R. B., Fahey D. W., Murphy P. C., Hovermale C., Mohnen V. A., Demerjian K. L., Mackay G. I., Schiff H. I.: Intercomparison of NO_2 Measurement Techniques; *J. Geophys. Res., vol. 95,* pp. 3579-3597; 1990

Ficek D., Zapadka T., Dera J.: Remote sensing reflectance of Pomeranian lakes and the Baltic; *OCEANOLOGIA, Vol. 53* , pp. 959-970; 2011.

Fix A., Ehret G., Flentje H., Poberaj G., Gottwald M., Finkenzeller H., Bremer H., Bruns M., Burrows J. P., Kleinböhl A., Küllmann H., Kuttippurath J., Richter A., Wang P., Heue K.-P., Platt U., Pundt I., Wagner T.: SCIAMACHY validation by aircraft remote sensing: design, execution, and first measurement results of the SCIA-VALUE mission; *Atmos. Chem. Phys., vol. 5*, pp. 1–18; 2005

Friedeburg C.V., Platt U., Wagner T.: Measurements of trace gas distributions using Long-path DOAS-Tomography during the motorway campaign BAB II: experimental setup and results for NO_2; *Atmospheric Environment, vol. 39*, pp. 967–975; 2005

Galle B., Oppenheimer C., Geyer A., McGonigle A. J. S., Edmonds M., Horrocks L. A.: A miniaturized ultraviolet spectrometer for remote sensing of SO_2 fluxes: a new tool for volcano surveillance; *J. Volcanol. Geotherm. Res., vol. 119*, pp. 241-254; 2003

Gerilowski, K., Tretner, A., Krings, T., Buchwitz, M., Bertagnolio, P. P., Belemezov, F., Erzinger, J., Burrows, J. P., and Bovensmann, H.: MAMAP – a new spectrometer system for column-averaged methane and carbon dioxide observations from aircraft: instrument description and performance assessment*; Atmos. Meas. Tech. Discuss., vol. 3*, pp. 3199-3276; 2010

Grainger, J. F. and Ring J.: Anomalous Fraunhofer line profiles; *Nature, vol. 193*; 1962.

Heckel A., Richter A., Tarsu T., Wittrock F., Hak C., Pundt I., Junkermann W., Burrows J. P.: MAX-DOAS measurements of formaldehyde in the Po-Valley; *Atmos. Chem. Phys., vol. 5*, pp. 909–918; 2005

Heue K.-P., Richter A., Bruns M., Burrows J. P., Friedeburg C. v., Platt U., Pundt I., Wang P., Wagner T.: Validation of SCIAMACHY tropospheric NO2-columns with AMAXDOAS measurements; *Atmos. Chem. Phys., vol. 5*, pp. 1039–1051; 2005

Heue K.-P., Wagner T., Broccardo S. P., Walter D., Piketh S. J., Ross K. E., Beirle S., Platt U.: Direct observation of two dimensional trace gas distributions with an airborne Imaging DOAS instrument; *Atmos. Chem. Phys., vol . 8,* pp.6707-6717; 2008

Holloway A.M. and Wayne R. P.: Atmospheric Chemistry; Royal Society of Chemistry, Cambridge; 2010

Johansson M., Rivera C., de Foy B., Lei W., Song J., Zhang Y., Galle B., Molina L.: Mobile mini-DOAS measurement of the outflow of NO_2 and HCHO from Mexico City; *Atmos. Chem. Phys., vol. 9*, pp. 5647–5653; 2009

Krings, T., Gerilowski, K., Buchwitz, M., Reuter, M., Tretner, A., Erzinger, J., Heinze, D., Burrows, J. P., and Bovensmann, H.: MAMAP – a new spectrometer system for column-averaged methane and carbon dioxide observations from aircraft: retrieval algorithm and first inversions for point source emission rates; *Atmos. Meas. Tech. Discuss., vol. 4*, pp. 2207-2271; 2011

Lee D.S., Köhler I., Grobler E., Rohrer F., Sausen R., Gallardo-Klenner L., Olivier J.G.J., Dentener F.J., Bouwman A.F.: Estimations of global NO_X emissions and their uncertainties; *Atmos. Environ., Vol. 31*, pp. 1735-1749; 1997

Lohberger F., Hönninger G., Platt U.: Ground-Based Imaging Differential Optical Absorption Spectroscopy of Atmospheric Gases; *Applied Optics, vol. 43 (24)*, pp. 4711-4717; 2004

Lyons T.J and Scott W.D.: Principles of Air Pollution Meteorology; Belhaven Press, London; 1990

Melamed M. L., Solomon S., Daniel J. S., Langford A. O., Portmann R. W., Ryerson T. B., Nicks D. K., Jr. and S. A. McKeen: Measuring reactive nitrogen emissions from point sources using visible spectroscopy from aircraft; *J. Environ. Monit., vol. 5*, pp. 29–34; 2003

Menken, K. D. Brezonik, P. L. Bauer, M. E.; Influence of Chlorophyll and Colored Dissolved Organic Matter (CDOM) on Lake Reflectance Spectra: Implications for Measuring Lake Properties by Remote Sensing; *Lake and Reservoir Management; Vol. 22*, pp. 179-190; 2006

Noxon J.F.: Nitrogen dioxide in the stratosphere and troposphere measured by ground-based absorption spectroscopy; *Science, vol. 189*, pp. 547–549; 1975

Platt U. and Perner D.: Direct Measurements of Atmospheric CH_2O, HNO_2, O_3, NO_2, and SO_2 by Differential Optical Absorption in the Near UV; *J. Geophys. Res., vol. 85,* pp. 7453-7458; 1980

Platt U. and Stutz J.: Differential Optical Absorption Spectroscopy: Principles and Applications; Springer Verlag Heidelberg; 2008

Pommereau, J.-P., Piquard, J.: Ozone and nitrogen dioxide vertical distributions by UV–visible solar occultation from balloons; *Geophys. Res. Lett., vol. 21*, pp. 1227–1230; 1994

Richter A. and Burrows J. P.: Tropospheric NO_2 from GOME measurements; *Adv. Space Res., vol. 29 (11)*, pp. 1673-1683; 2002

Richter A., Eisinger M., Ladstätter-Weiβenmayer A., Wittrock F., Burrows J. P.: Ground based UV/Vis measurements of O_3, NO_2, BrO and OClO over Bremen (53°N); *Proc. 3rd Europ. Symp. on Stratospheric Ozone, Schliersee*, pp. 373-378; 1995

Richter A.: Absorptionsspektroskopische Messungen stratosphärischer Spurengase über Bremen, 53°N; PhD thesis, Universität Bremen; 1997.

Rozanov V., M. Buchwitz, K.-U. Eichmann, R. de Beek, J.P. Burrows: Sciatran - a new radiative transfer model for geophysical applications in the 240–2400 nm spectral region: the pseudo-spherical version; *Adv. Space Res., vol. 29*, pp. 1831-1835; 2002

Rozanov V.V. and Rozanov A.V.: Differential optical absorption spectroscopy (DOAS) and air mass factor concept for a multiply scattering vertically inhomogeneous medium: theoretical consideration; *Atmos. Meas. Tech. Discuss., Vol. 3*, pp. 697–784; 2010

Rozanov, V. V., D. Diebel, R. J. D. Spurr, and J. P. Burrows: GOMETRAN: A radiative transfer model for the satellite project GOME, the plane-parallel version; *J. Geophys. Res., vol. 102*, pp. 16683–16695; 1997

Ryerson T. B., M. P. Buhr, G. J. Frost, P. D. Goldan, J. S. Holloway, G. Hübler, B. T. Jobson, W. C. Kuster, S. A. McKeen, D. D. Parrish, J. M. Roberts, D. T. Sueper, M. Trainer, J. Williams, F. C. Fehsenfeld: Emissions lifetimes and ozone formation in power plant plumes; *J. Geophys. Res., Vol. 103*, pp. 22569-22583; 1998

Schiff H. I., Karecki D. R., Harris G. W., Hastie D. R., Mackay G. I.: A Tunable Diode Laser System for Aircraft Measurements of Trace Gases; *J. Geophys. Res., vol. 95,* pp. 10147-10153; 1990

Schönhardt A., Richter A., Krautwurst S., Gerilowski K., Wittrock F., Burrows J. P.: A new airborne imaging DOAS instrument - development and first measurements; 5th International DOAS Workshop, Mainz, Germany; July 2011.

Sillman S., Logan J.A., Wofsy S.C.: The sensitivity of ozone to nitrogen oxides and hydrocarbons in regional ozone episodes; *J. Geophys. Res., Vol. 95*, pp. 1837-1852; 1990

Stutz, J. and Platt, U.: Numerical analysis and error estimation of differential optical absorption spectroscopy measurements with least squares methods. *Appl. Opt., vol. 35*, pp. 6041–6053; 1996

Sussmann R., Stremme W., Burrows J. P., Richter A., Seiler W., Rettinger M.: Stratospheric and tropospheric NO2 variability on the diurnal and annual scale: a combined retrieval from ENVISAT/SCIAMACHY and solar FTIR at the Permanent Ground-Truthing Facility Zugspitze/Garmisch; Atmos. Chem. Phys., Vol. 5, pp. 2657–2677; 2005

Vountas M., Rozanov V. V., Burrows J. P.: Ring Effect: Impact of rotational Raman Scattering on Radiative Transfer in Earth's Atmosphere, *J. Quant. Spec. Rad. Transf., vol. 60 (6)*, pp. 943-961; 1998

Wagner T., Ibrahim O., Shaiganfar R., Platt U.: Mobile MAX-DOAS observations of tropospheric trace gases; *Atmos. Meas. Tech., vol. 3*, pp. 129–140; 2010

Wang P., Richter A., Bruns M., Burrows J. P., Scheele R., Junkermann W., Heue K.-P., Wagner T., Platt U., Pundt I.: Airborne multi-axis DOAS measurements of tropospheric SO_2 plumes in the Po-valley, Italy; *Atmos. Chem. Phys., vol. 6*, pp. 329–338; 2006

Wang P., Richter A., Bruns M., Rozanov V. V., Burrows J. P., Heue K.P., Wagner T., Pundt I., Platt U.: Measurements of tropospheric NO_2 with an airborne multi-axis DOAS instrument; *Atmos. Chem. Phys., vol. 5*, pp. 337–343; 2005

White W.H.: NO_x-O_3 photochemistry in power plant plumes: comparison of theory with observation; *Environmental Science and Technology, Vol. 11*, pp. 995-1000; 1977

Wittrock F., Oetjen H., Richter A., Fietkau S., Medeke T., Rozanov A., Burrows J.P.: MAX-DOAS measurements of atmospheric trace gases in Ny-Alesund - Radiative transfer studies and their application; *Atmos. Chem. Phys., Vol. 4*, pp. 955–966; 2004